Fundamental Study on Spin State Transition of Fe and Co Complexes

李, 国玲

https://doi.org/10.15017/1866328

出版情報：Kyushu University, 2017, 博士（理学）, 課程博士
バージョン：
権利関係：

A Dissertation Submitted to Kyushu University for the Doctorate Degree of Philosophy

Fundamental Study on Spin State Transition of Fe and Co Complexes

Guo-Ling Li

Supervised by

Professor Katsuhiko Tomooka

Professor Osamu Sato

Department of Molecular and Material Sciences, Interdisciplinary Graduate School of Engineering Science, Kyushu University

2017

Contents

Chapter 1. Introduction

1. 1 Magnets Based on Coordination Complexes

Magnetic properties are basic nature for materials. The investigation of magnetic properties on materials can not only shed light on fundamental science but also can provide promising candidates for practicable devices. With the development of theoretical science and experimental technique, the essential nature of magnetic materials has been well understood.[1–6] The basic concepts of paramagnetism (for compound with unpaired electrons) and diamagnetism (for compound without unpaired electrons) were presented by M. Faraday in 1845. The correlations of magnetic susceptibility and temperature for paramagnetic and diamagnetic materials were discovered by P. curie, which were further developed to the significant low of Curie-Weiss by P. Weiss at the ending of 19 century. More in-depth understanding of magnetism profited from the development of quantum mechanics. At the beginning of 20 century, some important experiments gave out the evidence that magnetic moment is intrinsic nature for electron instead of generating by electron motion. In 1928, spin quantum number and gyromagnetic ratio for electron were determined through relativity quantum mechanics by P. Dirac, and Heisenberg magnetic exchange model based on spin-spin interaction was built by W. Heisenberg. These theories are important basis for modern magnetism, which give us insight into the intrinsic nature of magnetism at atomic and molecular lever.

Magnetic properties of materials can be classified to seven types according to the variation tendency of magnetization (M) with temperature (T) under applied magnetic field (H), namely, diamagnetism, paramagnetism, ferromagnetism, antiferromagnetism, ferrimagnetism, canted antiferromagnetism, and metamagnetism. Compounds without unpaired electrons have no net spin, and thus show diamagnetism. As for paramagnetic materials, all individual spins are uncoupled and randomly distribute in lattice (Figure 1.1 a) because of spin coupling energy is lower than coupling-

breaking energy. In the lattice of ferromagnetic materials, all individual spins are coupled and align parallelly to each other (Figure 1.1 b). In contrast, the individual spins are antiparallelly coupled in lattice for antiferromagnetic and ferrimagnetic compounds. If the antiparallelly coupled spins have identical moments, the compounds exhibit antiferromagnetism (Figure 1.1 c). When the moments of the antiparallelly coupled spins are distinct, that is, nonzero moments existing in the lattice, the compounds show ferrimagnetism (Figure 1.1 d). Some antiferromagnetic compounds show weak ferromagnetism at temperature close to absolute zero. This phenomenon is called canted antiferromagnetism, in which spins are not exactly antiparallel to each other (Figure 1.1 e). Some antiferromagnetic compounds with strong magnetic anisotropy may show first-order first order transition to ferromagnetic interaction under applied magnetic field, which is described as metamagnetism. It is worth to note that materials with coupled spins exhibit spontaneous magnetization below a critical temperature.

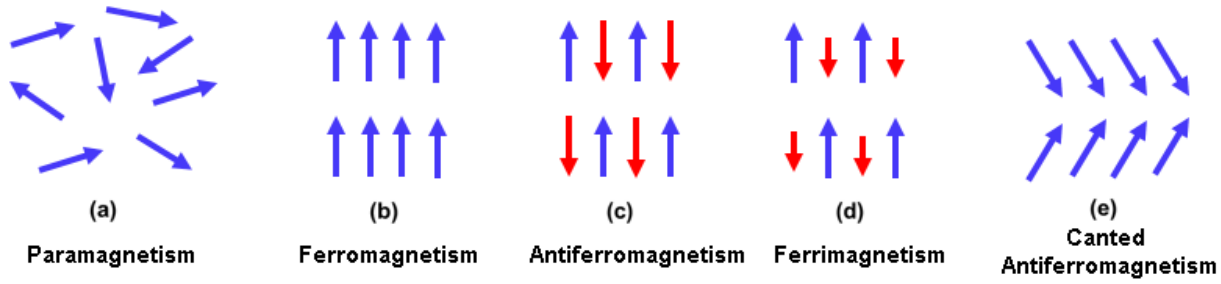

Figure 1.1 Schematic description of spin arrangements for some common magnetic behaviors.

The first discovery of magnetic property was on magnetite that exhibited strong ferromagnetism. The characteristic of magnetite is that they are compose of metallic oxides, and magnetic exchange interactions are through metallic bonds or ionic bonds. Hence, magnetite can be called atomic based magnets. With the development of magnetism and some special functional request for magnetic material, molecular based magnets have become a type of important object in this field.[2–7] Molecular based magnets possess some unique characteristics compared with traditional magnets: a) molecular

based magnets can be synthesized at moderate conditions; b) the structures and properties of molecular based magnets can be turned through chemical modification; c) molecular based magnets are compatible with biological system. Organic radicals and coordination compounds are two kinds of molecular based magnets.

Coordination compounds are composed of metal ions and organic ligands that are linked together through coordination bonds. Coordination magnetic complexes have received considerable research attention due to their adjustable magnetic properties and structures.[8] Generally, magnetic properties of coordination compounds are mainly from the metal ions with higher spin numbers. Variable oxidation states and electronic conformations of metal centers give the possibility of variable magnetic properties to coordination compounds. While the coordination ligands play significant roles to determine magnetic properties and structures for coordination compounds. Since the molecular structures can be relatively easy determined, coordination compounds are good candidates for studying magneto-structural correlations.

The exploitation of practicable magnetic devices, such as high-density memory devices, quantum computation, and molecular spintronics, require the materials to exhibit switchable magnetic states. The spin state of a complex is characterized by total spin direction and total spin number. Therefore, switchable magnetic states can be spin direction transition and spin number transition. Up to now, numerous coordination compounds exhibiting interesting spin state transition behaviors in solid states, including slow magnetic relaxation (spin direction change), spin number transition (spin transition in one metal center or charge transfer-coupled spin transition between two spin carriers), have been well investigated,[4–11] which will be introduced separately in the following sections.

1. 2 Slow Spin Direction transition in Low-Dimensional Complexes

The key point for coordination compounds being used as information memory devices is displaying spin state variable behaviors. Variable directions of magnetization is one of the significant magnetic

property. Slow spin direction transition, generally referred as slow magnetization relaxation, is the main mechanism for traditional magnetic materials being used as memory devices, which requires the materials possessing large magnetic moment with two opposite directions in ground state and a large energy barrier to re-orientate the magnetic moment. The traditional magnetic materials are generally composed of metallic alloys or metallic oxides, which exhibit long-range magnetic ordering below critical temperature and thus have large magnetization. The reversal energy barrier originates from magnetic anisotropy. Generally, molecular structures of traditional magnetic materials are high dimension, which limits them being used as high-density information carriers. Fortunately, the observation of slow magnetization dynamics in low-dimensional molecular based magnets, namely, single-molecule magnet (SMM), single-chain magnets (SCM), single-ion magnet (SIM) and single-atom magnet (SAM) presents a promising avenue for the development of high-density memory devices, as well as quantum computation and molecular spintronics.[12-15] Although the mechanism of magnetic bistability is the same with traditional media, the magnetization dynamics of low-dimensional molecular based magnets do not lie in formation of magnetic ordering.

Single-molecule magnet (SMM) is a kind of superparamagnetic material that displays slow relaxation of magnetization below a certain temperature. The magnetization of SMM is purely molecule derivation and independent of intermolecular interactions. Thus, SMM behavior can be observed regardless of the media where the molecules distribute. For SMMs, the molecules can be magnetized under an applied magnetic field, that is, the magnetic moments exhibit uniform direction with external magnetic field. The magnetized molecules can maintain their oriented magnetic moments at low temperature because of the presence of reversal energy barrier. The re-orientation barrier is related to magnetic anisotropy of the spin ground state. The magnetic anisotropy is produced by zero-field splitting (ZFS). When the spin multiplicities (2S+1) of the ground state are higher than triple-state, ZFS may occur if the molecular symmetry is lower than cubic. In the low symmetric molecule, the separated excited states interact with ground state through spin-orbital coupling, which

leads to further separation of the ground state into sublevels $|M_s>$ and formation of pseudo-degenerated bistable states (Figure 1.2). The Hamiltonian related to ZFS is expressed as following:

$$\hat{\mathrm{H}} = D\left(\hat{\mathrm{S}}_z^2 - S(S+1)/3\right) + E\left(\hat{\mathrm{S}}_x^2 - \hat{\mathrm{S}}_y^2\right) \qquad (1.1)$$

where D and E stands for the axial and rhombic ZFS parameters, and $\hat{S}$ represent the spin projection in a given axis.[16] For compounds with integer spin numbers, the energy barrier (U_{eff}) to relax the magnetization is determined by $U_{eff} = |D| \cdot S^2$. While for complexes with half spin numbers, the energy barrier (U_{eff}) is given by $U_{eff} = |D| \cdot (S^2 - {}^1/_4)$.

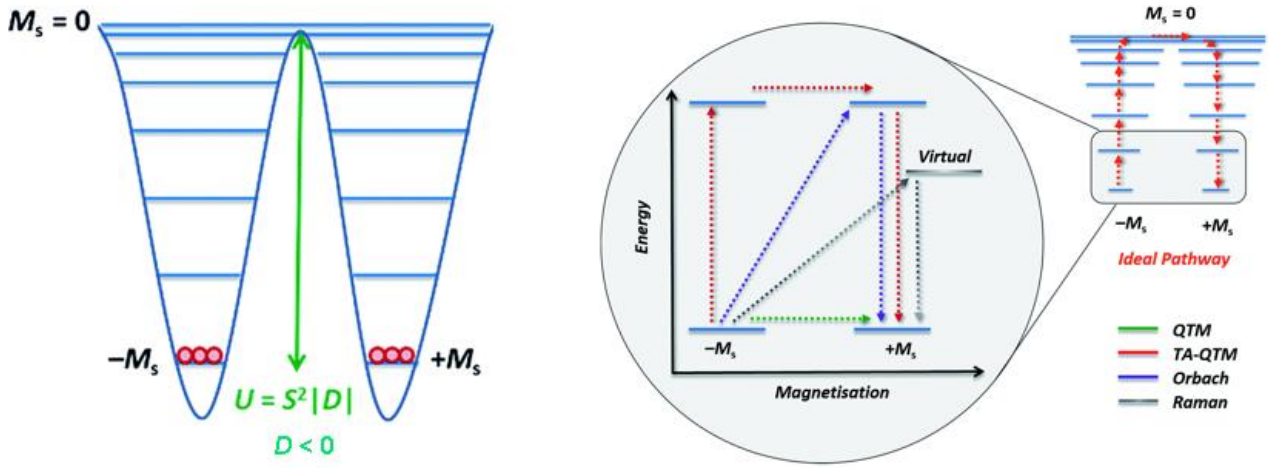

Figure 1.2 Double-well energy diagram produced by negative axial ZFS with red arrow showing ideal relaxation process (left), and schematic illumination of possible relaxation processes for SMMs (right). (Reprinted from ref.17)

The relaxation of magnetization for SMMs may pass through serval different processes, including Orbach, Raman, direct, and quantum tunneling (Figure 1.2).[17] The first three relaxation mechanisms are phonon-assisted processes, in which Orbach, Raman process involves two phonon, and direct process relates to one phonon. In the Orbach process, the ground spin of molecule absorbs a phonon reaching to a real state and then relaxes to the other ground state with emission of one phonon. The Raman process is similar with Orbach process but the phonon-excited state is an imaginary level. The

direct mechanism relates to flip of the molecular spin with one phonon emission. Quantum tunneling of magnetization (QTM) is induced by the perturbation in the system, such as transverse anisotropy and dipolar-dipolar interaction.[13] Herein, transverse anisotropy perturbation induced QTM is discussed. The transverse ZFS parameter E is non-zero when the molecule has no exact symmetric axis, and the rhombic ZFS Hamiltonian $\hat{\mathrm{H}} = E\left(\hat{\mathrm{S}}_x^2 - \hat{\mathrm{S}}_y^2\right)$ and axial ZFS Hamiltonian $\hat{\mathrm{H}} = D\left(\hat{\mathrm{S}}_z^2 - S(S+1)/3\right)$ are not commutable, which leads to no complete set of common eigenstate for the two Hamiltonians. The transverse anisotropy results in the mixture of different $|M_s>$ states, and thus induces QTM. QTM allows the spin to flip between two resonant $|M_s>$ states in two side of energy barrier, including between two ground $|M_s>$ states and two thermally excited $|M_s>$ states. QTM occurring between two ground $|M_s>$ states will cause no detectable slow magnetization relaxation behavior for complexes.

The relaxation barrier, relaxation mechanism and relaxation time of SMMs can be determined via several different techniques, among which alternating current (ac) magnetic susceptibility measurement is generally used. The ac magnetic susceptibility is composed of a real-part (in-phase) susceptibility (χ_m') and an imaginary-part (out-of-phase) susceptibility (χ_m''). Under applied ac field, the lack of ability of the magnetization to follow the progressive filed variation leads to a decrease of χ_m' and an increase of χ_m'', and the χ_m'' will reach to a maximum before declining again. The relationship between the ac magnetic susceptibility and relaxation time (τ) follows a generalized Debye model, which is expressed as below:

$$\chi_m = \chi_m{}' - i\chi_m{}'' \tag{1.2}$$

$$\chi_m = \chi_s + \frac{\chi_t - \chi_s}{1+(i\omega\tau)^{1-\alpha}} \tag{1.3}$$

$$\chi_m{}' = (\chi_t - \chi_s)\frac{((\omega\tau)^{1-\alpha}\cos\left(\frac{\pi\alpha}{2}\right))}{1+2(\omega\tau)^{1-\alpha}\sin\left(\frac{\pi\alpha}{2}\right)+(\omega\tau)^{2-2\alpha}} \tag{1.4}$$

$$\chi_m'' = \chi_s + (\chi_t - \chi_s)\frac{1+(\omega\tau)^{1-\alpha}\sin(\frac{\pi\alpha}{2})}{1+2(\omega\tau)^{1-\alpha}\sin(\frac{\pi\alpha}{2})+(\omega\tau)^{2-2\alpha}} \qquad (1.5)$$

where χ_s and χ_t is adiabatic and isothermal magnetic susceptibility, ω and α represents angular frequency of magnetic field variation and relaxation distribution parameter.[18] Hence, τ at different temperatures can be obtained by fitting the isothermal ac magnetic susceptibility to the generalized Debye model. The fit of temperature-dependent τ to a model contributing from a sum of above relaxation mechanisms can lead out effective relaxation barrier (U_{eff}). The expression of the model is presented as following:

$$\tau^{-1} = AH^nT + \frac{B_1}{1+B_2H^2} + CT^m + \tau_0^{-1}\exp(-U_{eff}/kT) \qquad (1.6)$$

in which the above items are corresponding to direct, QTM, Raman, and Orbach processes, respectively.[19] In real cases, only one or two relaxation processes occur in one compound.

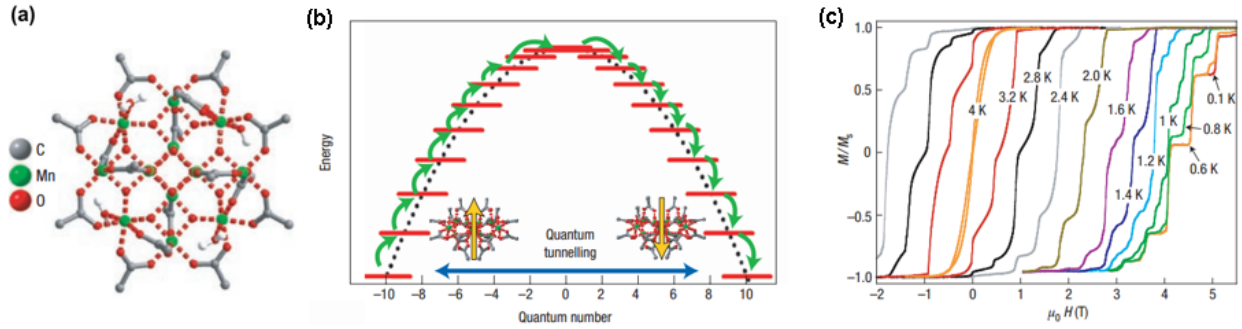

Figure 1.3 (a) Crystal structure, (b) schematic energy landscape with possible relaxation processes, and (c) magnetic hysteresis loops of single crystals for a Mn_{12} cluster SMM. (Reprinted from ref.25)

SMM behavior was first observed in a manganese cluster $[Mn_{12}O_{12}(O_2CMe)_{16}(H_2O)_4]\cdot 4H_2O$ in 1993 (Figure 1.3).[20] This cluster is a mixed-valence compound that has the valence state of $Mn(IV)_4Mn(III)_8$. The cluster has a S_4 symmetric structure with a $Mn(IV)_4O_4$ cubane locating at the core position and eight Mn(III) ion surrounding in periphery linked to the core through O^{2-} bridges. These Mn(III) ions exhibit strong Jahn-Teller effect and thus generate strong magnetic anisotropy

through spin-orbital coupling. Importantly, the orientations of the anisotropy axis for all Mn(III) ions are close to the main symmetric axis of the cluster, which leads to the cluster displaying strong axial anisotropy and thus exhibiting excellent SMM behavior. Magnetic investigation revealed that the Mn_{12} compound characterizes $S = 10$, $D = -0.5$ cm^{-1}, $U_{eff} = 60$ K and T_B = ca. 3 K. For this Mn_{12} cluster, the magnetization relaxation rate is significantly slow below the block temperature (10^{-7} s^{-1} at 2 K), which leads to remarkably wide magnetic hysteresis loops when external magnetic field directionally changed. The magnetization reversal rate becomes very fast with temperature increasing, which prevents this compound from being used as practicable memory devices. However, Mn_{12} family still represents the most extensively investigated SMMs.[20-25] Crystal structure, energy landscape and magnetic hysteresis loops for an example of Mn_{12} SMMs are given in Figure 1.14.[25]

Afterwards, research efforts were concentrated upon other polynuclear compounds with high spin ground states for increasing U_{eff}, and thus improving the T_B. The record breakthrough in polynuclear SMM system was achieved in a hexanuclear complex $[Mn^{III}_6O_2(Et\text{-}sao)_6(O_2CPh(Me)_2)_2(EtOH)_6]$ (Et-saoH$_2$ = 2-hydroxyphenylpropanone oxime), which has $S = 12$, $D = -0.42$ cm^{-1}, $U_{eff} = 86.4$ K and T_B = ca. 4.5 K.[26] From this view point, the anticipation for more efficient SMMs in polynuclear systems with large ground spin states was already under great challenge. Recent theoretical investigation revealed that the parameters (D and S^2) for determining the reversal barrier are correlative with each other, namely that the D value is in inverse proportion to the S^2 value.[27, 28] This limitation effect may be ascribed to that increase of paramagnetic ions in cluster leads to non-uniform alignment of the magnetic anisotropy axes of each ions and thus partial cancellation of local anisotropies, resulting in small overall anisotropy for the cluster. This theoretical finding drives the attention from polynuclear systems to mononuclear compounds for further development of excellent SMMs.

Mononuclear SMM, generally referred as single-ion magnet (SIM), was first reported in a family of lanthanide complexes [TBA][Pc$_2$Ln] (TBA = tetrabutylammonium, Pc = pthalocyanine, and Ln =

Tb or Dy) by Ishikawa and co-workers in 2003.[29] These SIMs display slow magnetization relaxation in the temperature range that much higher than that for polynuclear SMMs based on transition-metal ions. Afterwards, large amount of lanthanide-based mononuclear complexes manifesting excellent SIM behavior have been constantly reported.[30-35] Importantly, remarkable breakthrough of U_{eff} and T_B have been achieved in recently reported two lanthanide ion-based SIMs through artful chemical design. [Dy(bbpen)Br] displays slow magnetization dynamics with U_{eff} = 1025 K and T_B = 14 K (bbpen = N,N'-bis(2-hydroxybenzyl)-N,N'-bis(2-methylpyridyl)ethyle-nediamine (Figure 1.4).[34] And complex $[Dy(O^tBu)_2(py)_5][BPh_4]$ exhibits SMM behavior with U_{eff} = 1815 K and T_B = 14 K.[35] The common structural feature of these two complexes is that the lanthanide ions coordinated with much more electronegative ligands in the axial positions than these in equatorial positions thus produces strong axial magnetic anisotropies for the compounds. The large magnetic anisotropy of Ln-ions originates from their unquenched orbital angular momentum under ligand-field splitting.

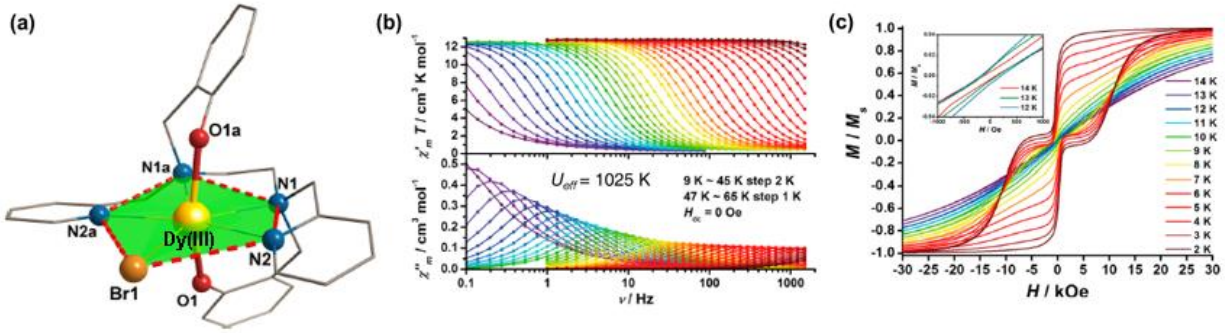

Figure 1.4 (a) Crystal structure, (b) ac magnetic susceptibility, and (c) magnetic hysteresis loops of [Dy(bbpen)Br] (Reprinted from ref.34).

Another important family of SIMs are 3d transition-metal ion-based SIMs. In contrast to mononuclear lanthanide complexes, the first-order orbital contribution for generating magnetic anisotropy in mononuclear transition-metal complexes is usually quenched by the large ligand-field splitting energy. The prevalent strategy in the search for 3d transition-metal ion-based SIMs is reducing the coordination number to minimize the quenching effect. This strategy started with the

discovery of slow magnetization relaxation behavior in three-coordinated high-spin Fe(II) complex K[(tpa^{Mes})Fe], as reported by Long and co-workers.[36] Soon later, the same group achieved a remarkable record of U_{eff} = −226 cm^{-1} (157.0 K) in a linear two-coordinated Fe(I) compound [K(crypt-222)][Fe(C(SiMe$_3$)$_3$)$_2$] (crypt-222 = 2.2.2-cryptand), which represents the largest U_{eff} among transition-metal ion-based SIMs (Figure 1.5).[37]Afterward, many low-coordination transition-metal ion-based SIMs, with metal ions of Fe(I, II), Co(II), Mn(III, IV), Ni(I, II), and Cr(II).[22, 38-44]

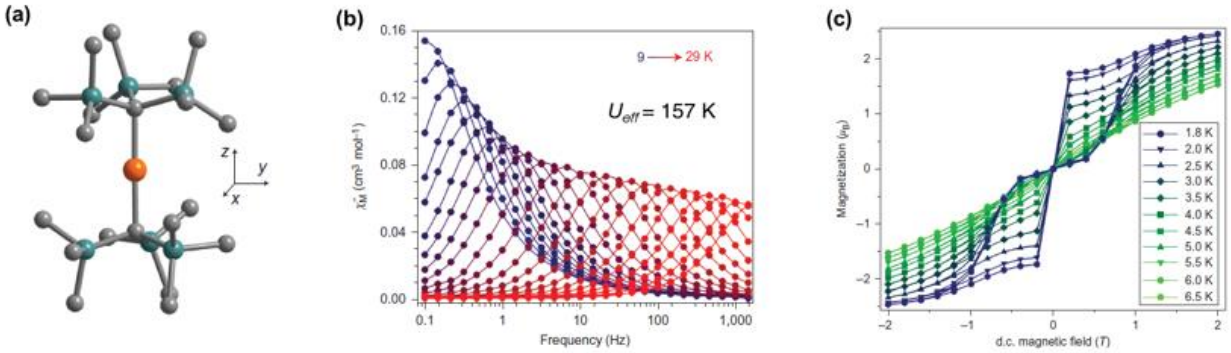

Figure 1.5 (a) Crystal structure, (b) ac magnetic susceptibility, and (c) magnetic hysteresis loops of [K(crypt-222)][Fe(C(SiMe$_3$)$_3$)$_2$] (Reprinted from ref.37).

One of the other available strategy to achieve transition-metal ion-based SIMs is controlling molecular symmetry through subtle chemical design. As mentioned forward, particularly efficient QTM will cause no detectable slow magnetization relaxation behavior for compounds. In some cases, QTM originates from lower molecular symmetry, which generates transvers magnetic anisotropy for the compounds. Therefore, increasing symmetry of molecule can favor the compound to exhibit slow magnetic relaxation behavior. This deduction is supported by a family of Fe(II) complexes with six tetrazole derivate as coordination ligands.[45, 46] [Fe^{II}(ptz)$_6$](BF$_4$)$_2$ (ptz = 1-propyltetrazole) exhibits thermally induced spin transition behaviors, and possesses two low-spin state phases (**LS$_\alpha$** and **LS$_\beta$**) determined by the rate of lowering the temperature.[45] **LS$_\alpha$** has C_i symmetry and **LS$_\beta$** possesses higher D_{3d} symmetry. SIM behavior can only be obtained for the light-excited state of **LS$_\beta$** (Figure 1.6).

Photo-switchable SIM behavior is also observed for a similar Fe(II) compound $[Fe^{II}(mtz)_6](CF_3SO_3)_2$ (mtz = 1-methyltetrazole). $[Fe^{II}(mtz)_6](CF_3SO_3)_2$ displays thermally induced incomplete spin transition, and the remnant high-spin Fe(II) sites at low temperature features D_{3d} symmetry.[39] Hence, the low temperature phase of $[Fe^{II}(mtz)_6](CF_3SO_3)_2$ exhibits field-induced SIM behavior, and the SIM behavior can be switched off and on through the red and green light, respectively.

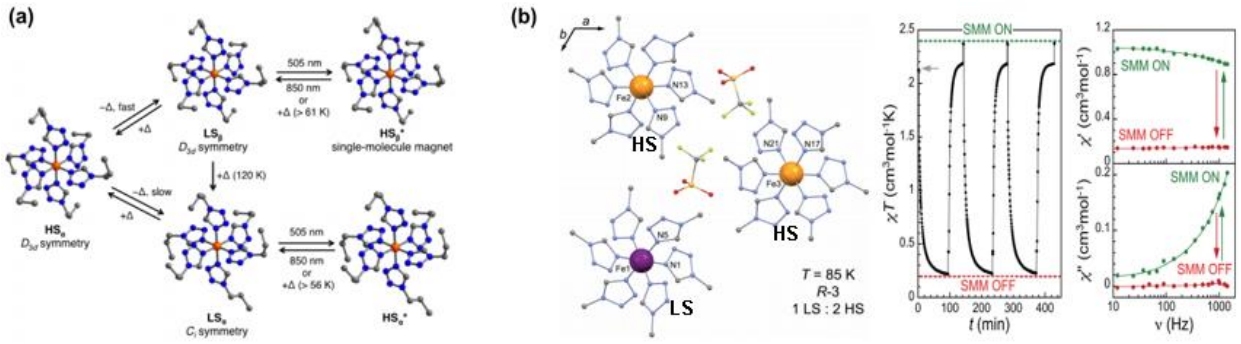

Figure 1.6 (a) Convention between five distinct states of complex $[Fe^{II}(ptz)_6](BF_4)_2$; (b) Low temperature crystal structure and photo-switching dc and ac magnetic data of complex $[Fe^{II}(mtz)_6](CF_3SO_3)_2$. (Reprinted from ref.45, 46)

Following the target to improve information density of in the memory media, the ultimate limit is that one-bit information can be stored in only one single atom. This target can be achieved via realizing magnetic remanence only in a single atom. This type of materials can be called single-atom magnets (SAMs), which have been successfully achieved in holmium (Ho) atoms by F. Donati and co-workers (Figure 1.7).[47] When the Ho atom is positioned on an oxygen atom of MgO surface, it displays strong magnetic anisotropy due to its extremely asymmetric electrostatic surrounding. Additionally, the C_{4v} symmetry structural feature of the Ho on MgO surface prevents the generation of rhombic anisotropy, and thus no QTM effect. Therefore, the Ho atoms on MgO surface exhibits slow magnetization relaxation with magnetic hysteresis up to 30 K, which is significantly higher than the blocking temperature for any SMMs. Soon later, Natterer and co-workers confirmed that the Ho atoms on MgO surface independently hold their magnetic information for many hours.[48] More

impressively, they realized information writing and reading through current pulses and tunneling magnetoresistance with a scanning tunneling microscope.

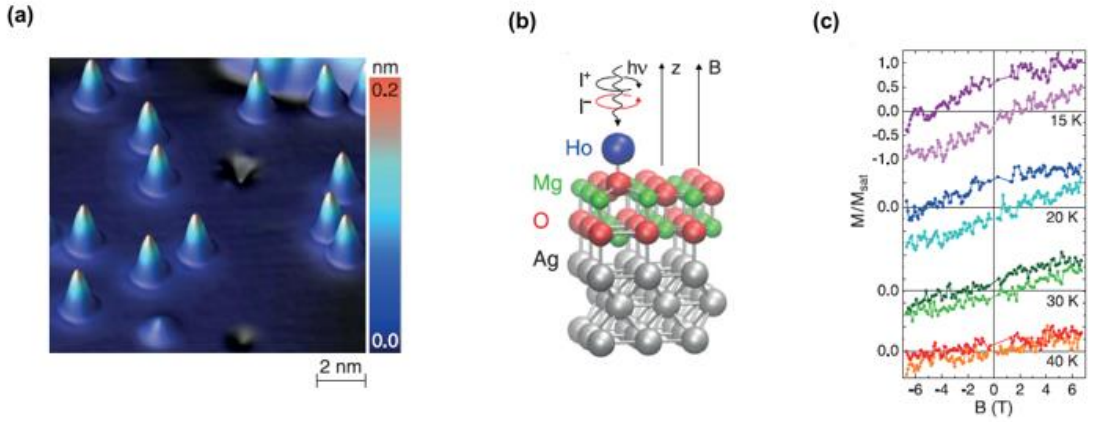

Figure 1.7 (a) Constant-current scanning tunneling microscopy image, (b) adsorption geometry determined by density functional theory and X-ray absorption spectra, and (c) magnetic hysteresis loops at different temperatures of Ho atoms on the surface of MgO layer. (Reprinted from ref.47)

SMMs, SIMs and SAMs can be classified as zero-dimensional magnets. Another important species of low- dimensional magnetic materials exhibiting slow magnetization relaxation are single-chain magnets (SCMs). SCMs generally possesses higher T_B than these of SMMs, and thus receive great research attention. SCMs are the Ising chains that feature strong exchange interactions of magnetic centers in one dimension, while exhibit very weak magnetic interaction in the other two dimensions. Ising chain requests the spin carriers displaying strong axial magnetic anisotropy. Furthermore, the Ising chains must have net spin, that is, the spin from different carriers cannot be mutually canceled. The weak magnetic interactions in the other two dimensions decedent upon the sufficiently large separation between adjacent chains.

In 1963, Glauber predicted that Ising magnetic chains would display slow magnetization relaxation and built the Glauber model with Hamiltonian of $\hat{\mathrm{H}} = -2J\sum_{i=1}^{L}\sigma_i\sigma_{i+1} - g\mu_B H\sum_{i=1}^{L}\sigma_i$, where J ferromagnetic exchange constant between spin units σ, g and μ_B stands for gyromagnetic factor and Bohr magneton.[48] Gatteschi confirmed Glauber's predication with observation of slow magnetic

relaxation in compound CoPhOme.[49] After that, lots of SCMs, including Mn(III)-Ni(II) ferromagnetic chains, Fe(III)-Co(II) ferromagnetic chains, and homo-spin Co(II) ferromagnetic have been reported.[50-51] Recent achievement in this field is the development of SCM with remarkable energy barrier in cyanide-bridged coordination polymers (As shown in Figure 1.8).[52] It should be noted that Glauber model only can be used for the description of strict Ising-type states. Hence, an anisotropic Heisenberg chain model with Hamiltonian of $\hat{H} = -2J\sum_{i=1}^{L} S_i S_{i+1} + D\sum_{i=1}^{L} {S_i}^2 - g\mu_B H\sum_{i=1}^{L} S_i$ is widely used to depict SCMs.

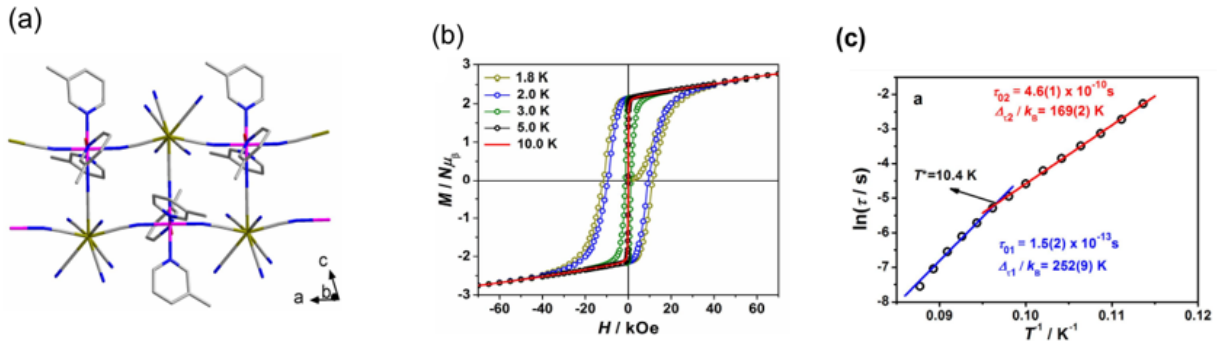

Figure 1.8 (a) crystal structure, (b) magnetic hysteresis loops , and (c) temperature-dependent of relaxation time for a cyanide-bridged single-chain magnet. (copied from 51).

1. 3 Spin Number Transition in Coordination Complexes

Molecular materials with two different electronic states determined by external factors generally exhibit switchable physical properties, and thus can serve as electronic devices.[52-54] Transition metal complexes may exhibit spin numbers change due to that some transition metal ions have tunable oxidation states and electronic conformations. Various coordination complexes manifest different type of spin number change, including electron conformations changing in one metal center (spin-transition complexes), electron transfer between two different spin carriers (metal-to-metal charge transfer or metal-to-ligand charge transfer), or coupled process (charge transfer coupled spin transition).[9,10,52-56] One of the most attractive points of electronic bistable systems is that the electronic

states can be controlled by external stimuli in solid state.

Octahedral transition metal complexes with metal centers possessing d^4–d^7 conformations can adopt two distinct spin states, low-spin (LS) or high-spin (HS), determining by the coordination ligand field strength. When the break-up energy of d orbitals close to the mean pairing energy for two electrons pairing to one orbital, the arrangement of *d*-electrons may realign under suitable external stimuli, such as temperature (*T*), light (*hv*), or pressure (*P*), namely spin transition (spin crossover) occurs in the metal centers. Generally, spin transition behavior of coordination compound is accompanied by the variation of it's optical, mechanical, and dielectric properties.[9,10] Figure 1.10 shows the scheme of spin transition behavior for Fe(II) complexes, which are typical family in spin transition systems.

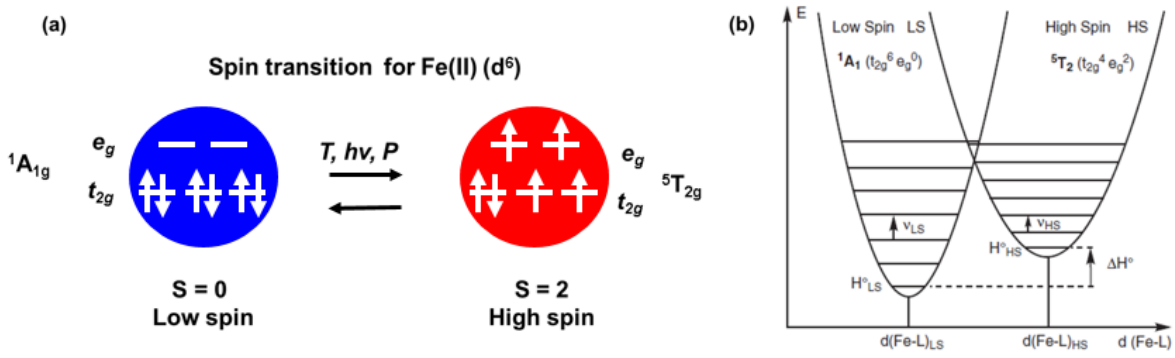

Figure 1.9 (a) Schematic description of spin transition for Fe(II) complex. **(b)** Potential energy wells of LS and HS for Fe(II) complex as a function of coordination bond distance (copy from ref.1).

Light switchable spin transition is depicted as light-induced excited spin-state trapping (LIESST) effect, whose mechanism is presented in Figure 1.10 (green part). Under photo-irradiation, the ground state $^1A_1$ for low spin Fe(II) is excited to the singlet state $^1T_2$ (or $^1T_1$), which fast relaxes to a metastable quintet state $^5T_2$ pass through the triplet states of $^3T_2$ and $^3T_1$. After switching off the light, the metastable state $^5T_2$ will slowly relax back to the initial ground state $^1A_1$. Revise LIESST effect can also be induced, the process of which is shown in red part of Figure 1.10. Structural analyses

revealed that the light-excited metastable state characterizes similar structure with the thermally accessible high spin phase, but not identical.[57,58] Additionally, the solid structures of coordination compounds would change with the variation of applied pressure, which always accompanied with coordination bonds strength change, and thus lead to the variation of break-up energy of ligand field. This effect may also result in rearranging *d*-electrons, namely, spin states change for the metal centers.

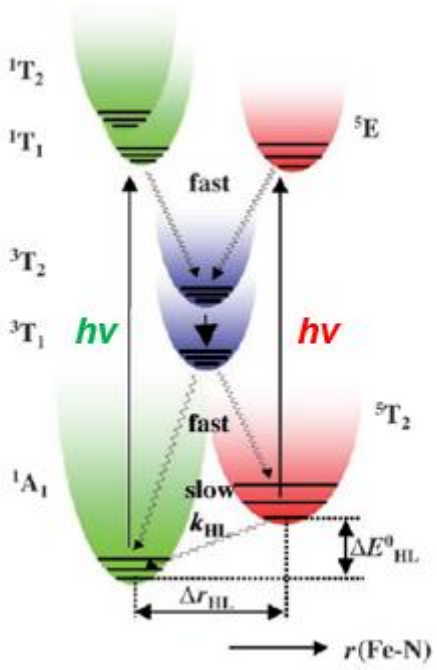

Figure 1.10 Schematic description of LIESST (green part) and revise LIESST (red part) for Fe(II) complex. (Copied from ref.56).

The investigation on spin transition compound can be date back to 1931, in that year spin transition phenomenon was firstly discovered on a Fe(III) compound by Cambi. After that, materials manifesting spin transition behaviors have been extensively studied for their potential application in electronic devices, such as information storage carriers, thermal or photo switches. Up to now, spin transition behaviors have been observed in mononuclear, multinuclear, and coordination polymeric complexes containing Fe(II), Fe(III), Co(II), Co(III), Mn(III), and Cr(II) ions.[9,10, 59, 60] The most important tasks for promoting spin transition compounds to final application are the exploitation of

compounds exhibiting abrupt spin transition at around room temperature with large thermal hysteresis loops, and merging spin transition into other functional materials.

Spin transition behaviors are deeply influenced by intermolecular interactions.[61,62] In 1998, O. Kahn and co-workers pointed out that strong interactions are in favor of intermolecular cooperative, and thus the material may exhibit sharp thermal induced spin transition with hysteresis—a kind of magnetic bistability.[52] The capability of manifesting magnetic bistability around room temperature is one of the key advantage for spin transition complexes to use as memory devices compared with other potential molecular based magnetic bistable materials. A Fe(II) complex shows spin transition with a 70 K thermal hysteresis loops near room temperature is presented in Figure 1.11.[63] The development in spin transition compounds with thermal hysteresis loops were summarized in a recent review paper.[60] The research effort in this field is developing spin crossover compounds with wide hysteresis loops.[64-68]To the best of my knowledge, the widest thermal hysteresis loops (ca. 140 K) were observed in complexes $Fe^{II}[(3\text{-bbp})_2](CF_3SO_3)_2\cdot H_2O$ ($T_{1/2}\uparrow$ = 147 K, $T_{1/2}\downarrow$ = 285 K, 3-bbp = 2,6-bis(pyrazolyl-3-yl)pyridine) and $Co^{II}(C12\text{-terpy})_2(BF_4)_2$ (C12-terpy = 4'-dodecyloxy-2,2':6',2''-terpyridine).[69,70] Another interesting findings are that the width of thermal hysteresis loops are dependent on the sample size and the rate of temperature variation.[71-73]

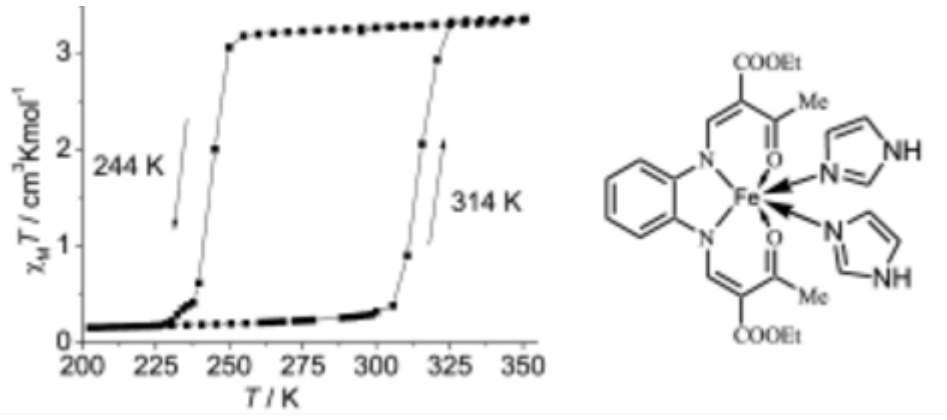

Figure 1.11 Magnetic data and schematic structure for a Fe(II) complex showing thermal induced spin transition with a 70 K thermal hysteresis loop. (Copy from ref. 63).

Merging spin transition with other functions to exploit multifunctional materials is another important mission for the application of spin crossover materials. As mentioned before, spin state variation for complexes normally accompanied with coordination bonds change, and thus can induce mechanical effects at macro-level. This phenomenon was clearly observed in a bilayer film with a spin transition layer and an aluminum layer.[74] The bilayer film obviously bent around the spin transition temperature, similar to the bending phenomenon observed in bimetallic strips with variation of temperature for their distinct thermal expansion. Furthermore, merging spin-crossover materials with conducting materials can also generate synergistic effect, that is, spin transition can modulate the conductivity.[75-77] For instance (Figure 1.12),[75] complex $[Fe^{II}(tpma)(xbim)](ClO_4)(TCNQ)_{1.5}\cdot DMF$ (tpma = tris(2-pyridylmethyl)amine; xbim = 1,1′-(α,α′-o-xylyl)-2,2′-bisimidazole; TCNQ = 7,7.,8,8.-tetracyanoquinodimethane) is co-crystal of the spin crossover cations $[Fe^{II}(tpma)(xbim)]^{2+}$ and partially charged $TCNQ^{\cdot\delta-}$ radicals, which locate in separation layers in the crystal lattice. The activation energy (E_a) reflecting the conductivity for the complex changed in the temperature range corresponding to completion of spin states variation from high spin to low spin.

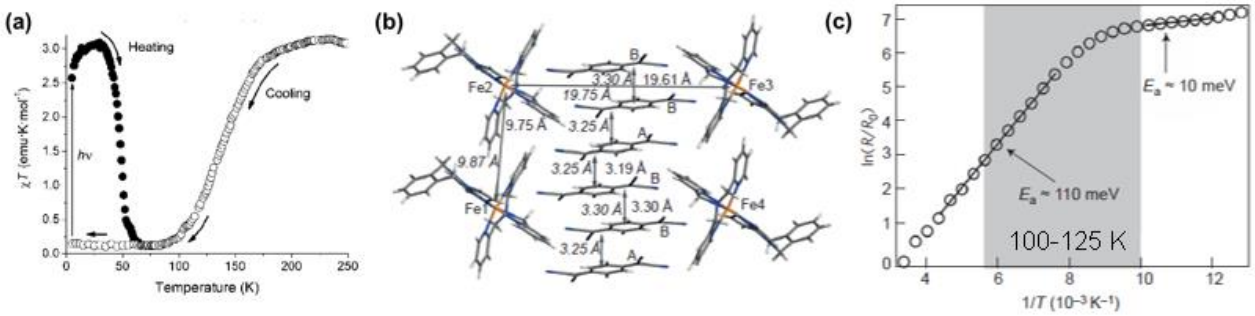

Figure 1.12 (a) Magnetic data, (b) crystal packing structure showing interatomic distances at 230 K (italic font) and 100 K (regular font), and (c) the variation of activation energy (E_a) with temperature for $[Fe^{II}(tpma)(xbim)](ClO_4)(TCNQ)_{1.5}\cdot DMF$. (Copy from ref.75).

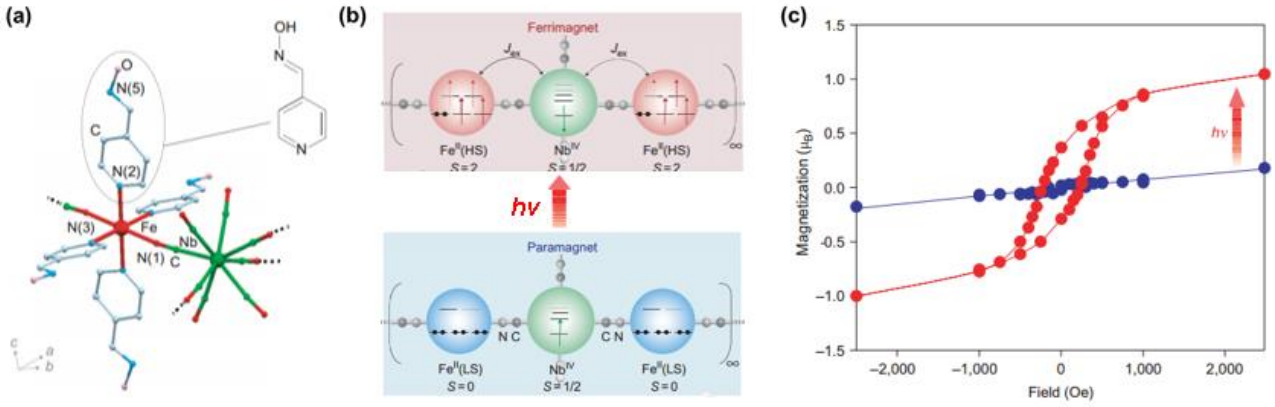

Figure 1.13 (a) Crystal structure showing coordination surroundings for Fe(II) and Nb(IV), (b) schematic description of photo-induced ferrimagnetic ordering, and (c) magnetization data before (blue) and after (red) irradiated by 473 nm light for $Fe_2[Nb(CN)_8](4\text{-pyridinealdoxime})_8 \cdot 2H_2O$ (Copy from ref.78).

Another significant strategy is utilizing LIESST effect to switch some other physical properties. A recent achievement is that photo-induced long-range magnetic ordering has been observed in a Fe–Nb-based metal–organic framework $Fe_2[Nb(CN)_8](4\text{-pyridinealdoxime})_8 \cdot 2H_2O$ (Figure 1.13).[78] The Fe(II) sites in this complex exhibited thermal and light induced spin transition. In the low temperature without photo irradiation, the paramagnetic Nb(IV) and the diamagnetic low spin Fe(II) were linked by cyanide bridges in an alternating style. After irradiated with 473 nm light, the Fe(II) sites become high spin state through LIESST process, and show strong antiferromagnetic coupling ($-6.9\ cm^{-1}$) with the Nb(IV) ions through cyanide bridges, and thus display ferromagnetic ordering below 20 K. Light controlled single ion magnets and single chain magnets through LIESST effect have also been successfully achieved.[45,46, 79]

1. 4 Charge-Transfer Coupled Spin-Transition in Coordination Complexes

Charge transfer is a common electron dynamic behavior for coordination compounds containing metal ions with variable oxidation states. It is well known that charge transfer between two electronic

carriers is a kind of oxidation-reduction reaction, which requires the electron donors and acceptors having appropriate redox potentials. For coordination compounds, charge transfer can occur between two redox-active metal ions, or between a redox-active metal ion and a redox-active organic ligand.[2] More specifically, charge transfer in coordination compound requires different electron carriers possessing comparable energies of frontier orbitals and efficient electron transition pathway.

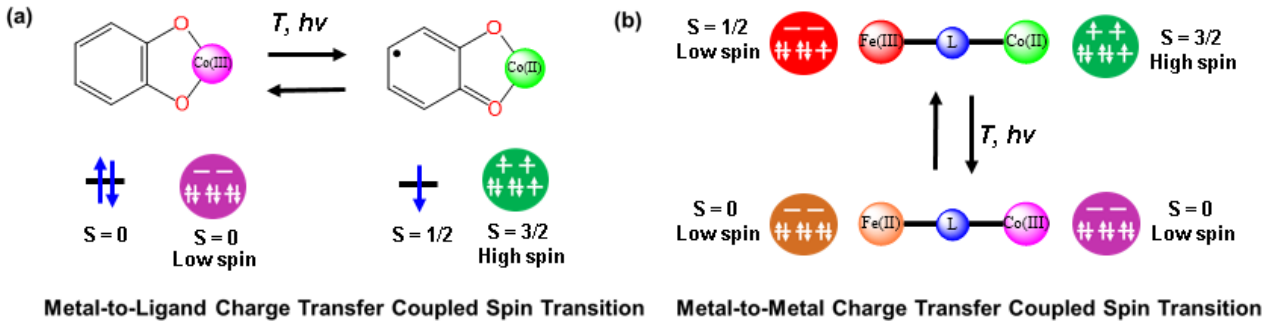

Figure 1.14 Schematic description of metal-to-metal charge transfer coupled spin transition (a), and metal-to-ligand charge transfer (b).

Furthermore, spin transition can be induced simultaneously in charge transfer process for complexes containing metal ions with d^4–d^7 conformations, the main effect that leads to significant magnetic susceptibility change in coordination compounds involving charge transfer.[9,10] Generally, the ligand field splitting of metal ion in high oxidation state is larger than that of metal ion in low oxidation state. Thus, charge transfer induced spin transition can be achieved if the ligand field splitting meeting the request of low spin in high oxidation state and high spin in low oxidation state. Figure 1.14 gives out the typical charge transfer process that coupled with spin transition in coordination compounds.

Thermal induced valence tautomeric transition is also an entropy driven process (Figure 1.15). The low spin state of metal ion is the quantum-mechanical ground state. While, the high spin state is the entropically favorable state, whose enthalpy is only a little larger than that of low spin state. Hence,

the spin state of metal ion will change from low spin to high spin with temperature increasing. The higher entropy of high spin state contributes from both electronic and vibrational entropy. The electronic entropy is mainly originated from spin degeneracy, since orbital degeneracy is generally removed in the spin transition complexes due to their non-ideal symmetrical structures. The coordination bonds for high spin phase feature longer distance because of the occupation of two electrons in the e_g orbitals showing antibonding character, which results in shallower potential well and lower metal-ligand vibrational frequency (more closely located vibrational levels).

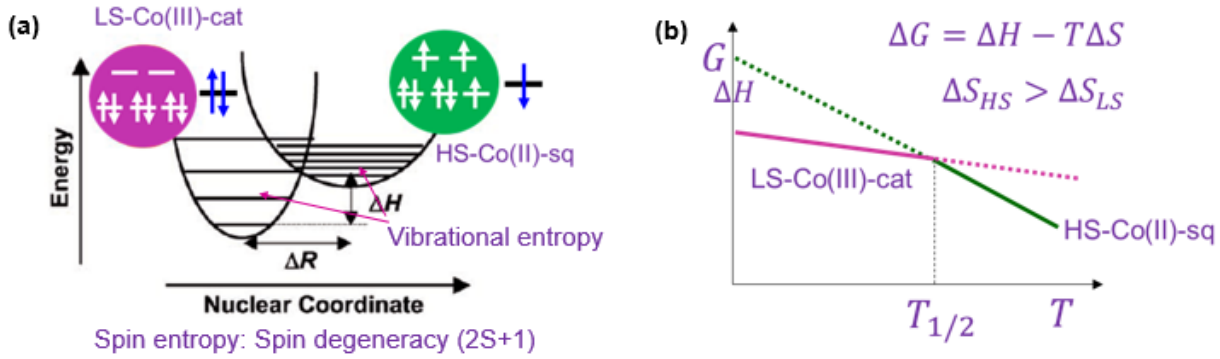

Figure 1.15 Entropy-driven process for valence tautomeric transition.

The particular interest for this type compounds is also toward reversible abrupt transition with large thermal hysteresis loops near room temperature, which is deep dependent on the intermolecular interaction. The intermolecular interaction affect the valence tautomeric transition base on the following analysis. Intermolecular interaction can be expressed: $\boldsymbol{N \times \mathbf{N}}$, and thus HS-LS interaction has this form: $\boldsymbol{2\{xN \times (1-x)N\}}$, which will lead to increase system energy. The mole Gibbs free energy including intermolecular contribution can be expressed: $\boldsymbol{\mathbf{G} = x\mathbf{G}_{\mathbf{HS}} + (1-x)\mathbf{G}_{\mathbf{LS}} - T\mathbf{S}_{\mathbf{mix}} + \Gamma x(1-x)}$. And the corresponding extrema of G can be obtained by setting the partial derivatives equal to zero: $(\partial \mathrm{G}/\partial x)_{T,P} = \mathrm{G_{HS}} - \mathrm{G_{LS}} + RT\ln[x/(1-x)] + \Gamma - 2\Gamma x = 0$. Hence according to this analysis, strong intermolecular interaction will lead to large energy cost in

spin number transition system. When the interaction parameter r is larger than the twice of R $T_{1/2}$, the temperature vs. high-spin fraction has the shape of a double fold with two external branches corresponding to minimal G, and the AB range corresponding to maximal G. In this case, with temperature increase before $T_{1/2}\uparrow$, most of the molecules will keep in low spin state to minimal the system energy. At the temperature of $T_{1/2}\uparrow$, the relatively large amount of high spin molecules make the system unstable. And at this temperature point, the secondary minimal Gibbs energy appears, thus with temperature further increase, the system has no other selection than to jump to the second minimal G, namely the low-spin molecules abrupt transition to a high spin state. The cooling process exhibits similar behavior with lower transition temperature $T_{1/2}\downarrow$, thus producing thermal hysterses.

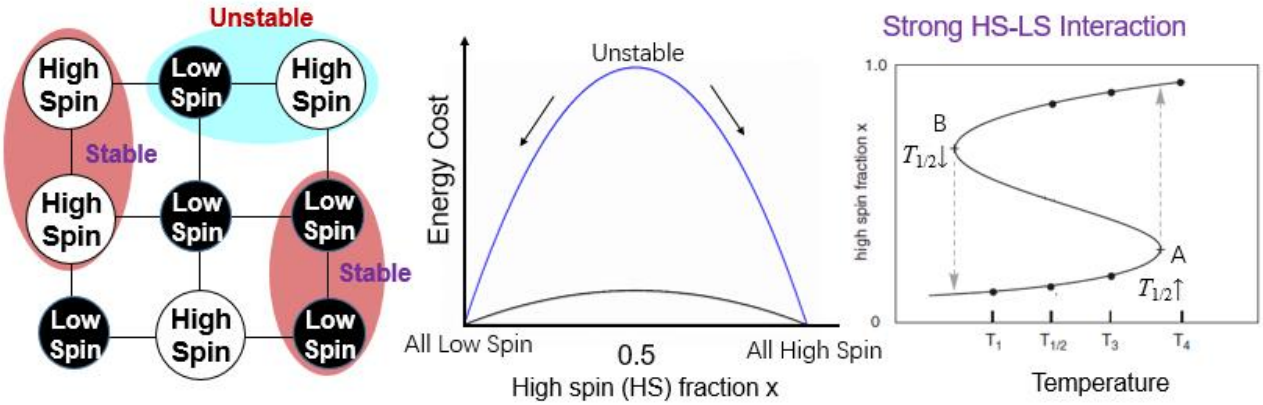

Figure 1.16. Influence of intermolecular interaction on valence tautomeric transition.

However, examples of valence tautomeric compounds exhibiting thermal hysteresis effects are relatively rare.[89-92] Jung and co-workers reported a valence tautomeric compound, [Co(Py_2O)(3,6-dbdiox)$_2$] (Py_2O = bis(pyridyl)ether), displaying a large thermal hysteresis loop (230 K, $T_{1/2}\uparrow$ = 330 K, $T_{1/2}\downarrow$ = 100 K) which is obviously larger than the widest ones for spin transition complexes.[89] Structural analyses of this compound revealed that the hysteresis effect was related to structural conformation change accompanied with the valence tautomeric transition. The coordination ligand Py_2O underwent a variation from a planar conformation in low temperature phase to a non-planar conformation in high temperature phase, imposing an energy barrier to the electron dynamics for this

complex. Another important factor to ensure the conformation change is sufficient space in crystal packing structure. Systemic study on a family of *trans*-[Co(4-x-Py)(dioxolene)$_2$] (x stands for different substituents) revealed that intermolecular interactions (hydrogen bonds) play a significant role to affect their valence tautomeric transition behaviors.[90] Among this family of [Co(4-x-Py)(dioxolene)$_2$], thermal hysteresis and trapping effects were only observed in complexes with intermolecular hydrogen bonds directly formed between the Co molecular units.

Photo-induced valence tautomerism has also been well investigated in Co-dioxolene compounds.[9, 10,55] In general light-induced valence tautomeric process, the ligand-to-metal charge transfer (LMCT) band of *ls*-Co(III)-cat (*ls* = low spin, cat = *o*-catecholate) phase is excited under photo-irradiation, producing a LMCT excited state. The LMCT excited state then quickly relaxes to the metastable *hs*-Co(II)-sq (*hs* = high spin, sq = *o*-semiquinone) state (Figure 1.15b).[93-95] Conversely, metastable *ls*-Co(III)-cat state can also be achieved via light excitation of the metal-to-ligand charge transfer (MLCT) band of the *hs*-Co(II)-sq phase.[96,97] The light excited metastable states in both cases hold the lifetime in nanoseconds before relaxing back to their initial phases.[10, 55] Unlike the LIESST effect that can lead to complete spin transition, the light induced valence tautomerism only occurs in a portion of solid sample. The incomplete photo-induced valence tautomeric transition is generally due to deep color of the sample, which prevents the solid sample being fully irradiated, or may be related to overlap of the transitions of two tautomeric phases producing a photostationary state.[95] One of intriguing property involving light-induced valence tautomerism is photomechanical effect. Irradiating crystal sample of one-dimensional complex [*ls*-Co^{III}-(3,6-dbsq)(3,6-dbcat)(pyz)]$_n$ (pyz = pyrazine) in one side resulted in reversible crystal bending.[98] This photomechanical effect is attributed to the longer coordination bonds distance of the light excited phase. Much great photomechanical effect has been observed in [Rh^{I}(3,6-dbsq)(CO)$_2$].[99]

As for polynuclear coordination compounds, another important species of charge transfer is metal-to-metal charge transfer (MMCT), which requires different metal ions possessing close energies of

d-orbitals be linked by appropriate chemical bridges. Like valence tautomerism, MMCT coupled with spin transition (CTCST) is generally significant for magnetic materials. In 1996, Sato and co-worker reported the first example of metal-to-metal CTCST in a three-dimensional Prussian blue complex $K_{0.2}Co_{1.4}[Fe(CN)_6]\cdot 6.9\ H_2O$, in which the diamagnetic unit *ls*-Fe(III)-CN-*ls*-Co(III) converts to the paramagnetic unit *ls*-Fe(II)-CN-*hs*-Co(II) upon temperature increasing or light irradiation.[100] More interestingly, the light-excited state *ls*-Fe(II)-CN-*hs*-Co(II) exhibits strong antiferromagnetic interaction, and thus the Prussian blue complex is turned to long-range ferromagnetic ordering state, which holds lifetime of several days at 5 K. After this discovery, CTCST behavior has been extensively investigated in Prussian blue systems, including coordination complexes be composed of Fe-CN-Co, W-CN-Fe, Os-CN-Fe, W-CN-Co, Fe-CN-Mn, Os-CN-Co, Mo-CN-Cu and W-CN-Fe/Co. Various molecular structures, from initial three-dimensional structures to recently reported dinuclear structure, have been obtained in cyanide bridged metallic complexes exhibiting CTCST behavior via artful chemical modification.[10, 101-120] It is worthy to note that thermally induced CTCST is also an entropically driven process and the transition temperature can be controlled by ligands (Figure 1.17).

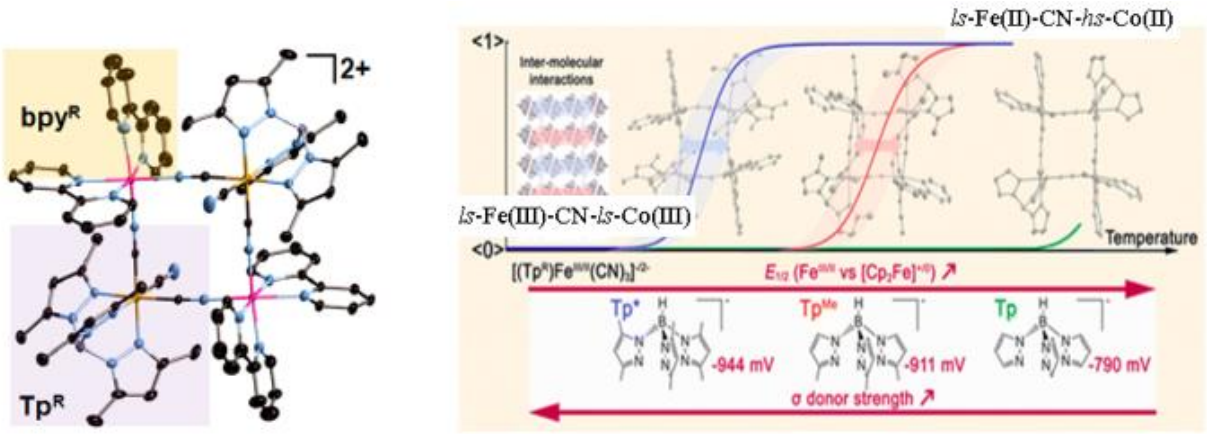

Figure 1.17 Example of turning CTCST transition temperature via modifying coordination ligands on Fe sites for a family of cyanide bridged FeCo square complexes (Copy from ref.110).

Investigation on metal-to-metal CTCST complexes is also focusing on development of multifunctional materials. A recent achievement is that CTCST behavior was coupled with controlling

conductivity and ferromagnetic single-chain magnet in a chiral cyanide bridged FeCo one-dimensional coordination polymer $[Co^{II}((R)\text{-pabn})][Fe^{III}TP(CN)_3](BF_4)\cdot MeOH\cdot 2H_2O$ (Tp = hydrotris(pyrazol-1-yl)borate, (*R*)-pabn = (*R*)-N(2),N(2′)-bis(pyridin-2-ylmethyl)-1,1′-binaphtyl-2,2′-diamine) (Figure 1.19).[104] This FeCo chiral chain complex exhibits temperature induced CTCST behavior with an adjustable thermal hysteresis loop, and the transition from the low temperature phase *ls*-Fe(III)-CN-*ls*-Co(III) to high temperature phase *ls*-Fe(III)-CN-*hs*-Co(II) accompanied with conductivity convention from insulating to semiconducting. At low temperature, the *ls*-Fe(III)-CN-*ls*-Co(III) phase can be excited to metastable *ls*-Fe(III)-CN-*hs*-Co(II) phase, which displays single-chain magnet behavior. Additionally, the same group reported a cyanide bridged Fe_4Co_2 hexanuclear complex showing photo switchable single-molecular magnet behavior through light excited CTCST.[74] Another significant achievement is the observation of electric field induced CTCST in complex 3-D-$[Co^{II}(pm)_2]_2[Co^{II}(H_2O)_2][W^{V}(CN)_8]_2\cdot 4H_2O$, which provides a promising avenue to achieve practicable electronic devices.[82]

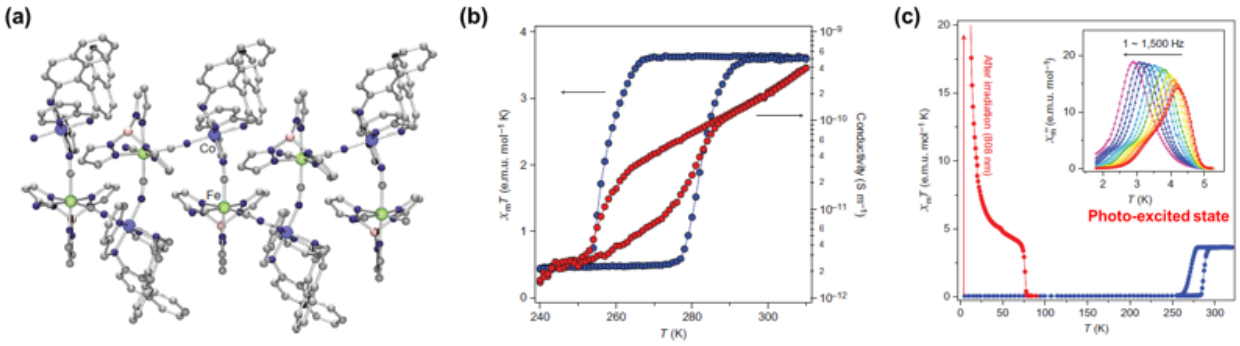

Figure 1.18 (a) crystal structure, (b) thermal switched magnetic susceptibility (blue) and conductivity (red), and (c) photo switched single-chain magnet behavior for complex $[Co^{II}((R)\text{-pabn})][Fe^{III}TP(CN)_3](BF_4)\cdot MeOH\cdot 2H_2O$ (Copied from ref.104).

In charge transfer systems, although pronounced magnetic properties variation generally induced by CTCST, interesting dynamic magnetic behaviors have also been observed in some coordination

complexes only involving charge transfer process. For instance, valence tautometism without coupling spin transition has been observed in a dinuclear ytterbium compound [(dpp-bian)Yb(μ-Cl)(1,2-dimethoxyethane)]$_2$ (dpp-bian = 1,2-bis[(2,6-diisopropylphenyl)imino]acenaphthene), which exhibits uncommon magnetic variation with temperature change (Figure 1.19a).[121] The low temperature phase Yb(III)-(μ-Cl)$_2$-Yb(III) with higher magnetic moment (6.6 μ_B) changes to the high temperature phase Yb(III)-(μ-Cl)$_2$-Yb(II) with lower magnetic moment (5.2 μ_B) upon heating via charge transfer, and the reverse processes generate a thermal hysteresis loop (7 K). Another well-known materials that display charge transfer induced magnetic dynamics are compounds containing Mo-CN-Cu units, in which the Mo(IV)-CN-Cu(II) state can be induced to the Mo(V)-CN-Cu(I) state via photo irradiation (Figure 1.19b).[122,123] Although the total spin quantum numbers are not change before and after irradiation, the light-excited metastable Mo(V)-CN-Cu(I) magnetically coupled, and thus leads to magnetic susceptibility increasing. Charge transfer induced magnetic variations have also been observed in a cyanide bridged WFe cluster and a cyanide bridged FeFe one dimensional coordination polymer.[124, 125]

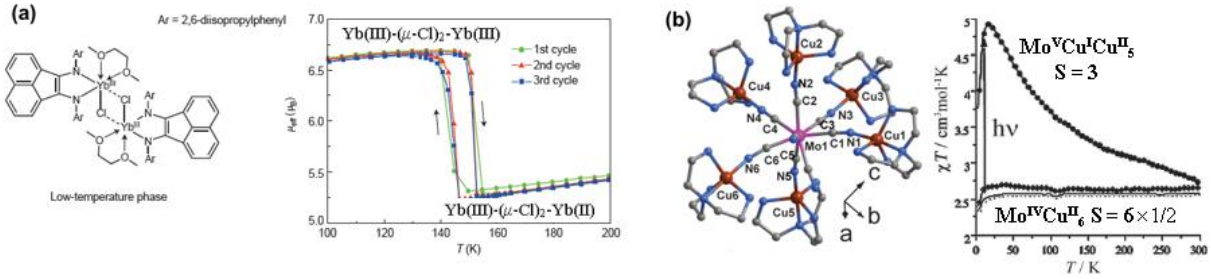

Figure 1.19 (a) Schematic structure and temperature dependent magnetic moment for [(dpp-bian)Yb(μ-Cl)(1,2-dimethoxyethane)]$_2$ (Copy from ref.121); (b) Crystal structure and temperature dependent magnetic susceptibility before and after photo irradiation for a cyanide bridged heptanuclear MoCu$_6$ complex (Copy from ref.124).

1. 5 Overview and Scope of This Thesis

As introduced above, spin state transition behaviors are significant for switchable physical properties. Since spin state is characterized by total spin direction and total spin number, spin state transition can be spin orientation flipping or spin number change. Importantly, these spin state transition behaviors are deeply influenced by the molecular components, molecular structures and intermolecular interactions, which can be carefully adjusted via artful chemical modulation and synthesis controlment. Our group is focusing on the realization of spin state transition in coordination compounds, and the revelation of the correlation of magnetic properties and molecular structures. Up to now, lots of coordination complexes that feature interesting spin state transition behaviors, and thus showing switchable magnetic properties under external stimuli, have been developed by our group members. In this thesis, I carried out the present research work as a prolongation of our previous investigation, which will be discussed in the following content.

In **chapter 1**, the research background on magnetic bistable compounds and scope of my research work is briefly introduced.

In **chapter 2**, an octa-coordinated Fe(II) complex, $[Fe^{II}(dpphen)_2](BF_4)_2 \cdot 1.3H_2O$ (dpphen = 2,9-di(pyrazo-1-yl)-1,10-phenanthroline) with a pseudo-D_{2d} symmetric metal center showing slow spin direction transition (slow magnetic relaxation) is reported. This Fe(II) complex slow magnetization dynamic (single-ion magnet, SIM) behavior since this it possesses strong uniaxial magnetic anisotropy. The uniaxial magnetic anisotropy for this high-coordinated Fe(II) is confirmed by magnetic measurement, high-frequency/field electron paramagnetic resonance (HF-EPR) studies, and *ab initio* calculations, which reveal that it has a negative axial zero-field splitting ($D \approx -6.0$ cm^{-1}) and a small rhombic zero-field splitting ($E \approx 0.04$ cm^{-1}). More interestingly, the magnetic units $[Fe^{II}(dpphen)_2]^{2+}$ arranged parallel to each other with their magnetic easy axis near to the crystalline *c*-axis, and thus serves as a perfect object for examining the fitness of experiment results and

theoretical results. Under applied dc magnetic fields, the octa-coordinated Fe(II) complex exhibits SIM behavior at low temperature. Fitting the relaxation time with the Arrhenius mode combining Orbach and tunneling terms affords a good fit to all the data and yields an effective energy barrier (17.0 cm^{-1}) close to the energy gap between the ground state and the first-excited state. The origin of the strong uniaxial magnetic anisotropy for this complex has been clearly understood from theoretical calculations. Generally, slow magnetization dynamics in transition-metal compounds are prevalently via reducing coordination numbers to reduce the orbital quenching effect, especially for the non-Kramers ions. Thus, our results provide a new strategy for realizing slow magnetization dynamics in high-coordinated transition complexes.

Scheme 1.1. Slow magnetic relaxation in an octa-coordinated Fe(II) complex.

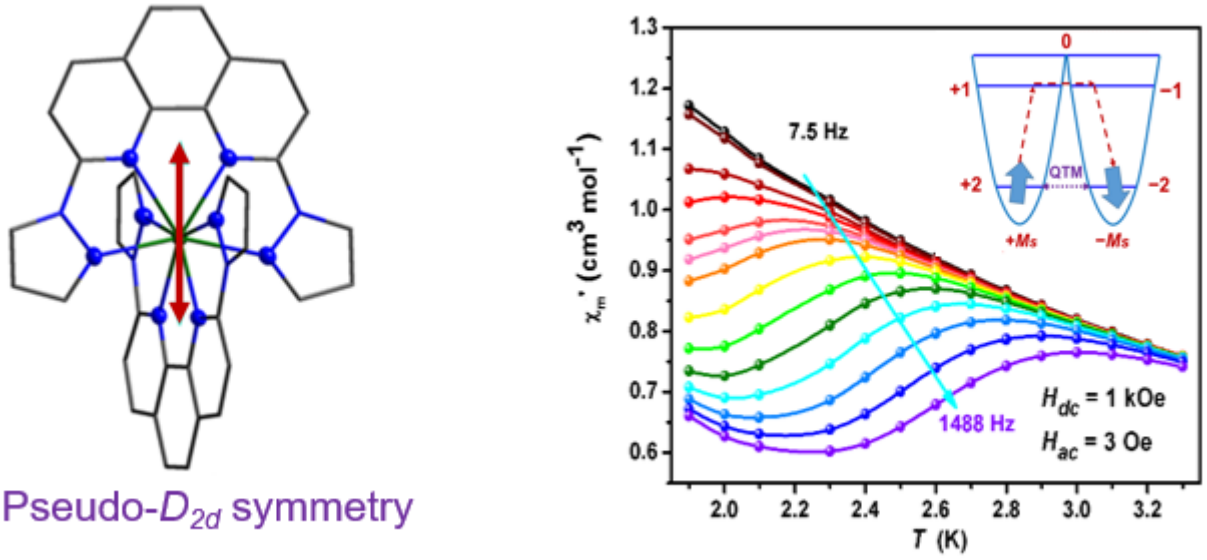

In **chapter 3**, in order to observe charge transfer coupled spin transition (CTCST) behavior in cyanide-bridged Fe^{II}/Fe^{III}, ligand (1,4-(1H-1,2,4-triazole)butane, btb) with stronger π-acceptor ability has been used. Two new cyanide-bridged Fe^{II}/Fe^{III} mixed-valence compounds are presented, which were obtained via cyanoferrate ($[Fe^{III}(Tp)(CN)_3]^-$, Tp = hydrotris(pyrazolyl)borate) and flexible ligand btb under different synthesis conditions. One of these two new compound

$\{[Fe(Tp)(CN)_3]_2Fe(btb)\cdot H_2O\}_n$ is a cyanide-bridged one-dimensional $\{Fe^{III}_2Fe^{II}\}_n$ double-zigzag chain, and exhibits thermal and photo-induced spin transition behavior in the Fe(II) sites. Whereas the other compound $[Fe(Tp)(CN)_3]_2Fe(btb)_2\cdot 2H_2O$ features cyanide-bridged trinuclear linear $Fe^{III}_2Fe^{II}$ motifs further linked by btb forming an extended linear chain, and shows weak antiferromagnetic interactions between metal centers. These results suggest that flexible ligands are sensitive to synthesis conditions and can be used to produce variable structures and magnetic properties. Although CTCS behavior has not been observed, the proposal for doing further work was provided, namely the ligand field strength and redox potential for the metal center should be carefully balanced via using ligand with moderate π-acceptor ability.

Scheme 1.2. Spin transition in Fe(II) site of a cyanide-bridged $\{Fe^{III}_2Fe^{II}\}_n$ double-zigzag chain.

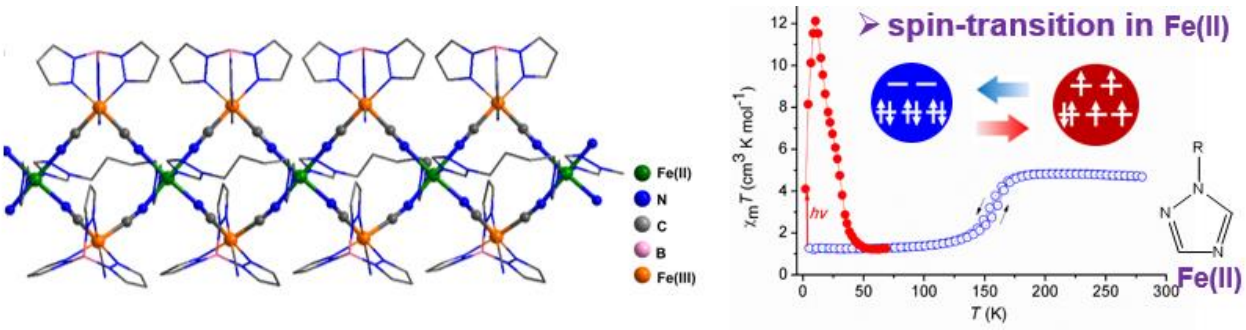

In **chapter 4**, Water-tunable thermal hysteresis in a valence tautomeric dinuclear cobalt complex $[\{Co(tpa)_2\}(dhbq)](PF_6)_3$ (tpa = tris(2-pyridylmethyl)amine, dhbq = deprotonated 2,5-dihydroxy-1,4-benzoquinone) are introduced. Two polymorphs of complex $[\{Co(tpa)_2\}(dhbq)](PF_6)_3$ were obtained via controlling the recrystallization temperature. Importantly, the two polymorphs display very distinct magnetic behaviors, thus provide a good opportunity for the investigation on the "pure" contribution of intermolecular factors to the valence tautomeric behaviors. The polymorph with the $[\{Co(tpa)_2\}(dhbq)]$ cations arranged *head-to-tail* characterizes relatively strong π···π interactions, and thus shows an abrupt and complete thermal valence tautomeric transition with adjustable hysteresis loop at around room temperature. Whereas, the polymorph featuring valence tautomeric

cations arranged *head-to-waist* with their neighbors exhibits weak π···π interactions, thus lead to a gradual and incomplete thermal valence tautomeric transition. The valence tautomeric transition process for both polymorphs can be induced by light, but the light-excited states for them show distinct thermal relaxation behaviors.

Scheme 1.3. Polymorphic structures a valence tautomeric dinuclear cobalt complex, one of polymorph exhibits water tunable thermal hysteresis.

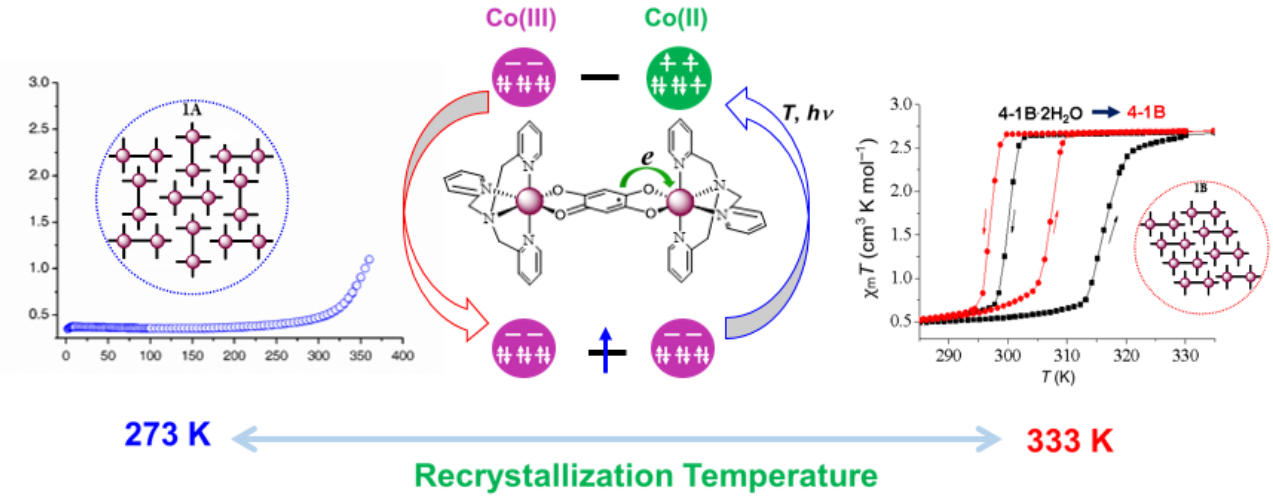

References

(1) R. L. Carlin, *Magnetochemistry*, Springer-Verlag, New York, **1986**.

(2) O. Kahn, *Molecular Magnetism*, VCH, New York, **1993**.

(3) R. L. Carlin, A. J. van Duyneveldt, *Magnetic Properties of Transition Metal Compounds,* Springer-Verlag, New York, **1977**.

(4) J. S. Miller, M. Drillon, *Magnetism: Molecules to Materials*, Wiley-VCH, Weinhein, New York, **2001**.

(5) D. Gatteschi, R. Sessoli, R. J. Villain, *Molecular Nanomagnets*, Oxford University Press, Oxford, **2006**.

(6) J. Bartolomé, F. Luis, J. F. Fernández, *Molecular Magnets*, Springer-Verlag, New York Dordrecht London, **2014**.

(7) J. P. Launay, M. Verdaguer, *Electrons in Molecules*. Oxford University Press, Oxford, **2014**.

(8) S. Decurtins, R. Pellaux, G. Antorrena, F. Palacio, *Coord. Chem. Rev.* **1999**, *190–192*, 841–854.

(9) P. Gütlich, H. A. Goodwin, *Spin Crossover in Transition Metal Compounds*, Springer-Verlag, New York, **2004**.

(10) M. A. Halcrow, *Spin-Crossover Materials*. John Wiley & Sons, United Kingdom, **2013**.

(11) L. Ouahab, *Multifunctional Molecular materials*, Pan Stanford, Singapore, **2013**.

(12) R. Sessoli, D. Gatteschi, A. Caneschi, M. A. Novak, *Nature* **1993**, *365*, 141–143.

(13) D. Gatteschi, R. Sessoli, *Angew. Chem. Int. Ed.* **2003**, *42*, 268–297.

(14) R. E. P. Winpenny, *Angew. Chem. Int. Ed.* **2008**, *47*, 7992–7994.

(15) L. Bogani, W. Wernsdorfer, *Nat. Mater.* **2009**, *7*, 179–186.

(16) G. A. Craig, M. Murrie, *Chem. Soc. Rev.* **2015**,*44*,2135–21347.

(17) J. M. Frost, K. L. Harriman, M. Murugesu, *Chem. Sci.* **2016**, *7*, 2470–2491.

(18) C. Benelli, D. Gatteschi, *Introduction to Molecular Magnetism*, Wiley-VCH: Weinheim, Germany, **2015**.

(19) J. M. Zadrazny, M. Atansov, A. M. Bryan, C.-Y. Lin, B. D. Rekken, P. P. Power, F. Neese, J. R. Long, *Chem. Sci.* **2013**, *4*, 125–138.

(20) R. Sessoli, H. L. Tsai, A. R. Schake, S. Wang, J. B. Vincent, K. Folting, D. Gatteschi, G. Christou, D. N. Hendrickson, *J. Am. Chem. Soc.* **1993**, *115*, 1084–1816.

(21) R. Bagai, G. Christou, *Chem. Soc. Rev.* **2009**, *38*,1011–1026.

(22) M. Murrie, *Chem. Soc. Rev.* **2010**,*39*,1986–1995.

(23) J. H. Atkinson, A. D. Fournet, L. Bhaskaran, Y. Myasoedov, E. Zeldov, E. del Barco, S. Hill, G. Christou, J. R. Friedman, *Phys. Rev. B* **2017**, 184403.

(24) J. Espín, R. Zarzuela, N. Statuto, J. Juanhuix, D. Maspoch, I. Imaz, E. Chudnovsky, J.Tejada, *J. Am. Chem. Soc.* **2016**, *138*, 9065–9068.

(25) L. Bogani, W. Wernsdorfer, *Nat. Chem.* **2008**, *7*, 179 –186.

(26) S. Moggach, Parsons, S. P. Perlepes, G. Christou, E. Brechin, *J. Am. Chem. Soc.* **2007**, *129*, 2754–2755.

(27) O. Waldamann, *Inorg. Chem.* **2007**, *46*, 10035–10037.

(28) F. Nees, D. A. Pantazis, *Faraday Disscuss.* **2011**, *148*, 229–238.

(29) N. Ishikawa, M. Sugita, T. Ishikawa, S. Koshihara, Y. Kaizu, *J. Am. Chem. Soc.* **2003**, *125*, 8694–8695.

(30) L. Sorace, C. Benelli, D. Gatteschi, *Chem. Soc. Rev.* **2011**, *40*,3092–3104.

(31) P. Zhang, Y.-N. Guo, J.-K. Tang, *Coord. Chem. Rev.* **2013**, *257*, 1728–1763.

(32) D. N. Woodruff, R.E.P. Winpenny, R. A. Layfield, *Chem. Rev.* **2013**, *113*, 5110–5148.

(33) P. Zhang, L. Zhang, C. Wang, S.-F. Xue, S.-Y. Lin, J.-K. Tang, *J. Am. Chem. Soc.* **2014**, *136*, 4484–4487.

(34) J. Liu, Y.-C. Chen, J.-L. Liu, V. Vieru, L. Ungur, J.-H. Jia, L. F. Chibotaru, Y Lan, W. Wernsdorfer, S. Gao, X.-M. Chen, M.-L. Tong, *J. Am. Chem. Soc.* **2016**, *138*, 5441–5450.

(35) Y.-S. Ding, N. F. Chilton, R. E. P. Winpenny, Y.-Z. Zheng, *Angew. Chem. Int. Ed.* **2016**, *55*,

16071–16074.

(36) D. E. Freedman, W. H. Harman, T. D. Harris, G. J. Long,C. J. Chang, J. R. Long, *J. Am. Chem. Soc.* **2010**, *132*, 1224–1225.

(37) J. M. Zadrozny, D. J. Xiao, M. Atanasov, G. J. Long, F. Grandjean, F. Neese, J. R. Long, *Nat. Chem.* **2013**, *5*, 577–581.

(38) A. K. Bar, C. Pichon, J.-P. Sutter, *Coord. Chem. Rev.* **2016**, 308, 346–380.

(39) M. Ding, G. E. Cutsail III, D. Aravena, M. Amoza, M. Rouzières, P. Dechambenoit, Y. Losovyj, M. Pink, E Ruiz, R. Clérac, J. M. Smith, *Chem. Sci.* **2016**, *7*, 6132–6140.

(40) Y. Rechkemmer, F. D. Breitgoff, M. V. D. Meer, M. Atanasov, M. Hakl, M. Orlita, P. Neugebaure, F. Neese, B. Sarkar, J. van Slageren, *Nat. Commun.* **2015**, *7*, 10467.

(41) F. Shao, B. Cahier, N. Guihéry, E. Rivière, R. Guillot, A.-L. Barra, Y. Lan, W. Wernsdorfer, V. E. Campbell, T. Mallah, *Chem. Commun.* **2015**, *51*, 16475–16478.

(42) W. Lin, T. Bodenstein, V. Mereacre, K. Fink, A. Eichhöfer, *Inorg. Chem.* **2016**, 55, 2091–2100.

(43) J. Miklovič , D. Valigura , R. Boča, J. Titiš, *Dalton Trans.* **2015**, *44*, 12484–12487.

(44) Y.-F. Deng, T. Han, Z. Wang, Z. Ouyang, B. Yin, Z. Zheng, J. Krzystek, Y.-Z. Zheng, *Chem. Commun. 2015*, *51*, 17688–17691.

(45) X. Feng, C. Mathonière, I.-R. Jeon, M. Rouzières, A. Ozarowski, M. L. Aubrey, M. I. Gonzalez, R. Clérac, J. R. Long, *J. Am. Chem. Soc.* **2013**, *135*, 15880–15884.

(46) A. Urtizberea, O. Roubeau, *Chem. Sci.* **2017**, *8*, 2290–2295.

(47) F. Donati, S. Rusponi, S. Stepanow, C. *et al.*, Science **2016**, *352*, 318–321.

(48) F. D. Natterer, K. Yang, W. Paul, P. Willke, T. Choi, T. Greber, A. J. Heinrich, C. P. Lutz, *Nature* **2017**, 226–228.

(49) R. Glauber, J. math. Phy. 1963, 4, 294–307.

(50) A. Caneschi, D. Gatteschi, N. Lalioti, C. Sangregorio, R. Sessoli, G. Venturi, A. Vindigni, A. Rettori, M. G. Pini, M. A. Novak, *Angew. Chem. Int. Ed.* **2001**, *40*, 1760–1763.

(51) W.-X. Zhang, R. Ishikawa, B. Breedlove, M. Yamashita, *RSC Adv.* 2013, *3*, 3772–3798.

(52) R.-M. Wei, F. Cao, J. Li, L. Yang, Y. Han, X.-L. zhang, Z. Zhang, X.-Y. Wang, Y. Song, *Sci. Rep.* **2016**, *6*, 24372.

(53) O. Kahn, C. J. Martinez, *Science* **1998**, *279*, 44–48.

(54) A. Bousseksou, G. Molnár, P. Demont, J. Menegotto, *J. Mater. Chem.* **2003**, *13*, 2069–2071.

(55) A. Calzolari, Y. Chen, G. F. Lewis, D.B. Dougherty, D. Shultz, M. B. Nardelli, *J. Phys. Chem. B* **2012**, *116*, 13141–13148.

(56) O. Sato, J. Tao, Y.-Z. Zhang, *Angew. Chem. Int. Ed.* **2007**, *46*, 2152–2187.

(57) O. Sato, *Nat. Chem.* **2016**, *8*, 644–656.

(58) E. Evangelio, D. Ruiz-Molina, *Eur. J. Inorg. Chem.* **2005**, *118*, 2957–2971.

(59) M. Marchivie, P. Guionneau, J. A. K. Howard, G. Chastanet, J.-F. LXtard, A. E. Goeta, D. Chasseau, *J. Am. Chem. Soc.* **2002**, *124*, 194– 195.

(60) T. Tayagaki, K. Tanaka, *Phys. Rev. Lett.* **2001**, *86*, 2886–2889.

(61) S. Brooker, *Chem. Soc. Rev.***2015**, *44*, 2880–2892.

(62) J. Tao, R.-J. Wei, R.-B. Huang, L.-S. Zheng, *Chem. Soc. Rev.* **2012**, *41*, 703–737.

(63) B. Weber, W. Bauer, J. Obel, *Angew. Chem. Int. Ed.* **2008**, *47*, 10098–10101.

(64) M. A. Halcrow, *Chem. Lett.* **2014**, *43*, 1178–1188.

(65) C. Lochenie, W. Bauer, A. P. Railliet, S. Schlamp, Y. Garcia, B. Weber, *Inorg. Chem.* **2014**, *53*, 11563–11572.

(66) E. Tailleur, M. Marchivie, N. Daro, G. Chastanet, P. Guionneau, *Chem. Commun.* **2017**, *53*, 4763–4766.

(67) E. Coronado, J. R. Galán-Mascarós, M. Monrabal-Capilla, J. García-Martínez, P. Pardo-Ibáñez, *Adv. Mater.* **2007**, *19*, 1359–1361.

(68) S. Hayami, Z.-Z. Gu, H. Yoshiki, A. Fujishima , O. Sato, *J. Am. Chem. Soc.* **2001**, *123*, 11644–11650.

(69) T. Buchen, P. Gütlich, K. H. Sugiyarto, H. A. Goodwin, *Chem. – Eur. J.* **1996**, *9*, 1134–1138.

(70) S. Hayami, K. Kato, Y. Komatsu, A. Fuyuhiro, M. Ohba, *Dalton Trans.* **2011**, *40*, 2167–2169.

(71) R.G. Miller, S. Narayanaswamy, J. L. Tallon, S. Brooker, *New J. Chem.* **2014***,38,* 1932-1941.

(72) R. Kulmaczewski, J. Olguín, J. A. Kitchen, H. L. C. Feltham, G. N. L. Jameson, J. L. Tallon, S. Brooker, *J. Am. Chem. Soc.* **2014**, *136*, 878–881.

(73) A. Atitoaie, R. Tanasa, C. Enachescu, *J. Magn. Magn. Mater.* **2012**, *324*, 1596–1600.

(74) H. J., Shepherd, *Nat. Commun.* **2013**, *4*, 2607.

(75) H. Phan, S. M., Benjamin, E. Steven, J. S. Brooks, M. Shatruk, *Angew. Chem. Int. Ed.* **2015**, *54*, 823–827.

(76) K. Takahashi, H.-B. Cui, Y. Okano, H. Kobayashi, H. Mori, H. Tajima, Y. Einaga, O. Sato, *J. Am. Chem. Soc.* **2008**, *130*, 6688–6689.

(77) H.-Y. Wang, J.-Y. Ge, C. Hua, C.-Q. Jiao, Y. Wu, C. F. Leong, *Angew. Chem. Int. Ed.* **2017**, *54*, 5465–5470.

(78) S. I. Ohkoshi, K. Imoto, Y. Tsunobuchi, S. Takano, H. Tokoro, *Nat. Chem.* **2011**, *3*, 564–569.

(79) T. Liu, H. Zheng, S. Kang, Y. Shiota, S. Hayami, M. Mito, O. Sato, K. Yoshizawa, S. Kanegawa C. Duan, *Nat. Commun.* 2013, *4*, 2826.

(80) R. M. Buchanan, C. G. Pierpont, *J. Am. Chem. Soc.* **1980**, *102*, 4951–4957.

(81) T. Tezgerevska, K. G. Alley, C. Boskvic, *Coord. Chem. Rev.* **2014**, *268*, 23–40.

(82) A. Witt, F. W. Heinemann, S. Sproules, M. M. Khusniyarov, *Chem. Eur. J.* **2014**, *20*, 11149–11162.

(83) W.-Q. Cheng, G.-L. Li, R. Zhang, Z.-H. Ni, W.-F. Wang, O. Sato, *J. Mol. Struct.* **2015**, *1087*, 68–72.

(84) F. Novio, J. Campo, D. Ruiz-Molina, *Inorg. Chem.* **2014**, *53*, 8742–8748.

(85) X.-Y. Chen, R.-J. Wei, L.-S. Zheng, J. Tao, *Inorg. Chem.* **2014**, *53*, 13212–13219.

(86) A. Witt, F. W. Heinemann, M. M. Khusniyarov, *Chem. Sci.* **2015**, *6*, 4599–4609.

(87) M. van der Meer, Y. Rechkemmer, U. Frank, F.D. Breitgoff, S. Hohloch, C.-Y. Su, P. Neugebauer, R. Marx, R. Marx, M. Dörfel, J. van Slageren, B. Sarkar, *Chem. Eur. J.* **2016**, *22*, 13884–13893.

(88) V. I. Minkin, A. A. Starikova, A. G. Starikov, *Dalton Trans.* **2015**, *44*, 1982–1991.

(89) O.-S. Jung, D. H. Jo, Y.-A. Lee, B. J. Conklin, C. G. Pierpont, *Inorg. Chem.* **1997**, *36*, 19–24.

(90) R. D. Schmidt, D. A. Shultz, J. D. Martin, P. D. Boyle, *J. Am. Chem. Soc.* **2010**, *132*, 6261–6273.

(91) J. Tao, H. Maruyama, O. Sato, *J. Am. Chem. Soc.* **2006**, *128*, 1790–1791.

(92) O. Cador, A. Dei, C. Sangregorio, *Chem. Commun.* **2004**, 652–653.

(93) D. M. Adams, D. N. Hendrickson, *J. Am. Chem. Soc.* **1996**, *118*, 11515–11528.

(94) P. L. Gentili, L. Bussotti, R. Righini, A. Beni, L. Bogani, A. Dei, *Chem. Phys.* **2005**, *314*, 9–17.

(95) C. Carbonera, A. Dei, J.-F. Létard, C. Sangregoria, L. Sorace, *Angew. Chem. Int. Ed.* **2004**, *43,* 3136–3138.

(96) P. Dapport, A. Dei, G. Poneti, L. Sorace, *Chem. – Eur. J.* **2008**, *14*, 10915–10918.

(97) O. Sato, S. Hayami, Z.-Z. Gu, K. Takahashi, R. Nakajima, K. Seki, A. Fujishima, *J. Photochem. Photobiol. A* **2002**, *149*, 111–114.

(98) O.-S. Jung, C. G. Pierpont, *J. Am. Chem. Soc.* **1994**, *116*, 2 2 2 9–2230.

(99) C. G. Pierpont, Proc. *Indiana Acad. Sci.* **2002**, *114*, 247–254.

(100) O. Sato, T. Tyoda, T. Fujishima, K. Hashimoto, *Science*, **1996**, *272*, 704–705.

(101) C. P. Berlinguette, A. Dragulescu-Andrasi, A. Sieber, J. R. Galán-Mascarós,| H.-U. Güdel, C. Achim, K. R. Dunbar, *J. Am. Chem. Soc.* **2004**, *126*, 6222–6223.

(102) C. P. Berlinguette, A. Dragulescu-Andrasi, A. Sieber, H.-U. Güdel, C. Achim, K. R. Dunbar, *J. Am. Chem. Soc.* **2005**, *127,* 6766–6779.

(103) D. Li, R. Clérac, O. Roubeau, E. Harté, C. Mathonière, R. L. Bris,| S. M. Holmes, *J. Am. Chem. Soc.* **2008**, *130,* 252–258.

(104) N. Hoshino, F. Iijima, G. N. Newton, N. Yoshida, T. Shiga, H. Nojiri, A.Nakao, R. Kumai,

Y. Murakami H. Oshio. *Nat. Chem.* **2012**, *4*, 921–926.

(105) X.-Y. Wang, C. Avendaño, K. R. Dunbar, *Chem. Soc. Rev.* **2011**, *40*, 3213–3238.

(106) S. Ohkoshi, S. Ikeda, T. Hozumi, T. Kashiwagi, K. Hashimoto, *J. Am. Chem. Soc.* **2006**, *128*, 5320–5321.

(107) C. Zheng, J. Xu, Z. Yang, J. Tao, D. Li. *Inorg. Chem.,* **2015**, *54*, 9687-9689.

(108) D. Garnier, R.Jiménez, Y.Li, J. von Bardeleben, Y.Journaux, T. Augenstein, E. Moos, M. T. Gamer, F. Breher, R. Lescouëzec. *Chem. Sci.* **2016**, 4825–4831.

(109) Y. Zhang, D. Li, R. Clérac, M. Kalisz, C. Mathonière, S. M. Holmes. *Angew. Chem. Int. Ed.* **2010**, *49*, 3752–3756.

(110) Y.- Z. Zhang, P. Ferko, D. Siretanu, R. Ababei, N. P. Rath, M. J. Shaw, R. Clérac, C. Mathonière, S. M. Holmes. *J. Am. Chem. Soc.* **2014**, *136*, 16854–16864.

(111) M. Nihei, Y. Sekine, N. Suganami, K. Nakazawa, A. Nakao, H. Nakao, Y. Murakami, H. Oshio. *J. Am. Chem. Soc.* **2011***, 133*, 3592–3600.

(112) E. S. Koumousi, I. R. Jeon, Q. Gao, P. Dechambenoit, D. N. Woodruff, P. Merzeau. *J. Am. Chem. Soc.* **2014**, *136*, 15461–15464.

(113) N. Masayuki, O. Yuki, S. Yoshihiro, H. Norihisa, S. Takuya, I. P. -C. Liu, H. Oshio. *Angew. Chem. Int. Ed.* **2012**, *51*, 6361–6364.

(114) T. Liu, D.- P. Dong, S. Kanegawa, S. Kang, O. Sato, Y. Shiota, K. Yoshizawa, S. Hayami, S. Wu, C. He, and C. Y. Duan. *Angew. Chem. Int. Ed.* **2012**, *51*, 4367–4370.

(115) A. Mondal, Y. Li, M. Seuleiman, M. Julve, L. Toupet, C. M. Buron-Le, R. Lescouëzec. *J. Am. Chem. Soc.* **2013**, *135*, 1653–1656.

(116) D. Siretanu, D. Li, L. Buisson, D.M. Bassani, S.M. Holmes, C. Mathonière, R. Clérac. *Chem. Eur. J.* **2011**, *17*, 11704–11708.

(117) J. Mercurol, Y. Li, E. Pardo, O. Risset, M. Seuleiman, H. Rousselière, R. Lescouëzec, M. Julveb. Chem. Comm. **2010**, *46*, 8995–8997.

(118) C. Avendano, M. G. Hilfiger, A. Prosvirin, C. Sanders, D. Stepien, K. R. Dunbar, *J. Am. Chem. Soc.* **2010**, *132*, 13123–13125.

(119) R. Podgajny, S. Chorazy, W. Nitek, M. Rams, A. M. Majcher, B. Marszalek, J. Zukrowski, C. Kapusta, B. Sieklucka, *Angew. Chem. Int. Ed.* **2013**, *52*, 896–900.

(120) S. I. Ohkoshi, T. Matsuda, H. Tokoro, K. Hashimoto, *Chem. Mater.* **2005**, *17*, 81–84.

(121) T. Mahfoud, G. Molnár, S. Bonhommeau, S. Cobo, L. Salmon, P. Demont, H. Tokoro, S. I. Ohkoshi, K. Boukheddaden and A. Bousseksou, *J. Am. Chem. Soc.* **2009**, *131*, 15049–15054.

(122) I. L. Fedushkin, O. V. Maslova, A. G. Morozov, S. Dechert, S. Demeshko, F. Meyer, *Angew. Chem. Int. Ed.* **2012**, *51*, 10584–10587.

(123) J. M. Herrera, V. Marvaud, M. Verdaguer, J. Marrot, M. Kalisz and C. Mathonière, *Angew. Chem., Int. Ed.* **2004**, *43*, 5468–5471.

(124) S. Chorazy et al., *Chem. Commun.* **2014**, *50*, 3484–3487.

(125) K. Zhang, S. Kang, Z. S. Yao, K. Nakamura, T. Yamamoto, Y. Einaga, N. Azuma, Y. Miyazaki, M. Nakano, S. Kanegawa, O. Sato, *Angew. Chem., Int. Ed.* **2015**, *55*, 6047–6050.

Chapter 2. Field-Induced Slow Spin Direction Transition in an Octa-Coordinated Fe(II) Complex

2. 1 Introduction

Single-molecule magnets (SMMs), which exhibit slow magnetization dynamics, have enduring appeal to researchers motivated to exploit high-density memory devices, quantum computation, and molecular spintronics.[1-4] Prior efforts in this field were focused on polynuclear SMMs with high ground spin states for the purpose of increasing the magnetization reversal barrier.[5-8] Over the last decade, research interests in SMMs have largely shifted to mononuclear SMMs (single-ion magnets, SIMs) since mononuclear compounds can exhibit stronger magnetic anisotropy, which is another important factor determining the reversal energy barrier. It is well known that strong magnetic anisotropy originating from large orbital contribution of the lanthanide ions results in numerous of excellent SIMs.[9-18]

In contrast, for 3d transition-metal ions, the orbital angular momentum required for generating magnetic anisotropy is usually quenched by the large ligand-field splitting energy. The prevalent strategy in the search for 3d transition-metal ion-based SIMs is decreasing the coordination number to reduce the quenching effect. This strategy started with the discovery of SMM behavior in a trigonal pyramidal high-spin Fe(II) complex, as reported by Long et al.[19] Later the same group achieved the remarkable record of a magnetization reversal energy barrier of −226 cm^{-1} in a linear two-coordinated Fe(I) compound.[20] After that, many mononuclear complexes based on transition-metal ions, including Fe(I, II, III), Co(II), Mn(III, IV), Ni(I, II), and Cr(I, II), with coordination numbers ranging from two to five exhibiting SMM behaviors have been reported.[21-28] Another recent method to improve the magnetic anisotropy of transition metal ion is using heavy metal ions as “ligands”.[29]

In general, transition-metal complexes with unsaturated coordination surroundings are far from

stable in air. Questing SIMs in high-coordinated transition-metal complexes can not only afford some air-stable SIMs, but also can provide some significant information about the intrinsic nature of the materials. Very recently, SIM behaviors have also been observed in some Co(II) compounds with higher-coordinated environments, including in hexa-,[30-40] hepta-,[41, 42] and octa-coordinated complexes[43]. Achieving SIM behaviors in Co(II) compounds are relatively easy since Co(II) is a type of Kramers ion (the ion possesses half-integer spin, for which all energy level is doubly degenerate). In contrast, achieving SIM behaviors in high-coordinated mononuclear compounds based on non-Kramers ions, such as Fe(II), remains a challenge. To date, there are still limited examples of high-coordinated mononuclear SMMs based on Fe(II) or other transition-metal non-Kramers ions.[44-48]

As we know, magnetic anisotropy is deeply influenced by molecular symmetry, which provides a means for achieving SIM behaviors in high-coordinated mononuclear complexes containing non-Kramers ions. We found that the transverse zero-field splitting (ZFS) parameter, *E*, can be limited in a very small value if the metal complex has a three- or four-fold symmetric axis, which may favor the compound to exhibit SIM behavior. This deduction is supported by a six-coordinated Fe(II) complex, $[FeII(ptz)_6](BF4)_2$ (ptz = 1-propyltetrazole), which exhibits photo-switchable SIM behaviors.[44] $[FeII(ptz)_6](BF_4)_2$ shows thermal- and photo-induced spin transition behaviors, and possesses two low-spin state forms (**LS$_\alpha$** and **LS$_\beta$**) determined by the rate of lowering the temperature. **LS$_\alpha$** has C_i symmetry and **LS$_\beta$** possesses higher symmetry (D_{3d}). SIM behavior can only be achieved for the light-excited state of **LS$_\beta$**. Photo-switchable SIM behavior is also observed for a similar Fe(II) compound $[FeII(mtz)_6](CF_3SO_3)_2$ (mtz = 1-methyltetrazole).[45] $[Fe^{II}(mtz)_6](CF_3SO_3)_2$ shows thermal-induced incomplete spin transition, and the high-spin Fe(II) sites at low temperature features D_{3d} symmetry. Hence, the low temperature phase of $[Fe^{II}(mtz)_6](CF_3SO_3)_2$ exhibits field-induced SIM behavior, and the SIM behavior can be switched off and on via the red and green light.

Generally, mononuclear complexes characterizing D_{2d} symmetry are more common in high-coordinated complexes, and these compounds also have a very small *E* value, which may represent

another family of candidates for SIMs. Herein, we present an octa-coordinated Fe(II) complex, $[Fe^{II}(dpphen)_2](BF_4)_2 \cdot 1.3H_2O$ (**2-1**, dpphen = 2,9-di(pyrazo-1-yl)-1,10-phenanthroline), which possesses an approximate D_{2d} symmetric metal center. Magnetic measurement, high-frequency/field electron paramagnetic resonance (HF-EPR) studies, and theoretical calculations reveal that this Fe(II) complex features uniaxial magnetic anisotropy, and exhibits field-induced slow magnetic relaxation in low temperature. We select dpphen as the coordination ligand based on the following considerations (Scheme 1): a) the terminal groups (pyrazole, pz) located at the 2,9- positions of the rigid phenanthroline (phen) can weaken their ligand field on the metal center; b) the relatively large steric effect of dpphen can prevent the molecular geometry from seriously deviating from D_{2d} symmetry. Finally, the correlation of magnetic properties and structure is carefully discussed based on **2-1** and a very recently reported 8-coordinated Fe(II) complex $[Fe^{II}(L)_2](ClO_4)_2$ (L = 2,9-bis(carbomethoxy)-1,10-phenanthroline),[48] which provides a possible strategy to improve the magnetic properties for this type of Fe(II) SIMs.

Scheme 2.1. Synthesis of 2,9-di(pyrazo-1-yl)-1,10-phenanthroline (dpphen) and complex **2-1**.

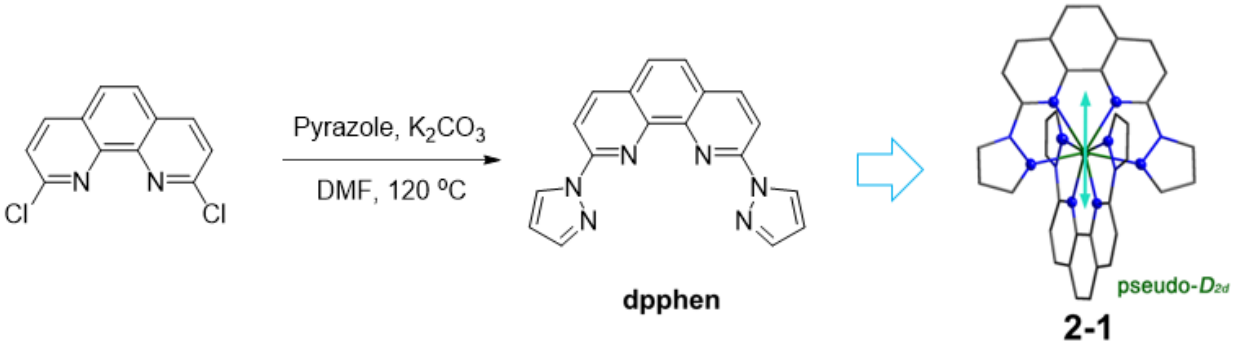

2. 2 Experimental Section

2.2.1 Starting Materials and Synthesis Methods

2,9-dichrolo-phenanthroline (Sigma-Aldrich), (pyrazole (TCI), $Fe^{II}(BF_4)2 \cdot 6H_2O$ (Sigma-Aldrich), K_2CO_3 (Wako) and all the solvents (Wako, reagent grade) were used as received.

Synthesis of dpphen (Scheme 2.1). 2,9-dichrolo-phenanthroline (0.50 g, 2.00 mmol), pyrazole (0.32 g, 4.80 mol) and K_2CO_3 (0.66 g, 4.80 mmol) were mixed in 10 ml DMF, and the mixture was kept at 120 °C for 3 days. The resulting mixture was slowly cooled to room temperature and then poured into 20 ml cold water. The target ligand, dpphen, was obtained as white solid which was collected by filtration, washed with cold water several times, and dried in air. Yield: 0.56 g, 89%. ^{1}H NMR (600 MHz, 25 °C, $CDCl_3$) δ: 9.10 (*d*, *J* = 2.4 Hz, 2H), 8.40 (*dd*, *J* = 20.4 Hz, 8.6 Hz, 4H), 7.84 (*d*, *J* = 0.8 Hz, 2H), 7.80 (*s*, 2H), 6.59–6.62 (m, 4H).

Synthesis of $[Fe^{II}(dpphen)_2](BF_4)_2 \cdot 1.3H_2O$ (2-1). $Fe^{II}(BF_4)_2 \cdot 6H_2O$ (16.85 mg, 0.05 mmol) in methanol (10 ml) was added to a suspension of dpphen (31.20 mg, 0.10 mmol) in acetonitrile (5 ml). The resulting orange-red solution was placed under ambient conditions without disturbance. Orange-black crystals can be obtained by evaporation of the solvent within one week. Yield: 67%. Anal. calcd for $C_{36}H_{26.6}N_{12}O_{1.3}FeB_2F_8$ (F.W. = 878.01 g mol^{-1}): C, 3.06; H, 49.27; N, 19.15. Found: C, 3.03; H, 49.37; N, 19.19.

2.2.2 Physical Measurement

Crystallographic data collection and structure refinement. Single-crystal X-ray data for compound **2-1** were collected on an FR-E + CCD diffractometer with Mo-Kα radiation at 123 K. The structure of complex **2-1** was solved using a direct method and refined with the full-matrix least-squares technique using the SHELXTL 2014 program[49]. All the non-hydrogen atoms were anisotropically refined, and all the hydrogen atoms were located by the HFIX command in the SHELXTL program. The conditions for X-ray data collection and structure refinement are available in Table 1. The coordination bond lengths and some significant geometrical parameters are presented in Table 2. Structural information of **2-1** (1528305) can be obtained freely from the Cambridge Crystallographic Data Centre (CCDC) or at www.ccdc.cam.ac.uk/conts/retrieving.html.

Other Physical measurements. Direct current (dc) and alternating current (ac) magnetic susceptibilities were collected on a Quantum Design MPMS-5S SQUID magnetometer using a crushed crystal sample which was fixed by eicosane. HF-EPR measurement was performed on a locally developed spectrometer at Wuhan National High-magnetic Field Center with a pulsed magnetic field of up to 30 T. Elemental analysis was carried out on a Yanaco CHN CORDER MT-6 elemental analyzer. NMR data were collected on a Bruker AVANCEIII 600 NMR spectrometer.

Computational details. Geometric optimization of complex **2-1** was performed with the Gaussian09 package [50] using the density functional theory (DFT) method. The coordinates of all the hydrogen atoms were optimized, and the coordinates of the other atoms were frozen to the X-ray determined structure. BP86 functional and TZVP basis was used in the optimization.[51-54] The ground- and excited-state energies as well as the wave functions for complex **2-1** were obtained from *ab initio* calculations. The calculations were performed using ORCA package (version 3.0.3), in which the Complete-Active-Space Self-Consistent-Field (CASSCF) module for static correlation, and the N-Electron Valence Perturbation Theory (NEVPT2) for dynamic correlation were used.[55] For simplicity, the active space only included the six electrons on the 3d orbitals of the Fe center. Five $S = 2$ and thirty $S = 1$ states were taken into consideration. Basis sets of TZVP quality together with the auxiliary sets (TZVP/C) were used through all ab initio calculations.[51-54]

2. 3 Results and Discussion

2.3.1 Structural Analysis

Main Structural analysis revealed that compound **2-1** crystallized in the triclinic space group $P\bar{1}$ (Table 2.1). Shape analysis[14] indicated that the magnetic unit $[Fe^{II}(dpphen)_2]^{2+}$ features an approximate D_{2d} symmetric metal center with a snub diphenoid (J84) FeN_8 coordination geometry (Fig. 2.1). The two N_4 planes of dpphen ligands are nearly in vertical form with an inter-planar angle of 89.32 °. The Fe-N_{phen} and Fe-N_{pz} bond lengths are almost equal within the range of 2.3088(18)–

2.3823(19) Å (Table 2.2). To the best of our knowledge, there are three other Fe(II) compounds featuring FeN_8 coordination surroundings with pseudo-D_{2d} symmetry.[56, 57] Compared with these compounds, **2-1** has slightly shorter Fe–N bond lengths near the S_4 axis, but obviously longer bond lengths between Fe(II) center and the coordination atoms of terminal chemical groups. The very recently 8-coordinated Fe(II) complex with FeN_4O_4 coordination surrounding characterizes similar structure with complex **2-1**.[48]

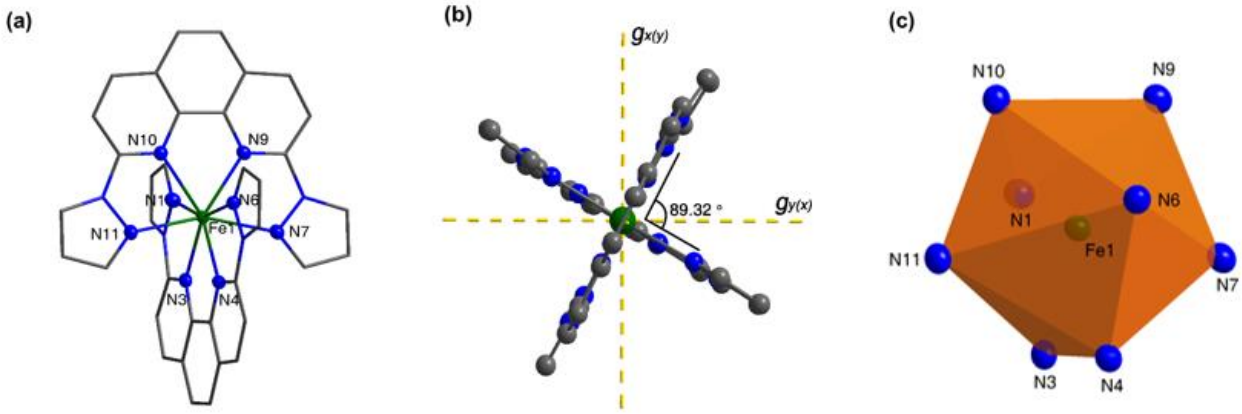

Figure 2.1. Molecular structure of $[Fe^{II}(dpphen)_2]^{2+}$ of complex **2-1** (a, view from front) and (b, view from top); (c) coordination polyhedron showing a snub diphenoid (J84) FeN_8 coordination geometry of $[Fe^{II}(dpphen)_2]^{2+}$ for complex **2-1**. (Fe, C and N atoms are represented in green, gray and blue, respectively; H atoms were omitted for clarity. The angle shown is the inter-plane angle between the two N4 planes of the two dpphen ligands; the *g*-tensors were determined by calculation.)

The crystal packing structure of compound **2-1** shows a layer-by-layer stacking $[Fe^{II}(dpphen)_2]^{2+}$ units, as viewed from the crystalline *a*-axis direction (Fig. 2.2). In the same layer, the $[Fe^{II}(dpphen)_2]^{2+}$ unit interacts with its neighbors through π···π intermolecular interactions between two pyrazole groups with the centroid···centroid distances of 3.710 Å and 3.727 Å for pyrazole pairs (Fig. 2). The adjacent Fe···Fe distances are 8.566 Å and 8.739 Å, which means no efficient intermolecular magnetic exchange pathway exists in complex **2-1**.

Table 2.1. Crystallographic parameters of complexes **2-1**.

Compound	**2-1**
Formula	$C_{36}H_{26.65}FeF_8N_{12}O_{1.33}B_2$
Formula weight	878.01
Temp. (K)	123 K
Crystal System	triclinic
Space group	$P\bar{1}$ (No. 2)
a (Å)	8.5661(17)
b (Å)	8.7388(17)
c (Å)	23.832(5) Å
α (°)	84.71(3)°
β (°)	84.21(3)
γ (°)	88.14(3)
Volume (Å^3)	1766.8(6)
Z	2
$\rho_{calcd.}$(g cm^{-3})	1.650
μ (Mo-$K\alpha$)	0.523
F(000)	890.5
θ range (°)	2.3412–30.6672
Reflections	6969
R_1 ($I > 2.0\sigma$)	0.0502
wR_2 (*all data*)	0.1268
Goodness-of-fit on F^2	1.069

[a] $R = \sum||F_0|-|F_c||)/\sum|F_0|$ [b] $wR = |\sum w(F_0-F_c)^2/\sum w(F_0^2)^2|^{1/2}$

Table 2.2. Selected bond distances (Å) and angles (°) for complex **2-1**.

Fe–N(phen)		Fe–N(pz)	
Fe1–N1	2.3454(19)	Fe1–N3	2.3396(19)
Fe1–N6	2.3265(19)	Fe1–N4	2.3218(19))
Fe1–N7	2.3130(19)	Fe1–N9	2.3088(18)
Fe1–N12	2.3823(19)	Fe1–N10	2.343(2)
Fe···Fe	8.566 / 8.739		
Inter-plane angle of dpphen(N_4)	89.32		

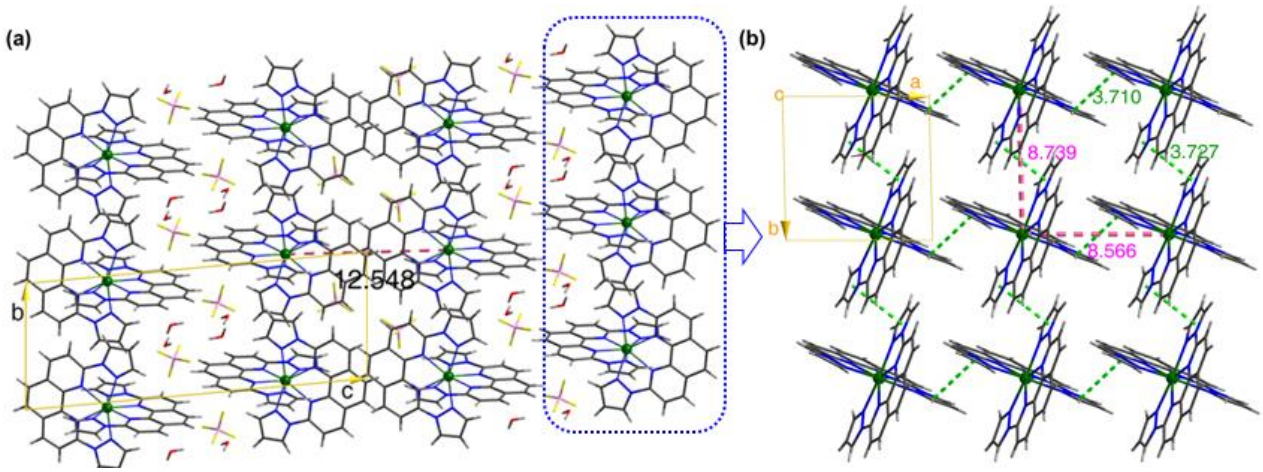

Figure 2.2. Crystal packing mode for complex **2-1** showing layer-by-layer packing of $[Fe^{II}(dpphen)_2]^{2+}$ along *a* direction (a), and one-layer packing of $[Fe^{II}(dpphen)_2]^{2+}$ with π···π interactions along the *c* direction (b), Fe, C, N, O, F, B, and H atoms are shown in green, gray, blue, red, yellow, pink, and light gray, respectively.

2.3.2 Static Magnetic Properties.

The temperature-dependent direct current (dc) magnetic susceptibility for **2-1** was obtained under an applied magnetic field of 1000 Oe (Fig. 2.3). The $\chi_m T$ value is 3.23 $cm^3\ mol^{-1}$ K at 300 K, a little larger than the spin-only value (3.00 $cm^3\ mol^{-1}$ K) for an isolated high-spin Fe(II) ion (S = 2, g = 2.0),

which is comparable with other high-spin Fe(II) compounds with pseudo-D_{2d} symmetric metal centers.[48, 56] Upon lowering the temperature, the $\chi_m T$ value remains almost constant until ca.50 K, and then gradually decreases before ca.15 K. After that, it decreases sharply until finally reaching 2.11 $cm^3\ mol^{-1}\ K$ at 2 K. The diminished $\chi_m T$ value at low temperature may be ascribed to the magnetic anisotropy of compound **2-1**, but can also be caused by intermolecular antiferromagnetic interactions at very low temperature.

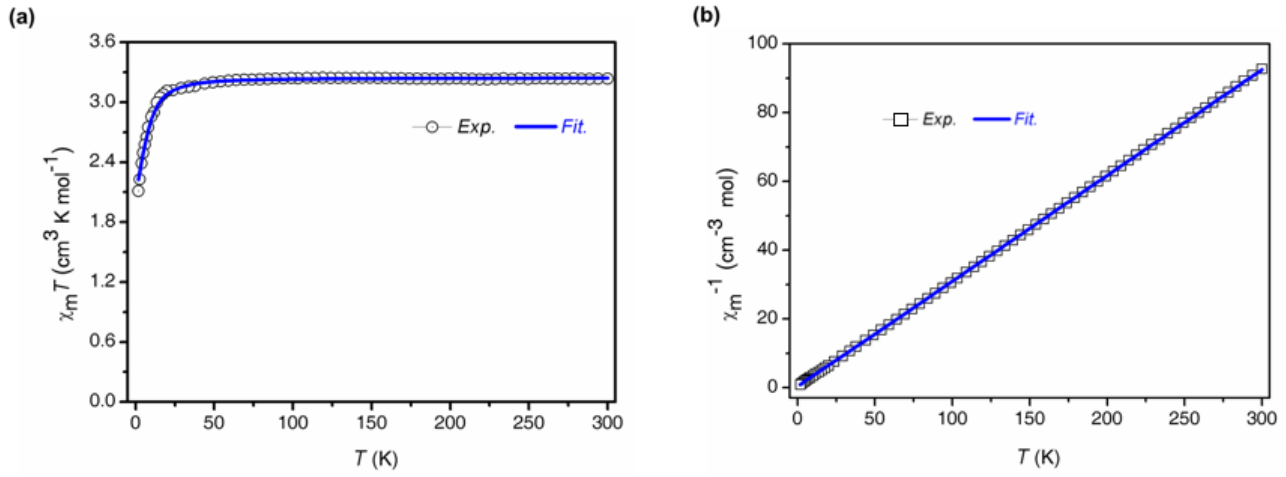

Figure 2.3. Temperature dependence of $\chi_m T$ (a) and χ_m^{-1}(b) measured under an applied field of 1000 Oe for **2-1**. The blue solid lines represent the best fits to the experimental data using the PHI program.

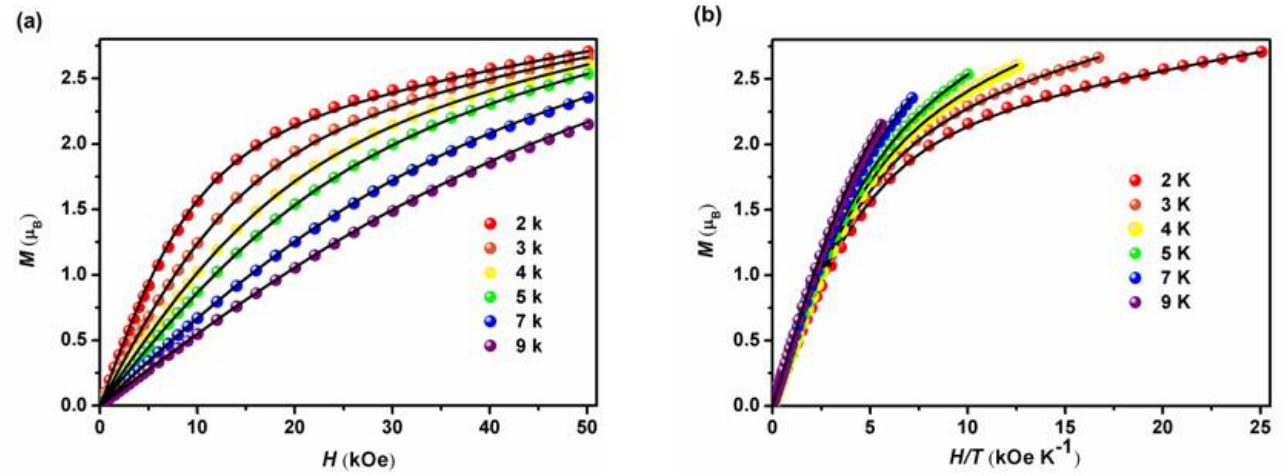

Figure 2.4. Field dependence of magnetization (a) and reduced magnetization (b) at different temperatures (2–9 K) for **2-1**. The solid lines are the best fits to the experimental data using the PHI program.

The isothermal field-dependent magnetization data for compound **2-1** were collected under an applied field of up to 5.0 T with the temperatures of 2–9 K (Fig. 2.4a). The magnetization values (2.15–2.71 Nβ) at 5 T are much smaller than the saturation value expected for a magnetic system with S = 2, revealing the existence of magnetic anisotropy in complex **2-1**. Additionally, the obvious separation of the reduced magnetization curves (M vs. H/T, inset in Fig. 2.4b) in the high-field region further confirms the presence of strong magnetic anisotropy in **2-1**. The reported octa-coordinated Fe (II) complex $[Fe^{II}(L)_2](ClO_4)_2$ exhibits very similar dc magnetic properties with complex **2-1**, but it has larger $\chi_m T$ (3.58 cm^3 mol^{-1} K at 300 K) and magnetization (3.53 Nβ at 5 T and 2 K) values, which indicates that it may possesses greater orbital contribution.[48]

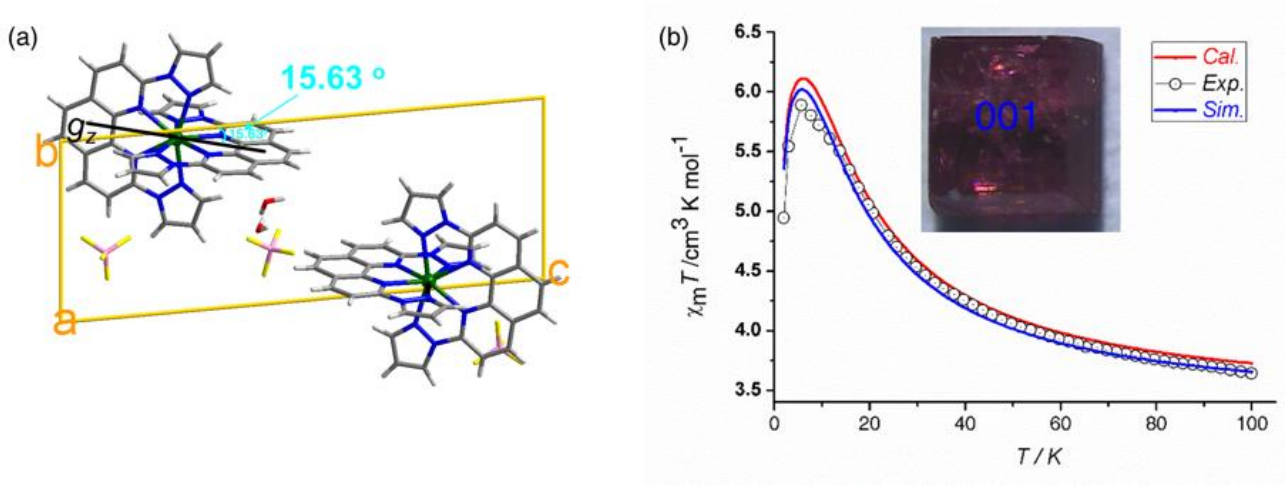

Figure 2.5. (a) Crystal packing structure of one unit cell for compound **2-1**. (b) Temperature dependence of $\chi_m T$ measured along the crystal c-axis under an applied magnetic field of 5000 Oe for **2-1**, the red solid line is the corresponding magnetic data and the blue solid line is the corresponding simulation based on spin Hamiltonian parameters derived from HF-EPR spectroscopy.

As can be seen from packing structure of compound **2-1**, $[Fe^{II}(dpphen)_2]^{2+}$ units are parallel to each other with their magnetic easy axis close to the crystal c-axis (the angle between g_z axis and c-axis is 15.63 °, Figure 2.5a). Hence, to further confirm compound **2-1** exhibiting uniaxial magnetic anisotropy, dc magnetic measurement using single crystal sample was performed along the c-axis in

the temperature range of 2–100 K (Figure 2.5b). The $\chi_m T$ value is 3.64 cm^3 mol^{-1} K at 100 K, which is obviously larger than that of powder sample at the same temperature. With temperature decreasing, the $\chi_m T$ value gradually increases to 5.89 cm^3 mol^{-1} K at 5 K, and then decreases to 4.95 cm^3 mol^{-1} K at 2 K, confirming that **1** has a magnetic easy axis near the crystal *c*-axis. More importantly, these magnetic data agree well with the magnetic data along crystal *c*-axis obtained by calculation as well as fitting data with spin Hamiltonian parameters derived from HF-EPR spectroscopy(Figure 2.5b).

In order to quantify the magnetic anisotropy, the experimental $\chi_m T$ vs. T data together with the M vs. H data were fitted with the PHI program[58] based on the anisotropic Hamiltonian expressed in the following equation (eqn. 2.1):

$$H = D\left(\hat{S}_z^2 - S(S+1)/3\right) + E\left(\hat{S}_x^2 - \hat{S}_y^2\right) + \mu_B(g_x\hat{S}_x B_x + g_y\hat{S}_y B_y + g_z\hat{S}_z B_z) \quad (2.1)$$

where D, E, S_i, B_i, and g_i stand for the uniaxial ZFS parameter, and transverse ZFS parameter, the spin operator, and the magnetic vector, and g tensor respectively, and μ_B is the Bohr magneton. The first two terms in eqn. 1 represent axial and rhombic crystal-field interactions, and the last term stands for the Zeeman effect. The best-fit parameters are $D = -5.85$ cm^{-1}, $|E| = 0.04$ cm^{-1}, $g_x = g_y = 2.04$, and $g_z = 2.16$. No admissible fitting can be achieved with a positive D. The negative signal of D and the negligible ratio of $|E/D|$ reveal that compound **2-1** features strong uniaxial magnetic anisotropy. It is worth noting that the E value approaching zero accords with the nature of a magnetic complex with a pseudo-D_{2d} symmetric metal center.

2.3.3 High-Frequency/Field Electron Paramagnetic Resonance (HF-EPR) Analysis.

Recently, HF-EPR has become a powerful technique to study the magnetic anisotropy of high-spin Fe(II) compounds.[59-62] In order to directly obtain information about the energy separation between the M_s levels, as well as to further confirm the magnetic anisotropy parameters of compound **2-1**, a variable-temperature HF-EPR at 170 GHz (Fig. 2.6) and a tunable-frequency HF-EPR at 10 K (Fig. 2.7a) experiments were carried out on a ground polycrystalline sample. As expected, complex **2-1**

generated high-quality EPR spectra with strong, well-resolved resonances in the frequency range 120–258 GHz. The field-dependent HF-EPR at 170 GHz measured at different temperature together with corresponding simulations based on a negative (lift) or a positive (right) *D* value are shown in Fig. 2.6. Upon lowering temperature, the EPR resonance at around 0.3 T becomes weaker and the signal at about 4.9 T enhances. It is clear that the simulations using a negative *D* value are in accordance with the experimental data. In contrast, the simulations based on a positive *D* value change in opposite tendency with the experimental data. This result undoubtedly indicates that this compound exhibits uniaxial magnetic anisotropy.

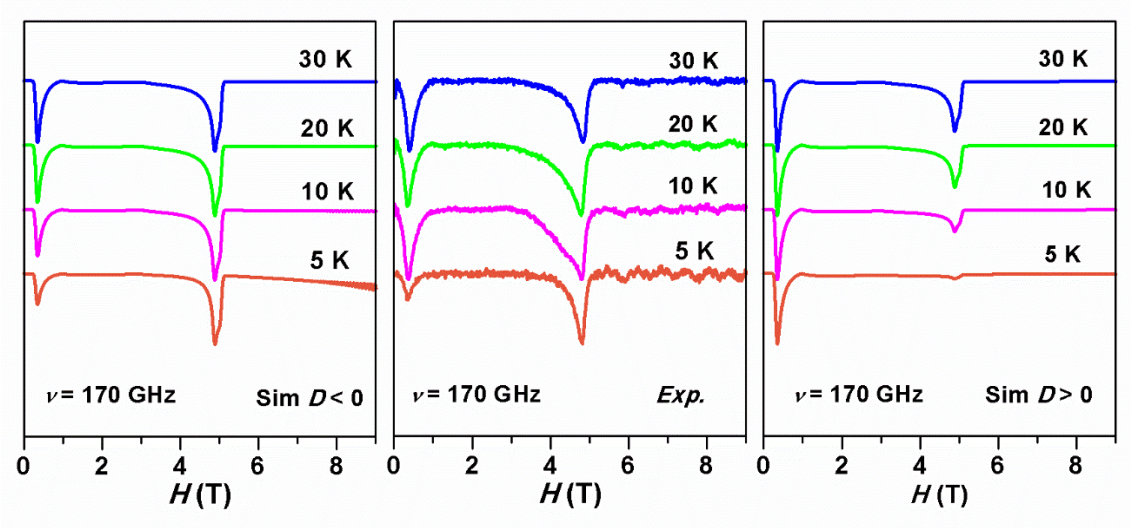

Figure 2.6. Variable-temperature of HF-EPR spectrum of **2-1** with simulated spectra at 170 GHz, which prove that the sign of zero-field splitting parameter *D* is negative for **2-1**.

To derive the magnetic anisotropy parameters from these HF-EPR spectra, the variable-frequency resonances were combined together to construct a two-dimensional map of resonant field versus frequency and transition energy, which is shown in Fig. 2.7b. A least-squares fit was carried out to the entire array of HF-EPR resonances, leading to the best-fit full-setting spin Hamiltonian parameters of D = –6.00(3) cm^{-1}, $|E|$ = 0.04(1) cm^{-1}, $g_x = g_y$ = 2.04(2) and g_z = 2.10(5). These results are in reasonable agreement with the parameters derived from the dc magnetic data. Additionally, the

simulated curves based on the above parameters agree well with the experimental points, which clearly confirms the original assignment of the observed resonances.

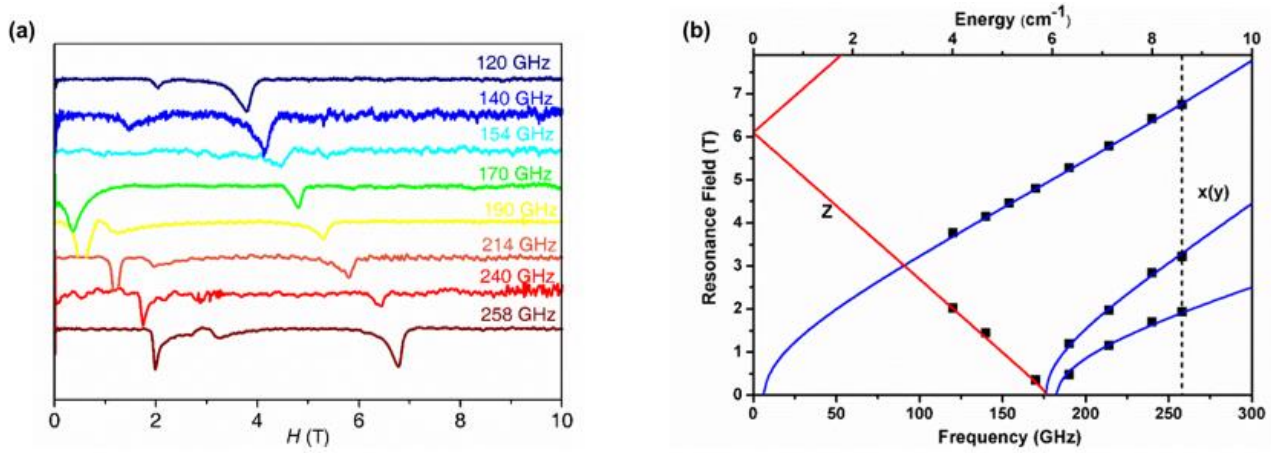

Figure 2.7. (a) HF-EPR spectra measured under various frequencies (120–258 GHz) for **2-1**; (b) Resonance field vs. microwave frequency (quantum energy) of EPR transition for **2-1**. The black squares are experimental data, while the red and blue solid lines are the best-fit to experimental data with magnetic field along z and *x* (*y*) direction, respectively.

In order to assign these particular EPR resonances, the simulated field-dependent Zeeman energy splitting plots (Fig. 2.8) for a spin quintet (S = 2) with field along *z* and *x* (*y*) directions were respectively constructed using the above spin Hamiltonian parameters in the PHI program[16]. The EPR resonances at 120 GHz and 258 GHz were representatively identified. The weak EPR resonance at 120 GHz at 2.0 T is the energy transition of $|+1\rangle \rightarrow |0\rangle$ states with the field along the *z* direction, and the resonance at 120 GHz at 3.8 T belongs to the energy transition of $|-1\rangle \rightarrow |+1\rangle$ states with the field along the *x* (*y*) direction. The EPR resonances at 2.0 T, 3.2 T, and 6.9 T at 258 GHz all originate from energy transitions between different sates with the field along the *x* (*y*) direction, which can be unambiguously identified as the energy transitions between the following sates: $|-1\rangle \rightarrow |0\rangle$, $|+1\rangle \rightarrow |0\rangle$, and $|-1\rangle \rightarrow |+1\rangle$. There is no resonance observed for *z*-components at higher

frequencies, which is due to that the *D* and the *g* factor are randomly distributed around their mean values, thus significantly broaden the EPR signals for the *z*-components at higher frequencies.[63]

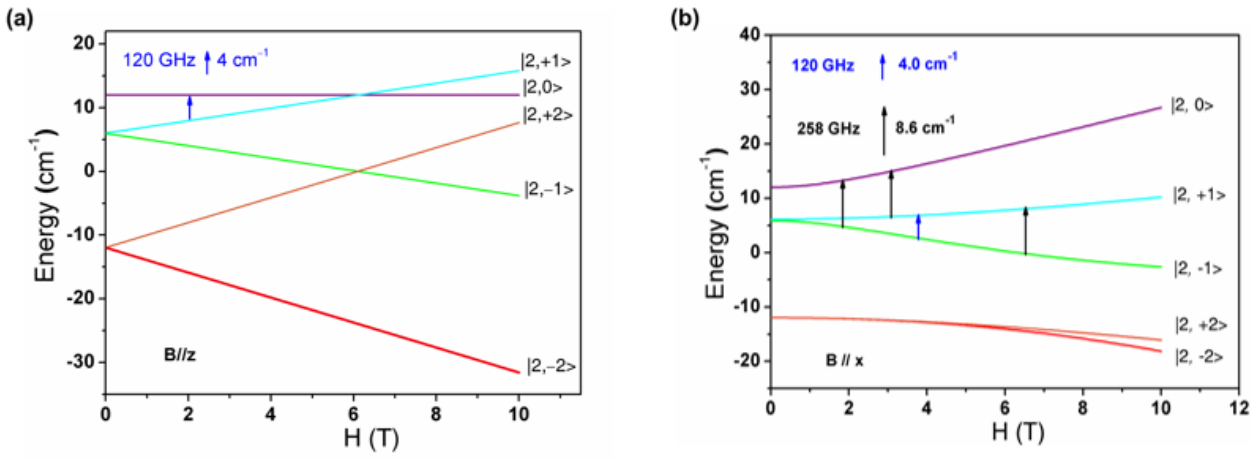

Figure 4.8. Field dependence of Zeeman energy splitting with the field along *z* (a) and *x* (b) direction, showing energy transitions between *Ms* levels corresponding to the EPR resonance at 120 GHz (blue) and 258 GHz (black) for **2-1**.

2.3.4 Dynamic Magnetic Properties

Low-temperature slow magnetic relaxation is a common property for complexes with magnetic anisotropy. To detect the dynamic magnetization behavior of compound **2-1**, its ac magnetic susceptibility was measured under zero and several non-zero external dc magnetic fields (Fig. 4.8). Under zero applied dc field, complex **2-1** exhibits very fast relaxation behavior with no detectable out-of-phase ac signal (χ_m") in the frequency range of 1–1500 Hz. This can be attributed to magnetic tunneling of the ground state, which is not uncommon for Fe(II) SIMs.[44-48] Under a 250 Oe applied dc field, a non-zero χ_m" signal with a well-resolved peak at around 165 Hz was observed. Upon increasing the external dc field, the intensity of the χ_m" signal obviously increased, accompanied by the maximum slightly shifting toward lower frequency. This variation becomes small when the external dc field is higher than 1500 Oe. It should be noted that there is a weak ac signal in the low-frequency region (1–5 Hz), indicating the existence of other relaxation processes at low temperature.

The magnetic relaxation at low frequency is likely related to the insufficient separation of the magnetic units.[64] This weak ac signal merges with the main relaxation signal when the external dc field is higher than 1000 Oe, which prevents some of the data from being fitted well. Hence, the data in the low-frequency region (1–5 Hz) were excluded in the following analyses.

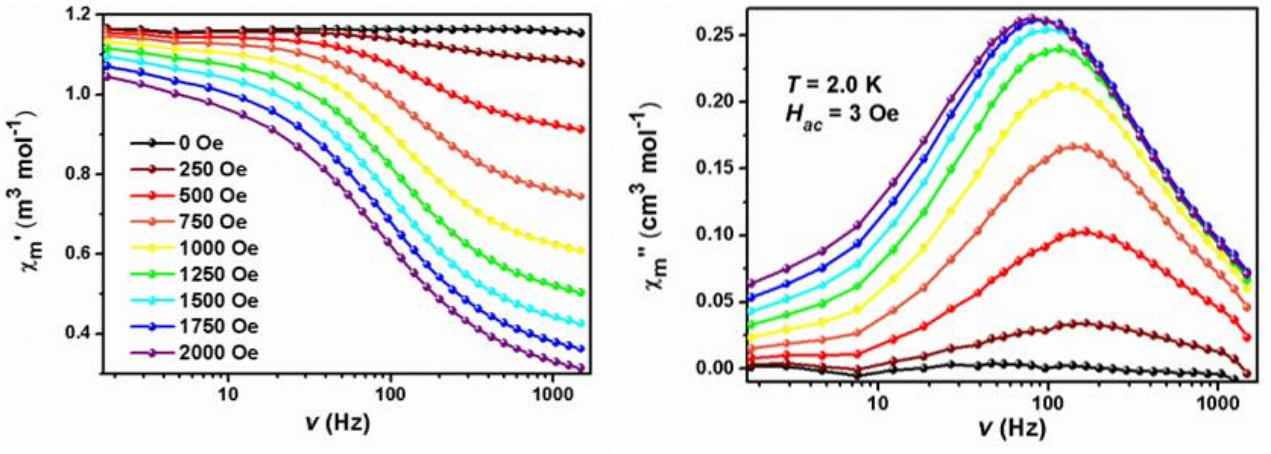

Figure 2.9. Frequency dependence of ac magnetic susceptibility measured under various applied dc fields (0–2000 Oe) at 2 K for complex **2-1**.

The dc field dependent magnetic relaxation time (τ) was determined by fitting the variable-frequency in-phase and out-of- phase ac susceptibilities (Cole–Cole plot, Fig. 4.9a) using a generalized Debye model:

$$\chi_m{}' = (\chi_t - \chi_s)\frac{((\omega\tau)^{1-\alpha}\cos(\frac{\pi\alpha}{2}))}{1+2(\omega\tau)^{1-\alpha}\sin(\frac{\pi\alpha}{2})+(\omega\tau)^{2-2\alpha}} \qquad (2.2)$$

$$\chi_m{}'' = \chi_s + (\chi_t - \chi_s)\frac{1+(\omega\tau)^{1-\alpha}\sin(\frac{\pi\alpha}{2})}{1+2(\omega\tau)^{1-\alpha}\sin(\frac{\pi\alpha}{2})+(\omega\tau)^{2-2\alpha}} \qquad (2.3)$$

where χ_s and χ_t is adiabatic and isothermal magnetic susceptibility, ω and α represents angular frequency of magnetic field variation and relaxation distribution parameter.[65] The best-fit parameters were summarized in Table 2.3, and τ versus *H* was plotted in Fig. 2.10b. The τ value monotonically increased with increasing applied dc field within the range 500–2000 Oe, which confirms the

existence of the tunneling effect at 2 K for compound **2-1**. The α values are larger than 0.2 at high applied dc fields, revealing a relatively broad distribution of relaxation times, which may be related to the fact that powder sample was used in the measurement, or the superposition of several magnetic relaxation processes in the low-frequency range.

Table 2.3. Best-fit parameters obtained by fitting Cole–Cole plots measured at various fields with a generalized Debye model for complex **2-1**.

Field (Oe)	τ(s)	α	χ_t (cm^3 mol^{-1})	χ_s(cm^3 mol^{-1})
500	0.00588	0.11988	1.15176	0.90719
750	0.00671	0.14105	1.14268	0.73065
1000	0.00776	0.16232	1.12945	0.58702
1250	0.00888	0.18037	1.11174	0.47889
1500	0.00996	0.20059	1.0915	0.3963
1750	0.1095	0.22081	1.06749	0.32947
2000	0.01207	0.23715	1.04114	0.27882

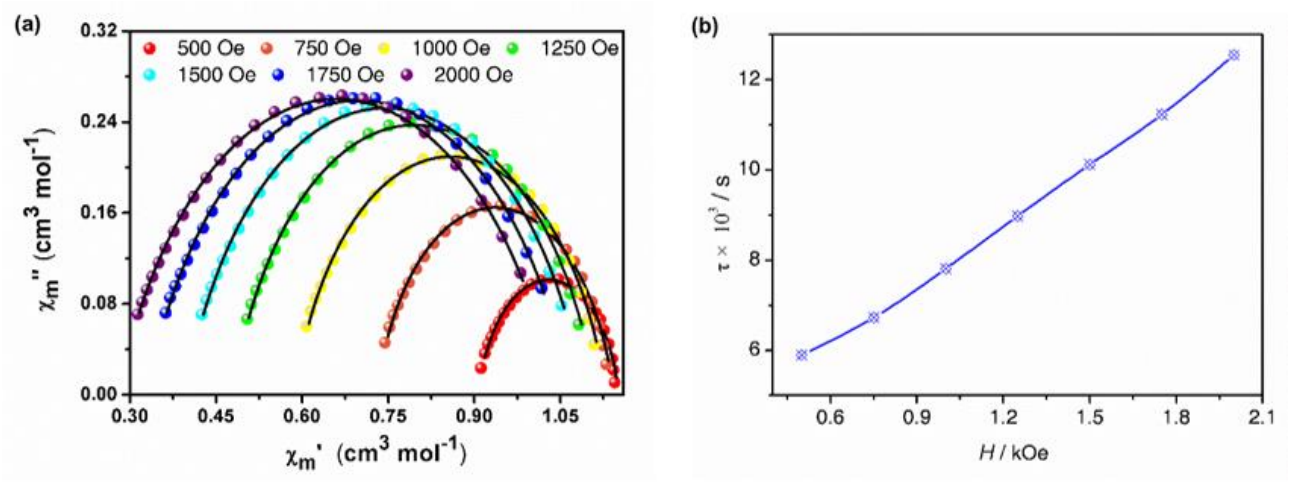

Figure 2.10. (a) Cole–Cole plot measured under various applied dc fields (500–2000 Oe) at 2 K for complex **2-1**. The solid lines represent the best fits to the experimental data using a modified Debye model. (b) Field dependence of magnetic relaxation time for complex **2-1**.

According to the above analysis, the variable-temperature ac magnetic susceptibility under different frequencies (Fig. 2.11) and isothermal frequency-dependent ac magnetic susceptibility (Fig. 2.12) were obtained under an external dc field of 1000 Oe for **2-1**. These ac data show obvious temperature and frequency dependence. The χ_m" vs. *T* curve produced a peak at ~2.6 K at a frequency of 1488 Hz, and the maximum of χ_m" obviously shifted to the lower-temperature region with decreasing frequency. The χ_m" vs. *v* curve exhibited a peak at ~95 Hz at 1.9 K, and the peak quickly shifted toward higher frequencies upon increasing the temperature. The magnetic relaxation time was extracted by fitting the Cole–Cole plot (Fig. 2.13a) to a modified Debye model. A plot of ln(τ) versus T^{-1} was shown in Fig. 2.13b. The best-fit α values are distributed in the range 0.09–0.18 (Table 2.4), which is an indication of multiple relaxation pathways and the remainder of tunneling effect.

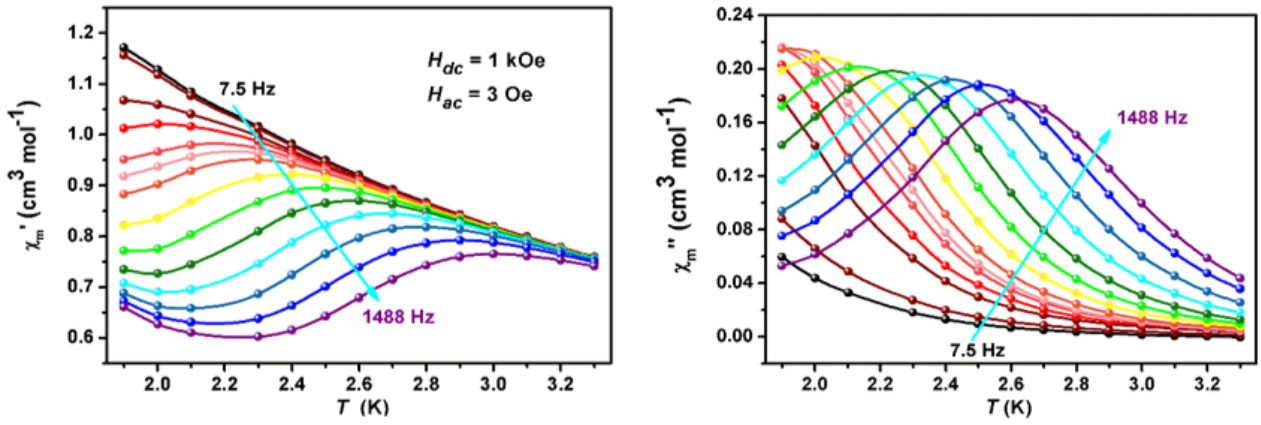

Figure 2.11. Temperature dependence of ac magnetic susceptibility under 1000 Oe for complex **2-1**.

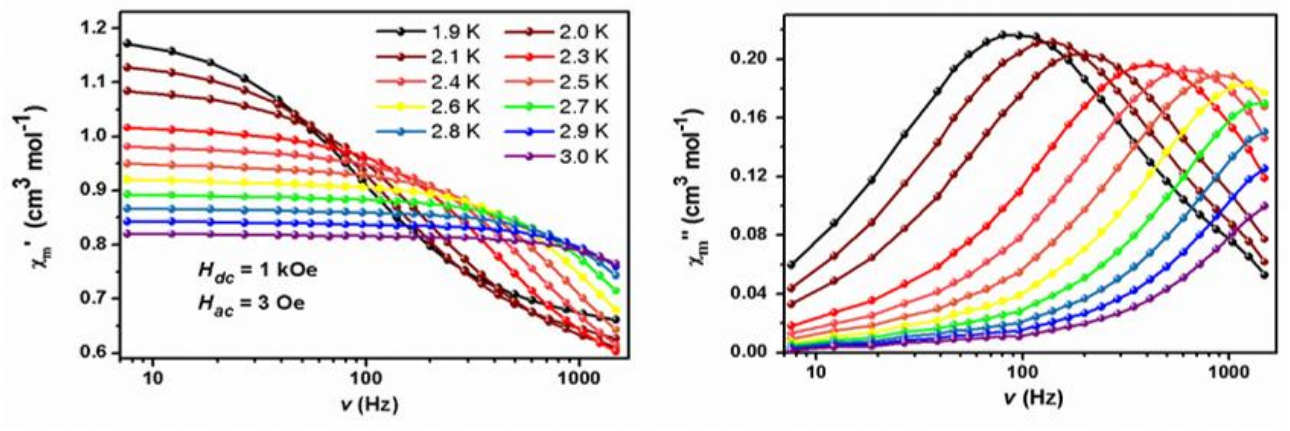

Figure 2.12. Frequency dependence of ac magnetic susceptibility measured at various T for **2-1**.

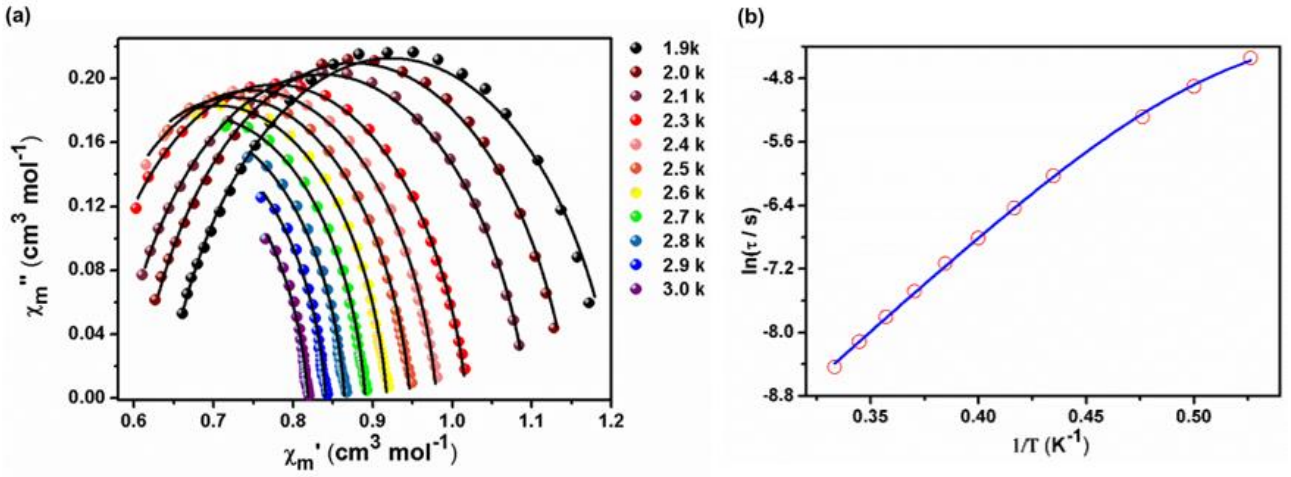

Figure 2.13. (a) Cole–Cole plot measured at various temperatures at 1000 Oe for **2-1**. The solid lines represent the best fits to the experimental data using a modified Debye model. (b) Temperature dependence of relaxation time shown in ln (τ) vs. T^{-1} plot for **2-1**. The solid line is the best–fit to the data based on eqn. (2.4).

Table 2.4. Best-fit parameters obtained by fitting Cole–Cole plots to a Debye model for **2-1**.

Field (Oe)	τ(s)	α	χ_t (cm^3 mol^{-1})	χ_s(cm^3 mol^{-1})
1.9	0.01063	0.18051	1.20618	0.63958
2.0	0.00745	0.16249	1.14761	0.60484
2.1	0.00502	0.15412	1.09517	0.57831
2.3	0.00241	0.13056	1.01839	0.53635
2.4	0.00161	0.11686	0.98083	0.5179
2.5	0.0011	0.10624	0.94733	0.50281
2.6	0.0007792	0.09568	0.91792	0.49266
2.7	0.0005638	0.08815	0.89075	0.48663
2.8	0.0004080	0.086	0.86487	0.47855
2.9	0.0002989	0.08482	0.84131	0.47235
3.0	0.0002168	0.09057	0.81888	0.46377

Therefore, the dependence of ln(τ) on T^{-1} was fitted based on an equation combining Orbach and tunneling terms:

$$\tau^{-1} = \tau_0^{-1} \exp\left(-U_{eff}/kT\right) + \tau_q^{-1} \qquad (2.4)$$

As shown in Fig. 2.13b, a well-fitted curve through all of the data was obtained, which affords an effective energy barrier of 17.0 cm^{-1}, a preexponential factor of $\tau_0 = 1.55 \times 10^{-7}$ s, and a tunneling relaxation time of $\tau_q = 0.017$ s for **2-1**. The U_{eff} value is lower than the values given by $U = D|S|^2$ with the D value determined from the dc magnetic data (23.4 cm^{-1}) or HF-EPR spectroscopy (24.0 cm^{-1}), but close to the energy gap (~18.0 cm^{-1}) between the pseudo-degenerate ground state (|+2⟩, |–2⟩) and the pseudo-degenerate first excited state (|+1⟩, |–1⟩) obtained by calculation. This feature indicates the Orbach process is through the energy barrier of the first excited state, as proposed for some other reported Fe(II) compounds showing field-induced SIM behaviors.[44-48]

The reported octa-coordinated Fe(II) complex $[Fe^{II}(L)_2](ClO_4)_2$ also exhibits field-induced slow magnetic relaxation.[48] The maximum of χ_m" for $[Fe^{II}(L)_2](ClO_4)_2$ appeals at much higher frequency range (> 690 Hz) than that of complex **2-1**. However, the reported results show that compound $[Fe^{II}(L)_2](ClO_4)_2$ possesses higher efficient reversal energy barrier (U_{eff} = 39. 1 cm^{-1}) than that of **2-1**, which indicated that higher reversal energy barrier does not generally lead to slower magnetic relaxation. This may be due to that complex $[Fe^{II}(L)_2](ClO_4)_2$ has a larger rhombic ZFS parameter (E = 0.08 cm^{-1}) originating from larger deviation of Fe(II) coordination environment from idea D_{2d} symmetry (86.38 ° for the inter-plane angle of two N_2O_2 planes).

2.3.5 Theoretical Calculations

To provide an insight into the peculiar electronic structure and thus the origin of the magnetic anisotropy for compound **2-1**, correlated *ab initio* calculations by the well-established CASSCF/NEVPT2 method have been carried out with the ORCA3.0.3 package.[50] The calculations give a relatively small excitation energy of 6742 cm^{-1} between the lowest ($d_{xy}^{2} d_{xz}^{1} d_{yz}^{1} d_{z^2}^{1} d_{x^2-y^2}^{1}$) and the highest quintet configuration ($d_{xy}^{1} d_{xz}^{1} d_{yz}^{1} d_{z^2}^{1} d_{x^2-y^2}^{2}$), confirming the weak overall ligand field from the tetradentate ligands (dpphen). As shown in Fig. 2.14 and Fig. 2.15, the d_{xy} orbital is locating on the lowest energy level with relatively large energy gaps to the d_{xz}, d_{yz} and d_{z^2} orbitals due to the weaker π* interaction compared with the σ* interaction. The quasi-degeneracy of the d_{xz} and d_{yz} orbitals results from the slight deviation of the geometry of $[Fe^{II}(dpphen)_2]^{2+}$ from D_{2d} symmetry. The stronger σ* repulsion between the Fe(II) center and the pyrazole groups leads to the highest orbital being $d_{x^2-y^2}$.

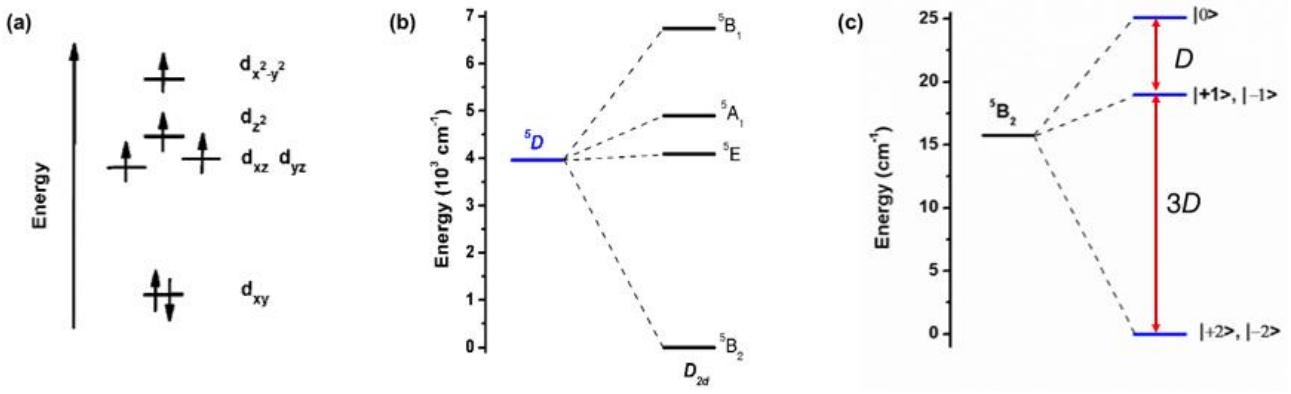

Figure 2.14. (a) calculated d-orbital splitting and electronic configuration of the ground state for compound **2-1**. (b) calculated splitting of the free-ion quintet state (S = 2) under the effect of a D_{2d} symmetric ligand field. (c) Calculated splitting of ground states under spin–orbit coupling of ground and excited states for **2-1**.

Spin–orbit coupling was taken into account by quasi-degenerate perturbation theory, which leads to the splitting of the ground state (Fig. 2.14c). Projecting the lowest five energy states of ground state obtained from CASSCF/NEVPT2 calculations onto a spin quintet $S = 2$ produced a full set of spin Hamiltonian parameters of $D = -6.32$ cm^{-1}, $|E| = 0.04$ cm^{-1}, $g_x = g_y = 2.05$, and $g_z = 2.11$, which are in good agreement with the results derived from the HF-EPR spectra. The very small E value was generated by the non-rigorous D_{2d} symmetry of the actual molecular structure, leading to quantum tunneling relaxation between pseudo-doublets. Regardless of the small deviation from ideal symmetry, the interaction between the $^5B_2$ and $^5B_1$ states contributes negatively (-6.36 cm^{-1}) to the overall D value, leading to the highly axial nature of the Fe(II) center. The contribution from the interaction between the ^5E states ($+2.42$ cm^{-1}) is approximately canceled by the contributions from interactions between different spin multiplicities (-2.50 cm^{-1}).

Based on the above theoretical analysis, one possible way to improve the axial anisotropy for this species of compounds is to enhance the donating ability of the coordination atoms near the S_4 axis to increase the antibonding interactions, or to reduce the donating effect of terminal groups to weaken the antibonding interactions. This strategy is supported by compound $[Fe^{II}(L)_2](ClO_4)_2$, for which two ester groups exert weaker ligand field on Fe center, and thus shows stronger uniaxial anisotropy with $D = -11.7$ cm^{-1}.[48] However, the compound $[Fe^{II}(L)_2](ClO_4)_2$ exhibits faster relaxation behavior compared with complex **2-1**, which may be related to that complex $[Fe^{II}(L)_2](ClO_4)_2$ features larger deviation of Fe(II) coordination environment from idea D_{2d} symmetry. This suggests that both molecular symmetry and ligand field should be carefully considered for further development of SMMs in high-coordinated complexes

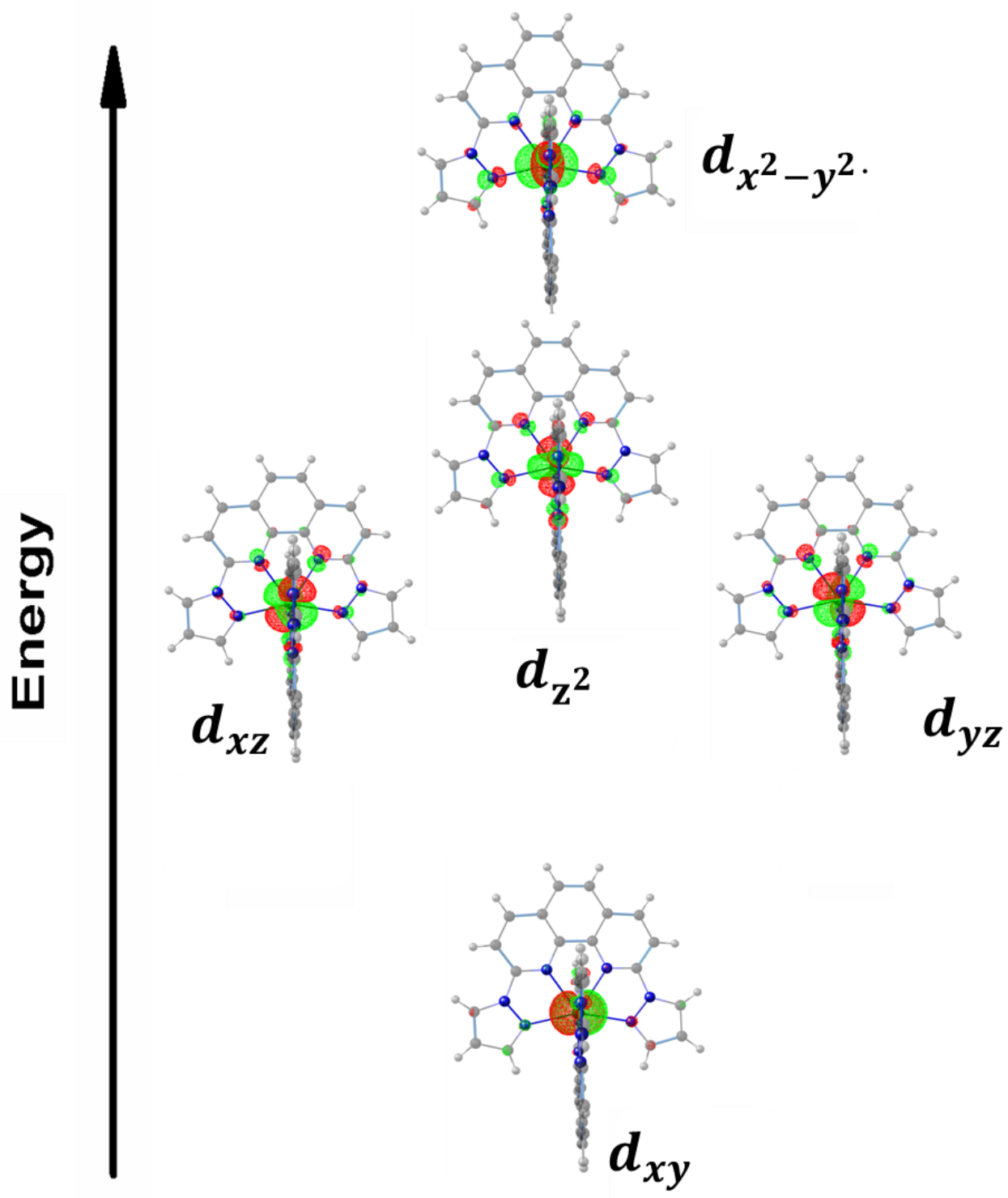

Figure 2.15. SA-CASSCF natural orbital shapes for complex **2-1**.

4. 4 Conclusion

An octa-coordinated Fe(II) complex, $[Fe^{II}(dpphen)_2](BF_4)_2 \cdot 1.3H_2O$ (**2-1**) with a pseudo-D_{2d} symmetric metal center has been synthesized. Magnetic, HF-EPR and theoretical investigations reveal that **2-1** characterizes uniaxial magnetic anisotropy with a negative axial zero-field splitting (ZFS) ($D \approx -6.0$ cm^{-1}) and a very small rhombic ZFS ($E \approx 0.04$ cm^{-1}). Under applied dc magnetic fields, complex **2-1** exhibits slow magnetic relaxation at low temperature. Fitting the relaxation time with the Arrhenius mode combining Orbach and tunneling terms affords a good fit to all the data and yields an effective energy barrier (17.0 cm^{-1}) close to the energy gap between the ground state and the first-excited state. The origin of the strong uniaxial magnetic anisotropy for **2-1** has been clearly understood from theoretical calculations.

Our work on this octa-coordinated Fe(II) complex confirms that D_{2d} symmetry can limit the rhombic ZFS in a small level for high-coordinated magnetic complexes, which is in favor of them to exhibit SIM behavior. The smaller rhombic ZFS (E) is, the slower magnetization relaxation may be observed for the mononuclear magnetic compound. More importantly, these results suggest that both molecular symmetry and ligand field should be carefully take into account for further design interesting SIMs in high-coordinated complexes.

References

(1) R. Sessoli, D. Gatteschi, A. Caneschi, M. A. Novak, *Nature* **1993**, *365*, 141–143.

(2) D. Gatteschi, R. Sessoli, *Angew. Chem. Int. Ed.* **2003**, *42*, 268–297.

(3) R. E. P. Winpenny, *Angew. Chem. Int. Ed.* **2008**, *47*, 7992–7994.

(4) L. Bogani, W. Wernsdorfer, *Nat. Mater.* **2009**, *7*, 179–186.

(5) R. Sessoli, H. L. Tsai, A. R. Schake, S. Wang, J. B. Vincent, K. Folting, D. Gatteschi, G. Christou, D. N. Hendrickson, *J. Am. Chem. Soc.* **1993**, *115*, 1084–1816.

(6) C. J. Milios, A. Vinslava, W. Wernsdorfer, S. Moggach, S. Parsons, S. P. Perlepes, G. Christou, E. Brechin, *J. Am. Chem. Soc.* **2007**, *129*, 2754–2755.

(7) R. Bagai, G. Christou, *Chem. Soc. Rev.* **2009**, *38*,1011–1026.

(8) M. Murrie, *Chem. Soc. Rev.* **2010**, *39*, 1986–1995.

(9) N. Ishikawa, M. Sugita, T. Ishikawa, S. Koshihara, Y. Kaizu, *J. Am. Chem. Soc.* **2003**, *125*, 8694–8695.

(10) L. Sorace, C. Benelli, D. Gatteschi, *Chem. Soc. Rev.* **2011**, *40*, 3092–3104.

(11) P. Zhang, Y.-N. Guo, J.-K. Tang, *Coord. Chem. Rev.* **2013**, *257*, 1728–1763.

(12) D. N. Woodruff, R.E.P. Winpenny, R. A. Layfield, *Chem. Rev.* **2013**, *113*, 5110–5148.

(13) P. Zhang, L. Zhang, C. Wang, S.-F. Xue, S.-Y. Lin, J.-K. Tang, *J. Am. Chem. Soc.* **2014**, *136*, 4484–4487.

(14) J. Long, J. Rouquette, J.-M. Thibaud., R. A. S. Ferreira, L. D. Carlos, B. Donnadieu, V. Vieru, L. F. Chibotaru, L. Konczewicz, J. Haines, Y. Guari, J. Larionova, *Angew. Chem. Int. Ed.* **2015**, *54*, 2236–2240.

(15) J. Liu, Y.-C. Chen, J.-L. Liu, V. Vieru, L. Ungur, J.-H. Jia, L. F. Chibotaru, Y Lan, W. Wernsdorfer, S. Gao, X.-M. Chen, M.-L. Tong, *J. Am. Chem. Soc.* **2016**, *138*, 5441–5450.

(16) Y.-S. Ding, N. F. Chilton, R. E. P. Winpenny, Y.-Z. Zheng, *Angew. Chem. Int. Ed.* **2016**, *55*, 16071–16074.

(17) J. Goura, J. Brambleby, P. Goddard, V. Chandrasekhar, *Chem.-Eur. J.* **2015**, *21*, 4926–4930.

(18) Y.-S. Meng, Y.-Q. Zhang, Z.-M. Wang, B.-W. Wang, S. Gao, *Chem.-Eur. J.* **2016**, *22*, 12724–12731.

(19) D. E. Freedman, W. H. Harman, T. D. Harris, G. J. Long,C. J. Chang, J. R. Long, *J. Am. Chem. Soc.* **2010**, *132*, 1224–1225.

(20) J. M. Zadrozny, D. J. Xiao, M. Atanasov, G. J. Long, F. Grandjean, F. Neese, J. R. Long, *Nat. Chem.* **2013**, *5*, 577–581.

(21) G. A. Craig, M. Murrie, *Chem. Soc. Rev.* **2015**, *44*, 2135–21347.

(22) A. K. Bar, C. Pichon, J.-P. Sutter, *Coord. Chem. Rev.* **2016**, *308*, 346–380.

(23) M. Ding, G. E. Cutsail III, D. Aravena, M. Amoza, M. Rouzières, P. Dechambenoit, Y. Losovyj, M. Pink, E Ruiz, R. Clérac, J. M. Smith, *Chem. Sci.* **2016**, *7*, 6132–6140.

(24) Y. Rechkemmer, F. D. Breitgoff, M. V. D. Meer, M. Atanasov, M. Hakl, M. Orlita, P. Neugebaure, F. Neese, B. Sarkar, J. van Slageren, *Nat. Commun.* **2015**, *7*, 10467.

(25) F. Shao, B. Cahier, N. Guihéry, E. Rivière, R. Guillot, A.-L. Barra, Y. Lan, W. Wernsdorfer, V. E. Campbell, T. Mallah, *Chem. Commun.* **2015**, *51*, 16475–16478.

(26) W. Lin, T. Bodenstein, V. Mereacre, K. Fink, A. Eichhöfer, *Inorg. Chem.* **2016**, *55*, 2091–2100.

(27) J. Miklovič , D. Valigura , R. Boča, J. Titiš, *Dalton Trans.* **2015**, *44*, 12484–12487.

(28) Y.-F. Deng, T. Han, Z. Wang, Z. Ouyang, B. Yin, Z. Zheng, J. Krzystek, Y.-Z. Zheng, *Chem. Commun.* **2015**, *51*, 17688–17691.

(29) J. H. Christian, D. W. Brogden, J. K. Bindra, J. S. Kinyon, J. van Tol, J. Wang, J. F. Berry, N. S. Dalal, *Inorg. Chem.* **2016**, *55*, 6367–6383.

(30) J. Vallejo, I. Castro, R. Ruiz-García, J. Cano, M. Julve, F. Lloret, G. De Munno, W. Wernsdorfer, E. Pardo, *J. Am. Chem. Soc.* **2012**, *134*, 15704–15707.

(31) Y.-Z. Zhang, S. Gómez-Coca, A. J. Brown, M. R. Saber, X. Zhang, K. R. Dunbar, *Chem. Sci.* **2016**, *7*, 6519–6527.

(32) J. Li, Y. Han, F. Cao, R.-M. Wei, Y.-Q. Zhang, Y. Song, *Dalton trans.* **2016**, *45*, 9279–9284.

(33) V. V. Novikov, A. A. Pavlov, Y. V. Nelyubina, M.-E. Boulon, O. A. Varzatskii, Y. Z. Voloshin, R. E. P. Winpenny, *J. Am. Chem. Soc.* **2015**, *137*, 9792–9796.

(34) Y.-Y. Zhu, Y.-Q. Zhang, T.-T. Yin, C. Gao, B.-W. Wang, S. Gao, *Inorg. Chem.* **2015**, *54*, 5475–5486.

(35) C. Plenk, J. Krause E. Rentschler, *Eur. J. Inorg. Chem.* **2015**, *2015*, 370–374.

(36) Y. Y. Zhu, C. Cui, Y. Q. Zhang, J. H. Jia, X. Guo, C. Gao, K. Qian, S. D. Jiang, B. W. Wang, Z. M. Wang, S. Gao, *Chem. Sci.* **2013**, *4*, 1802–1806.

(37) R. Herchel, L. Váhovská, I. Potoňák, Z. Trávníček, *Inorg. Chem.* **2014**, *53*, 5896–5898.

(38) S. Gómez-Coca, A. Urtizberea, E. Cremades, P. J. Alonso, A. Camón, E. Ruiz, F. Luis, *Nat. Commun.* **2014**, *5*, 4300.

(39) E. Colacio, J. Ruiz, E. Ruiz, E. Cremades, J. Krzystek, S. Carretta, J. Cano, T. Guidi, W. Wernsdorfer, E. K. Brechin, *Angew. Chem. Int. Ed.* **2013**, *52*, 9130–91304.

(40) V. Chandrasekhar, A. Dey, A. J. Mota, E. Colacio, *Inorg. Chem.* **2013**, *52*, 4554–4561.

(41) L. Chen, S.-Y. Chen, Y.-C. Sun, Y.-M. Guo, L. Yu, X.-T. Chen, Z. Wang, Z. W. Ouyang, Y. Song, Z.-L. Xue, *Dalton Trans.* **2015**, *44*, 11482–11490.

(42) X. C. Huang, C. Zhou, D. Shao, X. Y. Wang, *Inorg. Chem.* **2014**, *53*, 12671–12673.

(43) L. Chen, J. Wang, J. M. Wei, W. Wernsdorfer, X. T. Chen, Y. Q. Zhang, Y. Song, Z. L. Xue, *J. Am. Chem. Soc.* **2014**, *136*, 12213–12216.

(44) X. Feng, C. Mathonière, I.-R. Jeon, M. Rouzières, A. Ozarowski, M. L. Aubrey, M. I. Gonzalez, R. Clérac, J. R. Long, *J. Am. Chem. Soc.* **2013**, *135*, 15880–15884.

(45) A. K. Bar, C. Pichon, N. Gogoi, C. Duhayon, S. Ramasesha, J.-P. Sutter, *Chem. Commun.* **2015**, *51*, 3616–3619.

(46) A. Urtizberea, O. Roubeau, *Chem. Sci.* **2017**, *8*, 2290–2295.

(47) A. Pascual-Álvarez, J. Vallejo, E. Pardo, M. Julve, F. Lloret, J. Krzystek, D. Armentano, W.

Wernsdorfer, J. Cano, *Chem.-Eur. J.* **2015**, *21*,17299–17307.

(48) J. Xiang, J.-J. Liu, X.-X. Chen, L.-H. J, F. Yu, B.-W. Wang, S. Gao, T.-C Laud, *Chem. Commun.* **2017**, *53*, 1474–1477.

(49) G. M. Sheldrick, *Acta Cryst. C* **2015**, 71, 3–8.

(50) M. J. Frisch, et al., *Gaussian, Inc., Wallingford CT*, **2010**.

(51) A. D. Becke, *Phys. Rev. A* **1988**, *38*, 3098–3100.

(52) J. P. Perdew, *Phys. Rev. B* **1986**, *33*, 8822–8824.

(53) F. Weigend, R. Ahlrichs, *Phys. Chem. Chem. Phys.* **2005**, *7*, 3297–3305.

(54) F. Weigend, *Phys. Chem. Chem. Phys.* **2006**, *8*, 1057–1065.

(55) D. Schweinfurth, M. G. Sommer, M. Atanasov, S. Demeshko, S. Hohloch, F. Meyer, F. Neese, B. Sarkar, *J. Am. Chem. Soc.* **2015**, *137*, 1993–2005.

(56) M. Seredyuk, L. Piñeiro-López, M. C. Muñoz, F. J. Martínez-Casado, G. Molnár, J. A. Rodriguez-Velamazán, A. Bousseksou, J. A. Real, *Inorg. Chem.* **2015**, *54*, 7424–7432.

(57) A. K. Patra, K. S. Dube, G. C. Papaefthymiou, J. Conradie, A. Ghosh, T. C. Harrop, *Inorg. Chem.* **2010**, *49*, 2032–2034.

(58) N. F. Chilton, R. P. Anderson, L. D. Turner, A. Soncini, K. S. Murray, *J. Comput. Chem.* **2013**, *34*, 1164–1175.

(59) A. Ozarowski, S. A. Zvyagin, W. M. Reiff, J. Telser, L.-C. Brunel, J. Krzystek, *J. Am. Chem. Soc.* **2004**, *126*, 6574–6575.

(60) J. Telser, J. van Slageren, S. Vongtragool, M. Dressel, W. M. Reiff, S. A. Zvyagin, A. Ozarowski, J. Krzystek, *Magn. Reson. Chem.* **2005**, 43: s130–s139.

(61) J. Krzystek, D. Smirnov, C. Schlegel, J. van Slageren, J. Telser, A Ozarowski, J. *Magn. Reson.* **2011**, *153*, 158–165.

(62) W. H. Harman, T. D. Harris, D. E. Freedman, H. Fong, A. Chang, J. D. Rinehart, A. Ozarowski, M. T. Sougrati, F. Grandjean, G. J. Long, J. R. Long, C.J. Chang, *J. Am. Chem. Soc.* **2010**,

132, 18115–18126.

(63) K. Park, M. A. Novotny, N. S. Dalal, S. Hill, P. A. Rikvold, *Phys. Rev. B* **2001**, *65*, 014426.

(64) F. Habib, Korobkov, M. Murugesu, *Dalton Trans.* **2015**, *44*, 6368–6373.

(65) J. M. Zadrazny, M. Atansov, A. M. Bryan, C.-Y. Lin, B. D. Rekken, P. P. Power, F. Neese, J. R. Long, *Chem. Sci.* **2013**, *4*, 125–138.

Chapter 3. Spin Transition of Fe(II) in an Fe^{II}/Fe^{III} Mixed-Valence Chain

3. 1 Introduction

In 1996, thermal and photo switchable electronic bistablility has been observed in the Prussian blue analogue $K_{0.14}Co[Fe(CN)_6]_{0.7}\cdot 5H_2O$.[1] After that, Cyanide-bridged metal complexes, namely Prussian blue analogues, have received considerable research attentions for their abundant structures and intriguing magnetic and optical properties.[2-5] Magnetic bistability through electron dynamics are most fascinating properties in analogous Prussian blue system. As for a cyanide-bridged metal compound, it comprises the basic unit of M–CN–M' (M and M' stand for metal ions). Hence, electron dynamic behaviors in cyanide-bridged metal complexes may involve electron conformation changing in one metal ion site (spin crossover in M'), or electron transfers from one metal site to the other metal site (MMCT), or electron transfers from one metal site to the other metal site and subsequently causes the electron conformation changing in one metal site (CTCST). All of these electron dynamic behaviors would induce some interesting physical properties switching in the cyanide-bridged compounds.[2]

To achieve the above magnetic bistabilities in Prussian blue analogues, the most important strategy is subtly selecting the assemble units, including cyanide containing metal building blocks (cyanometallates), metal ions, and coordination ligands. There are various stable cyanometallates, such as cyanoferrates, cyanoosmates, and some octacyanometallates ($[Mo^{IV/V}(CN)_8]^{4-/3-}$, $[W^{IV/V}(CN)_8]^{4-/3-}$), which can be used for assembling electronic bistable complexes. The prevalent metal ions for M' are Fe(II/III), Co(II/III), and Mn(II/III) due to their variable valence and spin states. The coordination ligands play significant roles to adjust the redox potential, ligand field, and coordination surroundings of the two metal sites linked by cyanide group. Up to now, tunable electron dynamic behaviors have been observed in many cyanide-bridged heterometallic complexes, such as FeCo,[6-21] FeFe,[22-27] WFe,[28] OsFe,[29] WCo,[30, 31] FeMn,[32-34] OsCo,[35] MoCu[36-40] and FeCoW[41].

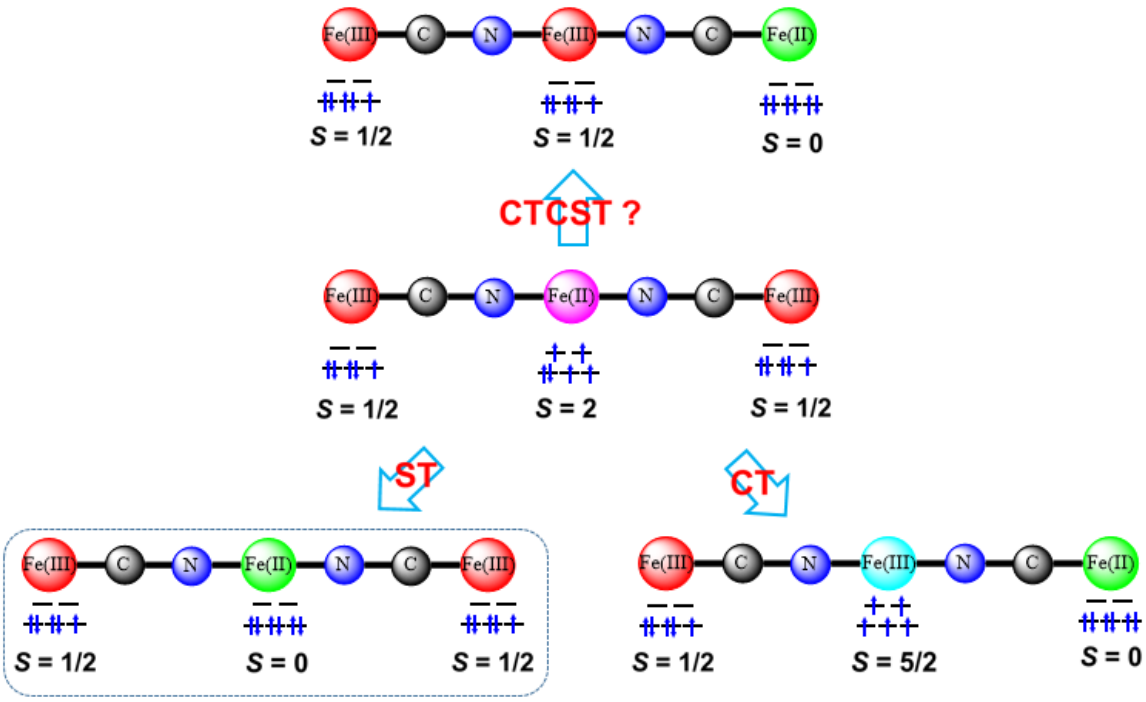

Scheme 3.1. Possible electron dynamic behaviors in cyanide-bridged mixed-valence Fe^{II}/Fe^{III} compound (ST = spin transition; CT = charge transfer and CICST = charge transfer coupling spin transition).

Recently, our group shift attention to the cyanide-bridged mixed valence Fe^{II}/Fe^{III} system. With the concerted efforts of former members in our group, SCO and MMCT behaviors have been respectively observed in two cyanide-bridged Fe^{II}/Fe^{III} one-dimensional (1D) double-zigzag chains. Complex $\{[Fe^{III}(Tp^*)(CN)_3]_2Fe^{II}(bpmh)\}\cdot 2H_2O$ (Tp* = hydrotris(3,5-dimethylpyrazolyl)borate; bpmh = N,N0-bis-pyridin-4-ylmethylene hydrazine) exhibits thermal and light induced SCO behavior at the Fe(II) site.[25] More interestingly, the light-excited state of this compound shows single-chain magnetic behavior. Whereafter, a similar double-zigzag chain $\{[Fe(Tp)(CN)_3]_2Fe(bpe)\cdot 5H_2O\}_n$ (Tp = hydrotris(pyrazolyl)borate; bpe=1,2-bis(4-pyridyl)ethane) manifests thermal induced MMCT between cyanide-bridged two Fe sites.[27] Based on these results, we want to realize CTCST behavior and except some interesting physical properties in cyanide-bridged mixed valence Fe^{II}/Fe^{III} system. Unfortunately, the target compound has not been obtained yet. Nevertheless, a new cyanide-bridged Fe^{II}/Fe^{III} 1D double-zigzag chain, $\{[Fe(Tp)(CN)_3]_2Fe(btb)\cdot 1H_2O\}_n$ (**3-1**) (btb = 1,4-(1H-1,2,4-

triazole)butane) exhibit SCO behavior has been obtained by careful selection of the cyanoferrate and coordination ligand. Additionally, a new trinuclear cyanide-bridged Fe^{II}/Fe^{III} complex $[Fe(Tp)(CN)_3]_2Fe(btb)_2\cdot 2H_2O$ (**3-2)** that remain electron state unchanged was obtained by using the same cyanoferrate and ligand under different reaction condition.

3. 2 Experimental Section

3.2.1 Starting Materials and Synthesis Methods

All of the chemical reagents were commercially obtained and used directly. $Li[Fe^{III}(TP)(CN)_3]$, $(Bu_4N)[Fe^{III}(pzTP)(CN)_3]$, and btb were synthesized according to the literatures.[42,43]

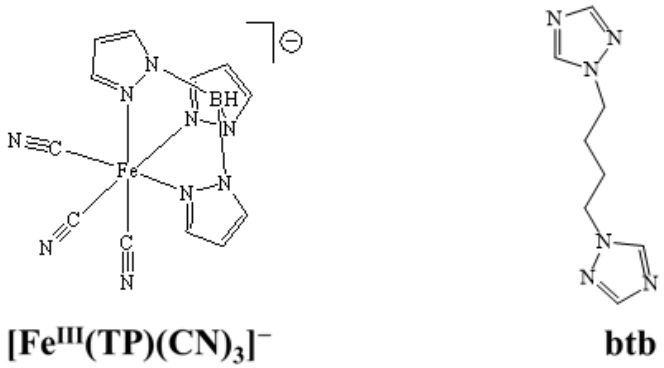

$[Fe^{III}(TP)(CN)_3]^-$ **btb**

Scheme 3.2. Schematic structure of $[Fe^{III}(TP)(CN)_3]^-$ and 1,4-(1H-1,2,4-triazole)butane (btb).

Synthesis of $Li[Fe^{III}(TP)(CN)_3]$. $FeCl_2\cdot 4H_2O$ (2.0 g, 0.01 mol) in methanol (50 ml) was slowly added to the mixture of KTp (5.0 g) in water (50 ml) under stirring. Purple precipitation of $Fe(TP)_2$ was formed during the above process. After the reaction, the product was collected by filtration and dried in vacuum. A mixture of $Fe(TP)_2$ and KCN (2.0 g, 0.03 mol) in 2-propanol was heated at 80 ºC for more than 12 h under violent stirring. The color of the solid changed from purple to yellow during the reaction. After cooling to room temperature, the yellow solid was collected via filtration and air-dried. The obtained solid was dissolved in water, and the insoluble solid was removed by filtering. Terabutylammonium bromide (3.22 g, 0.01 mol) was added to the filtrate. And then 30% H_2O_2 was

added very slowly, during which orange product $(Bu_4N)[Fe^{III}(TP)(CN)_3]$ was formed. The product was collected by filtration, which was washed by water air-dried. The lithium salt $Li[Fe^{III}(TP)(CN)_3]$ was obtained through ion exchanging reaction of $(Bu_4N)[Fe^{III}(TP)(CN)_3]$ with $LiClO_4$ in acetonitrile. The final yield is ca. 56% (based on iron salt).

Synthesis of btb. A mixture of 1H-1,2,4-triazole (2.8 g, 0.04 mol), 40% NaOH (14 ml), Terabutylammonium bromide (0.6 g, 18.8 mmol), and 1,4-dibromobutane (4.4 g, 0.02 mol) in 40 ml toluene was heated at 80 ºC for 72 h under violent stirring. After cooling to room temperature, the organic phase and aqueous phase were separated. The aqueous phase was extracted with CH_2Cl_2 (30 ml) for 3 times, and the extraction was combined with the above organic phase. Colorless crystals of btb were obtained by slowly evaporating the organic solvent. Yield: ca. 35%.

Synthesis of $\{[Fe(Tp)(CN)_3]_2Fe(btb)\}_n$ (3-1). $Fe(ClO_4)_2 \cdot 6H_2O$ (36.5 mg, 0.01 mmol) in water (10 ml) was added to the mixture of $Li[Fe^{III}(TP)(CN)_3]$ (70.8 mg, 0.02 mol) and btb (19.2 mg, 0.01 mmol) in water (15 ml) under stirring. Ethanol (5 ml) was added to the above mixture, and then the mixture was equally separated to six autoclaves. The autoclaves were heated at 120 ºC for 1 h. After slowly cooling to 30 ºC, red needle crystals of compound **3-1** were collected via filtration, and washed with small amount of ethanol. Yield: ca. 40%. Anal. Calcd ($C_{32}H_{32}B_2Fe_3N_{24}$): C 40.80, H 3.42, B 2.30, Fe 17.79, N 35.69. Found: Found: C 40.20, H 3.43, N 35.10.

Synthesis of $[Fe(Tp)(CN)_3]_2Fe(btb)_2 \cdot 2H_2O$ (3-2). A mixture of $Fe(CF_3SO_3)_2$ (35.4 mg, 0.01 mmol), $(Bu_4N)[Fe^{III}(pzTP)(CN)_3]$ (127.8 mg, 0.02 mmol) and btb (19.2 mg, 0.01 mmol) in 3 DMF solution was placed in relatively dry surrounding. Red needle crystal sample of complex 2-2 can be obtained by slow evaporation of DMF solvent. Yield: ca. 20%. Anal. Calcd ($C_{40}H_{48}B_2Fe_3N_{30}O_2$): C 41.05, H 4.13, N 35.91. Found: Found: C 41.20, H 4.16, N 35.83.

3.2.2 Physical Measurements

Crystal structural analysis. The crystal data of **3-1** collected on a Rigaku FR-E+ CCD

diffractometer with Mo-Kα radiation. All the structures were solved via direct method and refined by the full-matrix least-squares technique on F^2 by on the SHELXTL program.[44] All H atoms on C atoms were geometrically produced and refined using a riding model. While H atoms on lattice water can be found from difference Fourier maps, for which O-H distance were normalized to 0.82 Å.

Other physical measurement. Magnetic measurements were performed on a Quantum Design MPMS-XS SQUID magnetometer. Light-irradiation of the sample (**3-1**) was carried out with a laser diode pumped Nd:YAG laser (758 nm). The UV-vis absorption spectra for solid sample were recorded in the range 400–800 nm on a UV-3100 PC spectrometer. Infrared (IR) spectra (CaF_2 pellet) were recorded in the range 1000–4000 cm^{-1} on a JASCO FT/IR-600 Plus spectrometer. Elemental analyses were carried out on a Yanaco CHN CORDER MT-6 elemental analyzer.

3. 3 Results and Discussion

3.3.1 Crystal Structure Analysis

Single-crystal X-ray analysis indicates that compound **3-1**crystallized in a monoclinic space group $P\,2_1/c$ (Table 3.1) at 296 K. The crystal structure of complex **3-1** is consistent of neutral mixed valence $\{Fe^{III}_2Fe^{II}\}_n$ double-zigzag chains (Figure 3.1). In the mixed valence $\{Fe^{III}_2Fe^{II}\}_n$ double-zigzag chain, each $[Fe^{III}(TP)(CN)_3]^-$ entities connected with two independent Fe(II) center via two of its three CN^- groups in the *cis*-positions, and each Fe(II) center coordinated with four N atoms of CN^- groups from four independent $[Fe^{III}(TP)(CN)_3]^-$ blocks in its equatorial positions, which generates the frame of the double-zigzag chain. Additionally, the two coordination sites of Fe(II) in the axial positions were occupied by two N atoms from two btb ligands, and each btb ligand stretched over the $Fe^{III}_2Fe^{II}_2$ square unit and coordinated with two Fe(II) sites through the N atoms in its two triazole groups. The btb ligands linked by the Fe(II) ions forming a wave line-like shape in one double-zigzag chain. The double-zigzag chains are almost parallel to each other and extend along crystalline *c*-axis. The shortest interchain Fe···Fe distance is 10.393 Å.

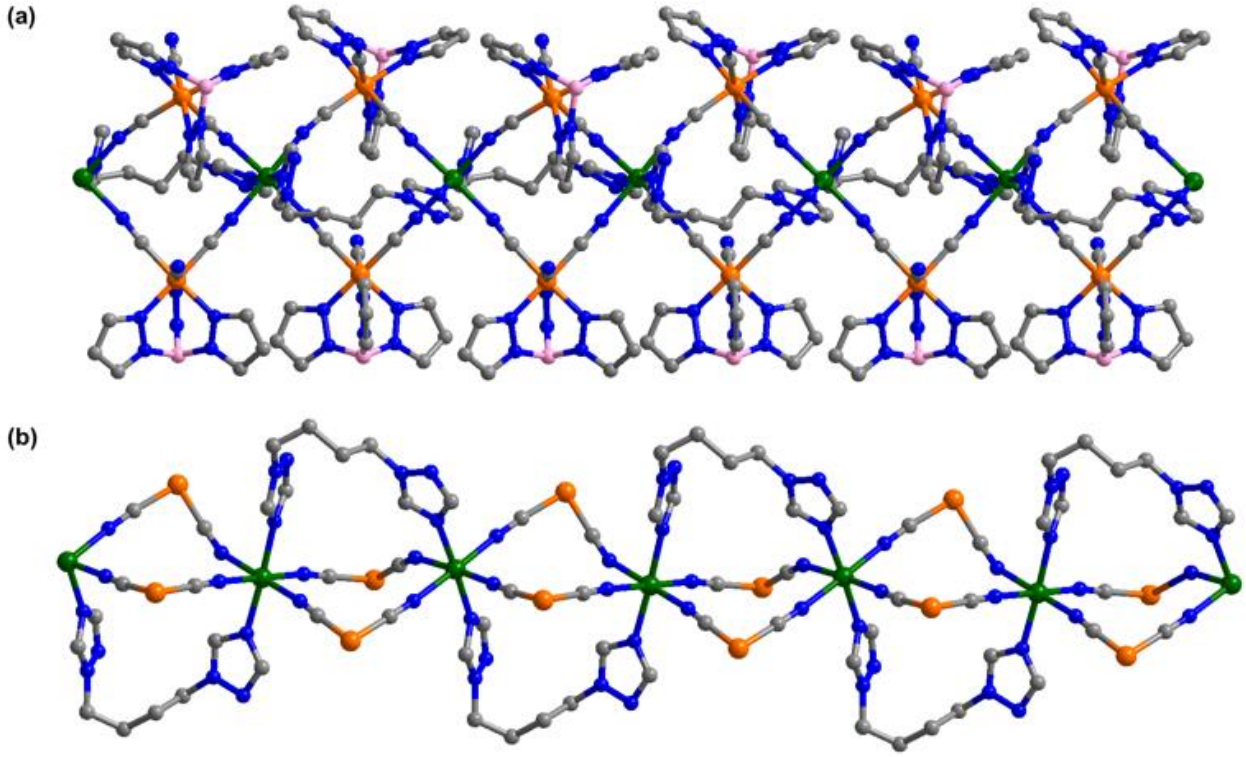

Figure 3.1. Crystal structure of complex **3-1** (Fe^{3+}, Fe^{2+},C, N and B atoms are represented by orange, green, grey, blue and pink ball, respectively. H atoms were omitted for clarity. Tp ligands and terminal CN^- groups beyond the double-zigzag chain were also omitted in (b)).

The repetitive unit of the double-zigzag chain contained two independent Fe(III) sites and a unique Fe(II) site. The Fe(III) ion was coordinated by three N atoms from the Tp ligand and three C atoms from three CN^- groups, the Fe−N_{Tp} bonds lengths are in the range of 1.963(5) − 1.981(5) Å, and the average Fe−C bonds distance is 1.917(6) Å, which are comparable with the $Fe^{III}(TP)(CN)_3]^-$ blocks in other complexes and suggest that the Fe(III) centers in the double-zigzag chain are low-spin.[6-13] The Fe(II) center was coordinated by four N atoms from CN^- and two N from btb ligands, forming a slightly elongated octahedral geometry with two axial Fe−N_{btb} bonds (2.172(6) and 2.175(5) Å) a little longer than Fe−N_{CN} (2.137(5)- 2.161(6) Å) in the equatorial positions. More importantly, the Fe−N bonds lengths reveal that the Fe(II) ions in the $\{Fe^{III}_2Fe^{II}\}_n$ double-zigzag chain are in high-spin (HS) states.

Table 3.1. Crystallographic parameters of complexes **3-1**.

Compound	**3-1 (HS)**	**3-1 (LS)**
Formula	C_{32} H_{32} B_2 Fe_3 N_{24}	C_{32} H_{32} B_2 Fe_3 N_{24}
Formula weight	941.93	941.93
Temp. (K)	296	100
Crystal System	monoclinic	monoclinic
Space group	*P* $2_1/c$ (No. 14)	*P* $2_1/c$ (No. 14)
a (Å)	15.6054(6)	15.432(3)
b (Å)	20.4603(9)	20.417(4)
c (Å)	13.9175(6)	13.607(3)
α (°)	90	90
β (°)	102.268(4)	101.23(3)
γ (°)	90	90
Volume (Å^3)	4342.3(3)	4205.1(15)
Z	4	4
$\rho_{calcd.}$(g cm^{-3})	1.441	1.464
μ (Mo-$K\alpha$)	1.044	1.080
F(000)	1920.00	1828
θ range (°)	1.74–29.28	2.995–27.367
Independent reflections	10577	5463
R_1 ($I > 2.0\sigma$)	0.0942	0.1668
wR_2 (*all data*)	0.2243	0.4045
Goodness-of-fit on F^2	1.020	1.089

[a] $R = \sum||F_0|-|F_c||)/\sum|F_0|$ [b] $w\mathrm{R} = |\sum w(F_0-F_c)^2/\sum w(F_0^2)^2|^{1/2}$

Table 3.2. Selected bond distances (Å) and angles (°) for complex **3-1** at HT.

Fe(II)		Fe(III)		Fe(III)	
Fe1−N1	2.175(5)	Fe2−C9	1.897(6)	Fe3−C10	1.915(6)
Fe1−N4^{i}	2.172(6)	Fe2−C11	1.916(6)	Fe3−C22	1.920(9)
Fe1−N7	2.137(5)	Fe2−C12	1.926(7)	Fe3−C23	1.916(7)
Fe1−N8	2.157(6)	Fe2−N11	1.981(5)	Fe3−N19	1.983(6)
Fe1−N9^{i}	2.145(6)	Fe2−N13	1.976(5)	Fe3−N21	1.979(5)
Fe1−N18^{i}	2.161(6)	Fe2−N15	1.963(5)	Fe3−N23	1.971(6)
N1−Fe1−N4^{i}	176.8(2)	C9−Fe2−C11	85.2(2)	C10−Fe3−C22	88.5(3)
N1−Fe1−N7	92.0(2)	C9−Fe2−C12	88.4(3)	C10−Fe3−C23	85.7(3)
N1−Fe1−N8	88.4(2)	C11−Fe2−C12	87.5(3)	C22−Fe3−C23	87.9(3)
N1−Fe1−N9^{i}	90.5(2)	C9−Fe2−N11	178.2(2)	C10−Fe3−N19	90.8(3)
N1−Fe1−N18^{i}	87.6(2)	C9−Fe2−N13	91.5(2)	C10−Fe3−N21	176.3(2)
N4^{i} −Fe1−N7	91.0(2)	C9−Fe2−N15	91.8(3)	C10−Fe3−N23	95.2(3)
N4^{i}−Fe1−N8	88.5(2)	C11−Fe2−N11	93.1(2)	C22−Fe3−N19	179.1(3)
N4^{i}−Fe1−N9^{i}	90.4(2)	C11−Fe2−N13	176.3(2)	C22−Fe3−N21	92.2(3)
N4^{i}−Fe1−N18^{i}	91.3(2)	C11−Fe2−N15	94.1(3)	C22−Fe3−N23	92.3(3)
N7−Fe1−N8	178.4(2)	C12−Fe2−N11	92.2(3)	C23−Fe3−N19	91.6(2)
N7−Fe1−N9^{i}	93.9(2)	C12−Fe2−N13	90.8(2)	C23−Fe3−N21	90.7(2)
N7−Fe1−N18^{i}	90.1(2)	C12−Fe2−N15	178.4(3)	C23−Fe3−N23	179.1(3)
N8−Fe1−N9 ^{i}	87.7(2)	N11−Fe2−N13	90.2(2)	N19−Fe3−N21	88.5(2)
N8−Fe1−N18^{i}	88.3(2)	N11−Fe2−N15	87.6(2)	N19−Fe3−N23	88.2(3)
N9^{i}−Fe1−N18^{i}	175.7(2)	N13−Fe2−N15	87.6(2)	N21−Fe3−N23	88.4(2)

Symmetric operate with code i: *x, 3/2− y, 1/2 + z*

Table 3.3. Selected bond distances (Å) and angles (°) for complex **3-1** at LT.

Fe(II)		Fe(III)		Fe(III)	
Fe1−N1	2.01(2)	Fe2−C1	1.84(2)	Fe3−C13	1.94(3)
Fe1−N2 ^{i}	1.948(15)	Fe2−C2	1.94(2)	Fe3−C14	1.942(17)
Fe1−N10	1.93(2)	Fe2−C3	1.89(2)	Fe3−C15	1.84(2)
Fe1−N11^{i}	1.977(16)	Fe2−N5	2.011(17)	Fe3−N13	1.952(17)
Fe1−N19	1.986(18)	Fe2−N7	1.984(17)	Fe3−N15	1.997(18)
Fe1−N22	1.983(17)	Fe2−N9	1.935(19)	Fe3−N17	2.005(16)
N1−Fe1−N2^{i}		C1−Fe2−C2	84.8(10)	C13−Fe3−C14	87.8(8)
N1−Fe1−N10		C1−Fe2−C3	90.2(10)	C13−Fe3−C15	89.7(11)
N1−Fe1−N11 ^{i}		C2−Fe2−C3	88.0(9)	C14−Fe3−C15	86.7(9)
N1−Fe1−N19		C1−Fe2−N5	88.4(9)	C13−Fe3−N13	90.5(10)
N1−Fe1−N22		C1−Fe2−N7	95.0(9)	C13−Fe3−N15	178.0(9)
N2^{i} −Fe1−N10		C1−Fe2−N9	175.8(8)	C13−Fe3−N17	178.0(9)
N2^{i}−Fe1−N11^{i}		C2−Fe2−N5	89.4(8)	C14−Fe3−N13	94.6(8)
N2^{i}−Fe1−N19		C2−Fe2−N7	177.6(8)	C14−Fe3−N15	176.9(8)
N2^{i}−Fe1−N22		C2−Fe2−N9	92.2(8)	C14−Fe3−N17	91.1(7)
N10−Fe1−N11^{i}		C3−Fe2−N5	177.1(8)	C15−Fe3−N13	178.7(8)
N10−Fe1−N19		C3−Fe2−N7	94.5(8)	C15−Fe3−N15	90.6(8)
N10−Fe1−N22		C3−Fe2−N9	92.5(9)	C15−Fe3−N17	91.9(10)
N11^{i}−Fe1−N19		N5−Fe2−N7	88.2(7)	N13−Fe3−N15	88.1(7)
N11^{i}−Fe1−N22		N5−Fe2−N9	88.8(7)	N13−Fe3−N17	87.9(8)
N19−Fe1−N22		N7−Fe2−N9	87.9(7)	N15−Fe3−N17	90.5(7)

Symmetric operate with code i: *x, 3/2− y, 1/2 + z*

With temperature decreasing to 100 K, the average Fe−N distance for Fe(II) shortened to 1.98 Å, typical feature for low-spin Fe(II). The Fe−C and Fe−N bond lengths for Fe(III) centers locate in the range of 1.84−1.94 Å and 1.93−2.01 Å, which are nearly the same with these measured at high temperature. The bond change with temperature variation indicates that the Fe(II) ions in the double-zigzag chain show spin transition from high-spin to low-spin.

Single-crystal measured at 123K reveals that complex **3-2** crystallized in a triclinic space group $P\bar{1}$ (Table 3.4). The molecular structure of complex **3-2** can be described as a trinuclear $Fe^{III}_2Fe^{II}$ unit with extend one-dimensional (1D) structure linked by the ligand btb in the Fe(II) site (Figure 3.2). Within the trinuclear unit, two $Fe^{III}(Tp)(CN)_3]^-$ entities bridged to the Fe(II) center through one of three CN group in each $Fe^{III}(Tp)(CN)_3]^-$ entity, and these two CN nitrogen atoms occupied two axial position of the Fe(II) center. Four N atoms from four btb ligands coordinated with the Fe(II) center in the equatorial positions, and the other terminal N atoms in the btb ligands coordinated to two adjacent Fe(II) centers in the same style, forming extend 1D structure along the *a*-axis.

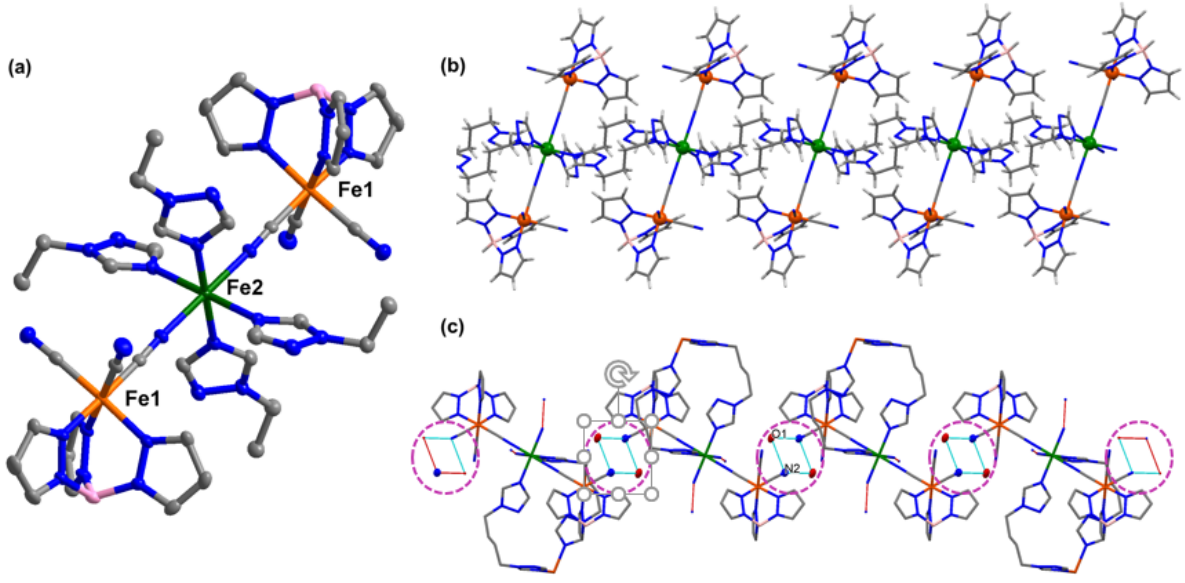

Figure 3.2. Crystal structure of complex **3-2**: (a) structure of the trinuclear $Fe^{III}_2Fe^{II}$ unit in **3-2**; (b) 1D structure bridged by coordination ligands (btb); (c) Hydrogen-bonds (in the purple cycles) formed between terminal CN group and lattice water molecules.

Table 3.4. Crystallographic parameters of complex **3-2**.

Compound	**3-2**
Formula	$C_{40}H_{48}B_2Fe_3N_{30}O_2$
Formula weight	1170.1671
Temp. (K)	123 K
Crystal System	triclinic
Space group	$P\bar{1}$ (No. 2)
a (Å)	9.5343(19)
b (Å)	11.625(2)
c (Å)	12.972(3)
α (°)	81.01(3)
β (°)	76.41(3)
γ (°)	66.72(3)
Volume (Å^3)	1280.5(6)
Z	1
$\rho_{calcd.}$(g cm^{-3})	1.455
μ (Mo-$K\alpha$)	0.906
F(000)	554
θ range (°)	1.619–27.485
Reflections	3991
R_1 ($I > 2.0\sigma$)	0.0557
wR_2 (*all data*)	0.1389
Goodness-of-fit on F^2	0.999

[a] $R = \sum||F_0|-|F_c||)/\sum|F_0|$ [b] $wR = |\sum w(F_0-F_c)^2/\sum w(F_0^2)^2|^{1/2}$

Table 3.5. Selected bond distances (Å) and angles (°) for complex **3-2**.

Fe(II)		Fe(III)	
Fe2−N1	2.171(3)	Fe1−C1	1.929(4)
Fe2−N1^{i}	2.171(3)	Fe1−C2	1.931(4)
Fe2−N10	2.205(3)	Fe1−C3	1.912(4)
Fe2−N10^{i}	2.205(3)	Fe1−N4	1.965(3)
Fe2−N13	2.192(3)	Fe1−N6	1.986(3)
Fe2−N13^{i}	2.192(3)	Fe1−N8	1.972(3)
N1−Fe2−N1^{i}	180.0	C1−Fe1−C2	86.70(16)
N1−Fe2−N10	90.31(12)	C1−Fe1−C3	86.70(16)
N1−Fe2−N10^{i}	90.31(12)	C2−Fe1−C3	88.55(18)
N1−Fe2−N13	91.25(12)	C1−Fe1−N4	92.98(15)
N1−Fe2−N13^{i}	88.75(12)	C1−Fe1−N6	94.32(15)
N1^{i}–Fe2−N10^{i}	89.69(12)	C1−Fe1−N8	177.71(15)
N1^{i}–Fe2−N10	89.69(12)	C2−Fe1−N4	90.61(16)
N1^{i}–Fe2−N13^{i}	91.25(12)	C2−Fe1−N6	177.55(15)
N1^{i}–Fe2−N13	88.75(12)	C2−Fe1−N8	90.45(15)
N10−Fe2−N10^{i}	180.0	C3−Fe1−N4	179.12(16)
N10−Fe2−N13	88.15(12)	C3−Fe1−N6	92.11(16)
N10−Fe2−N13^{i}	91.85(12)	C3−Fe1−N8	91.51(15)
N10^{i}–Fe2−N13	91.85(12)	N4−Fe1−N6	88.74(14)
N10^{i}–Fe2−N13^{i}	88.15(12)	N4−Fe1−N8	88.79(13)
N13−Fe2−N13^{i}	180.0	N6−Fe1−N8	87.17(13)

Symmetric operate with code i: *x, 3/2− y, 1/2 + z*

The same with $Fe^{III}(TP)(CN)_3]^-$ entities in **3-1**, the Fe(III) ion in **3-2** is also coordinated by three N atoms from the Tp ligand with Fe−N_{Tp} bonds lengths in the range of 1.965(3) −1.986(3) Å, and three C atoms from three CN^- groups with the Fe−C bonds ranging from 1.912(4) Å to 1.931(4). The Fe−N_{CN} bond lengths are 2.171(3) Å, and Fe−N_{btb} bond lengths are 2.192(3) Å and 2.192(3) Å, which indicates that the Fe(II) ions in complex **3-2** are in high-spin state. The lattice water molecules formed hydrogen-bonds (O−H···N with the terminal CN groups with the O···N distances of 2.866 and 2.969 Å, which link the 1D chains forming a two-dimensional (2D) extended structure.

3.3.3 Magnetic Properties

Temperature-dependent magnetic susceptibility for compound **3-1** was collected in the temperature range of 2−280 K under an applied magnetic field of 2000 Oe (Figure 3.3). The $\chi_m T$ value is 4.78 cm^3 K mol^{-1} at 280 K, obviously larger than the spin only value (3.75 cm^3 K mol^{-1}) for a basic magnetic unit containing isolated two low-spin Fe(III) (S = 1/2) ions and one high-spin Fe(II) (S = 2) ion due to the existence of orbital contribution of the metal ions. Upon lowering the temperature, the $\chi_m T$ value maintains almost no change until to around 200 K. After that, the $\chi_m T$ value sharply decreases to 1.23 cm^3 K mol^{-1} at about 70 K, and then keeps almost constant with further decreasing temperature. The $\chi_m T$ value in low temperature range is corresponding to two isolated low-spin Fe(III) with spin-

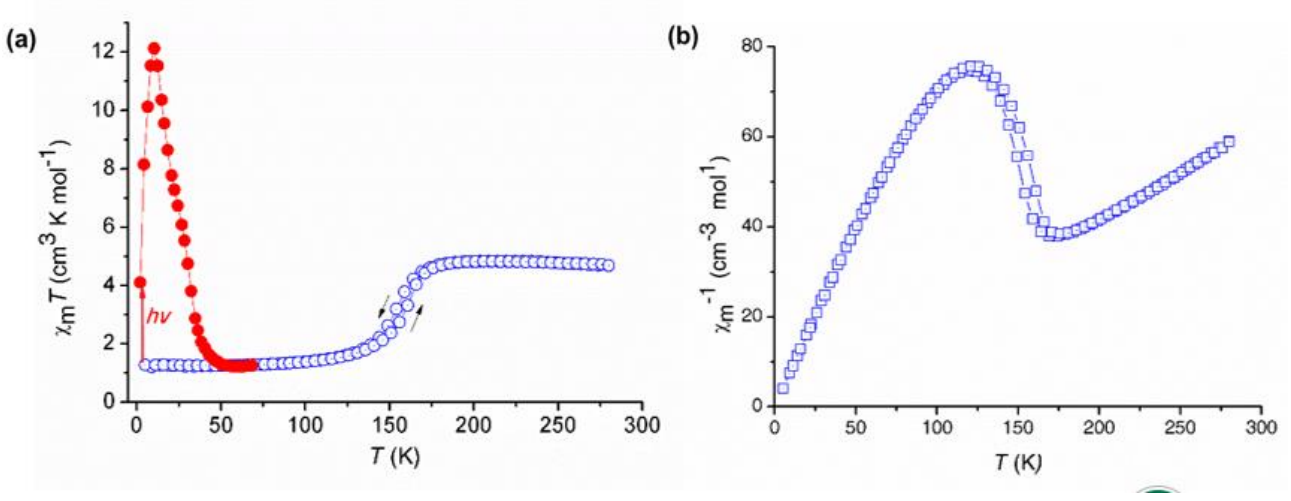

Figure 3.3. Temperature dependence of $\chi_m T$ (a) and χ_m^{-1} (b) for **3-1** measured in the temperature range of 2-280 K under 2000 Oe in one reversal cycle.

orbital contributions, which suggests that the abrupt magnetic susceptibility decrease was caused by complete spin transition of Fe(II) ion from high-spin (S = 2) to low-spin (S = 0). One the heating process, the $\chi_m T$ exhibits a reversal increase to the initial value with a small thermal hysteresis loop of 7 K.

The spin transition on the Fe(II) sites in complex **3-1** can also be induced by light. At low temperature, the $\chi_m T$ value can be induced from 1.21 cm^3 K mol^{-1} to a much larger value of 12.2 cm^3 K mol^{-1} by red light irradiation. The $\chi_m T$ value for the light-excited state is also obviously large that that for that measured at 280 K, which suggests the presence of magnetic interaction between Fe(III) and Fe(II) centers. After light switching off, the photo reached large $\chi_m T$ value shows an abrupt decrease with temperature, and relaxes back to its initial value at about 50 K, indicating that the photo-induced spin transition is revisable.

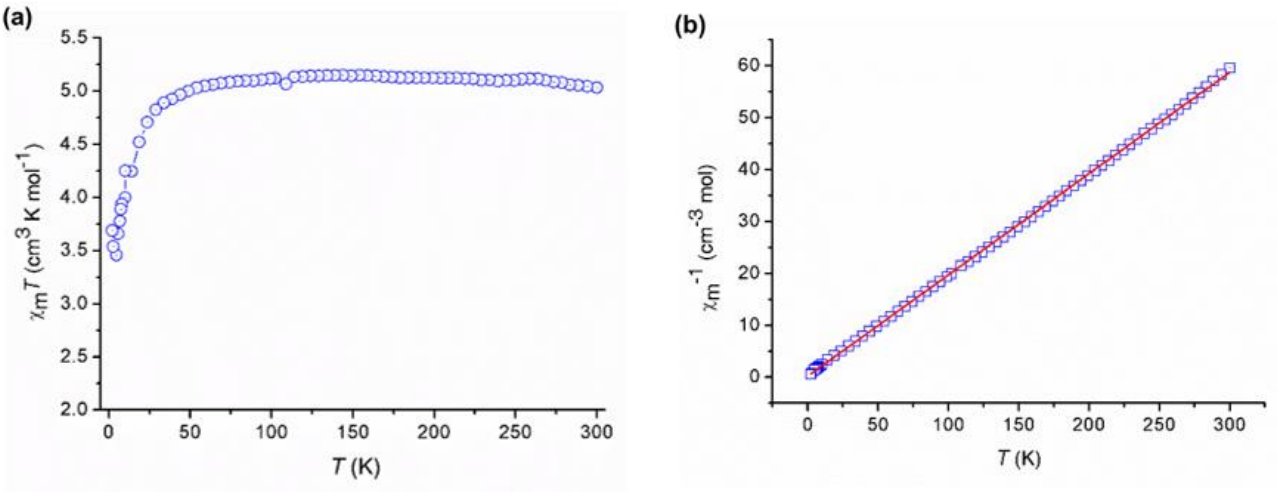

Figure 3.4. Temperature dependence of $\chi_m T$ (a) and χ_m^{-1} (b) for **3-2** measured in the temperature range of 2-300 K under a dc magnetic field of 2000 Oe.

Temperature dependence of magnetic susceptibility for compound **3-2** was measured in the temperature range of 2−300 K under an applied magnetic field of 2000 Oe (Figure 3.4). At around room temperature the $\chi_m T$ value is 5.0 cm^3 K mol^{-1}, which is common for a trinuclear complex with two low-spin Fe(III) and one high-spin Fe(II). With measure temperature declining, the $\chi_m T$ value

keeps nearly unchanged until about 60 K. After that, the $\chi_m T$ value abruptly decreases to 3.4 cm^3 K mol^{-1} at 2 K. The $\chi_m T$ vs T curve for complex **3-2** suggests the absence of electronic dynamic behavior in this complex and the existence of weak antiferromagnetic interactions between Fe(III) and Fe(II) centers. The χ_m^{-1} vs T plot well obeys the Curie-Weiss law ($\chi_m^{-1} = T/C - \theta/C$) with a Curie constant C = 5.13 cm^3 K mol^{-1} and Weiss constant W = –0.92 K. The negative and small value also indicates that the magnetic coupling interaction between Fe(III) and Fe(II) in 2-2 is weak antiferromagnetic.

3.3.2 Mössbauer Spectra Analysis

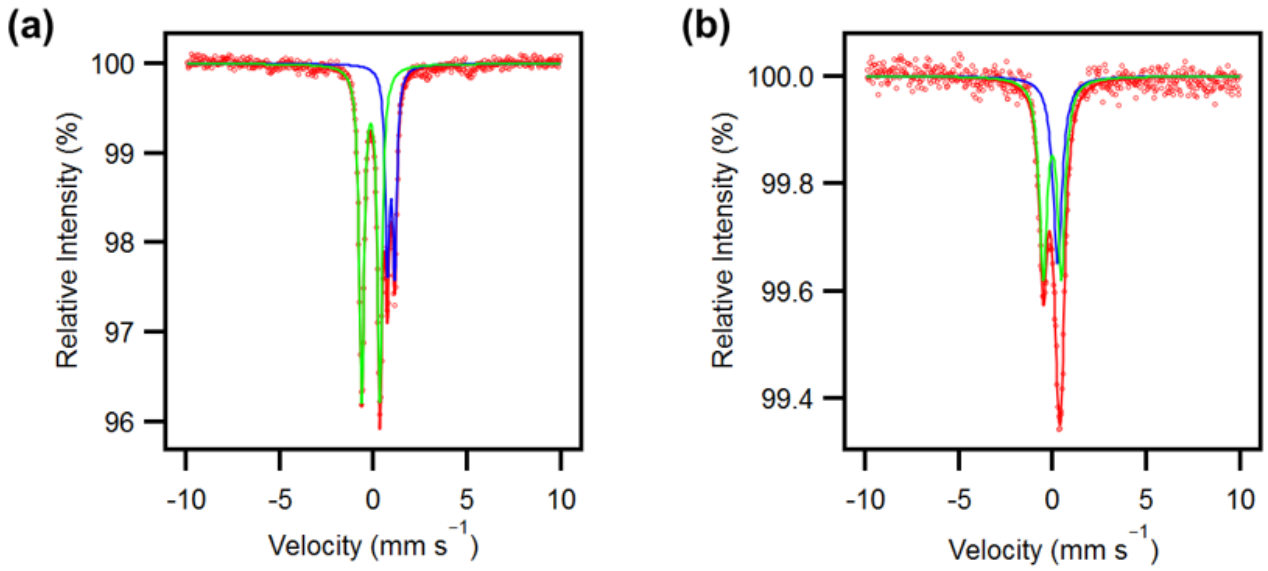

Figure 3.5. Mössbauer spectra recorded at 293 K (a) and 16.5 K for **3-1**. The solid lines stand for Lorentzian curves plotted according to calculation value.

It is well known that Mössbauer spectra analysis is a powerful technique for determining the oxidation and spin states of Fe ions. To further confirm that the magnetic dynamic behavior of complex **3-1** was generated via spin transition of Fe(II) ions in the double-zigzag chain, Mössbauer spectra were measured before (293 K, Figure 3.5a) and after (16.5 K, Figure 3.5 b) magnetic transition. The Mössbauer spectrum recorded at 293 K features a quadruple doublet with Mössbauer parameters of δ (isomer shift) = 0.92 mms^{-1} and ΔE_Q (quadruple splitting) = 0.38 mms^{-1}, and another quadruple doublet with Mössbauer parameters of δ = –0.17 mms^{-1} and ΔE_Q = 0.97 mms^{-1}. The former

quadruple doublet is typical characterization of high-spin Fe(II) ion, whereas the latter one reveals the existence of low-spin Fe(III) in compound **3-1**. Additionally, the peak area ratio (Fe(II) : Fe(III)) of these two quadruple doublets is 0.35 : 0.65, which agrees well with the result of structural analysis. As the temperature lowered down to 16.5 K, the quadruple doublet for high-spin Fe(II) was replaced by a singlet for low-spin Fe(II) with Mössbauer parameters of $\delta = 0.24$ mms^{-1} and $\Delta E_Q = 0.60$ mms^{-1}, while the quadruple doublet for low-spin Fe(III) with Mössbauer parameters of $\delta = -0.04$ mms^{-1} and $\Delta E_Q = 0.97$ mms^{-1} maintains almost the same as that for high temperature phase. The peak area ratio in low temperature also indicates that the Fe(II) to Fe(III) is 1 : 2, confirming that the complete spin transition of Fe(II) from high-spin to low-spin for compound **3-1**.

2.3.4 Optical Spectrum Analyses

The spin transition behavior of Fe(II) ions in the double-zigzag chain of **3-1** was also supported by temperature dependent ultraviolet–visible–near infrared absorption (UV/Vis-NIR) spectra and infrared (IR) absorption spectra. When the spin state of Fe(II) centers change from high-spin state to low-spin state, the absorption peak at 435 nm in the UV/Vis-NIR spectra that belongs to metal-to-ligand charge transfer (MLCT) band nearly unchanged, whereas the absorption peak at around 1200 nm relating to intervalence charge transfer between Fe(II) ion and Fe(III) ion band enhanced (Figure 3.6a).

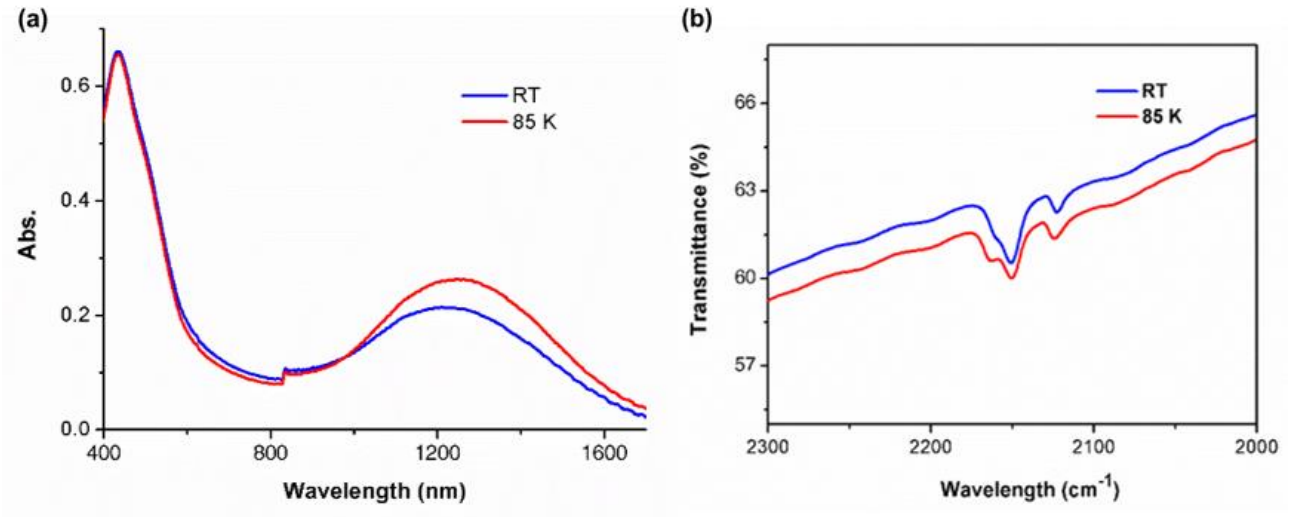

Figure 3.6. Temperature dependence of UV/Vis-NIR (a) and IR spectra (b) for compound **3-1**.

To check whether electron transfer occurred or not with temperature variation, variable-temperature IR spectra were conducted at room temperature (RT) and 85 K, At room temperature, the IR spectrum characterizes two vibrating absorption peaks at 2150 and 2123 cm^{-1} for bridge and terminal CN^- groups, respectively. These IR absorption peaks are typical feature for the Fe^{III}–CN, which remains almost unchanged in the spectrum recorded at 85 K, suggesting the absence of Fe^{II}–CN (IR absorption peaks below 2100 cm^{-1}) in the magnetic dynamic process of compound **3-1**. The optical spectra variation of complex **3-1** is similar to other cyanide-bridged Fe^{II}/Fe^{III} mixed-valence compounds with spin transition occurred on the Fe(II) sites.[24, 25]

3.3.5 Ligand Effects on Spin Number variation for Fe^{II}/Fe^{III} mixed-valence system

As mentioned in the introduction part, there are three possible electronic dynamic processes, including spin transition, charge transfer and charge transfer coupled spin transition, for a system with different active metal centers linked by cyanide groups. Certainly, these electronic dynamic processes can also occur in the cyanide-bridged Fe^{II}/Fe^{III} system. To the best of my knowledge, the magnetic dynamic behaviors of the cyanide-bridged Fe^{II}/Fe^{III} compounds are mainly resulted from spin transition of the Fe(II) sites. There is only one example of this system with magnetic variation caused via charge transfer mechanism between the Fe(II) and the Fe(III) centers. Additionally, CTCST behavior has not been observed yet in cyanide-bridged Fe^{II}/Fe^{III} compound. In the $\{Fe^{III}_2Fe^{II}\}_n$ double-zigzag chains system, ST and MMCT behaviors have been respectively observed in different compounds by our group. Therefore, the possible influences, such as composition and structure, on the electronic dynamic processes of the cyanide-bridged Fe^{II}/Fe^{III} system is discussed herein based on these $\{Fe^{III}_2Fe^{II}\}_n$ double-zigzag chains, which may provide available information for realizing CTCST in this system. It is well known that the electronic dynamic behavior in a system containing two active metal ions is determined by various factors, such as the redox-potential of the two metal sites, bridge ligands, ligand field strength, coordination geometries, packing mode, and intermolecular interactions. In the cyanide-bridged $\{Fe^{III}_2Fe^{II}\}_n$ mixed-valence double-zigzag chains,

complexes **3-1** and $\{[Fe^{III}(Tp^*)(CN)_3]_2Fe^{II}(bpmh)\}\cdot 2H_2O$ exhibit thermal induced ST behavior,[25] whereas complex $\{[Fe(Tp)(CN)_3]_2Fe(bpe)\cdot 5H_2O\}_n$ manifests temperature-dependent MMCT behavior.[27] Another $\{Fe^{III}_2Fe^{II}\}_n$ double-zigzag chain $\{[Fe(Tp)(CN)_3]_2Fe(CH_3OH)\cdot H_2O\}_n$ with CH_3OH coordinated in the Fe(II) sites remains electronic state unchanged in the temperature of 2-300K.[45]

The thermal induced electronic dynamics undoubtedly influenced by the coordination ligands. The σ-donor or π-acceptor ability of the coordination ligands sensitively adjusts the ligand field strength and redox potentials of the metal centers. As for the cyanoferrates, Tp* possesses two methyl groups in each pyrazole group, and that has richer electron density, which leads to more negative $Fe^{II/III}$ redox couples ($E_{1/2}$ = –0.94 V vs Fc^+/Fc for $[Fe^{III}(Tp^*)(CN)_3]^-$ and $E_{1/2}$ = –0.79 V for $[Fe^{III}(Tp)(CN)_3]^-$).[13]

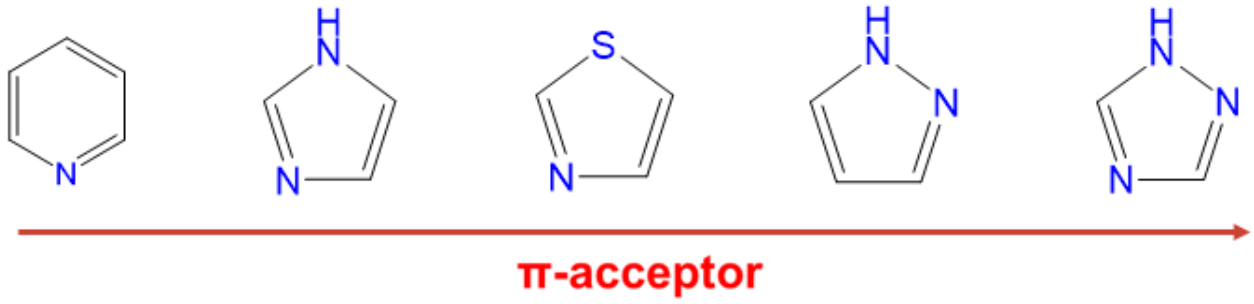

Scheme 3.3. the order of increasing σ-donor interaction and declining of π-acceptor ability for some nitrogen donor ligands .

As for the ancillary ligands on the Fe(II) sites, 1,2,4-triazole has much weak σ-donor ability and stronger π-acceptor interaction than these for pyridine. Among the above three cyanide-bridged $\{Fe^{III}_2Fe^{II}\}_n$ mixed-valence double-zigzag chains, both compounds **3-1** and $\{[Fe^{III}(Tp^*)(CN)_3]_2Fe^{II}(bpmh)\}\cdot 2H_2O$ exhibit ST behavior on the Fe(II) sites, which indicating that both 1, 2, 4-triazole and pyridine combined with four CN groups provide suitable ligand field strength to generate spin-crossover behavior for Fe(II) center. Complexes **3-1** and $\{[Fe(Tp)(CN)_3]_2Fe(bpe)\cdot 5H_2O\}_n$ have the same Fe(III) sites ($[Fe^{III}(Tp)(CN)_3]^-$), but the Fe(II) sites

coordinated by 1,2,4-triazole and pyridine, respectively. While complexes $\{[Fe(Tp)(CN)_3]_2Fe(bpe)\cdot 5H_2O\}_n$ and $\{[Fe^{III}(Tp^*)(CN)_3]_2Fe^{II}(bpmh)\}\cdot 2H_2O$ possess similar Fe(II) sites but different in Fe(III) sites. The MMCT behavior only observed in compound $\{[Fe(Tp)(CN)_3]_2Fe(bpe)\cdot 5H_2O\}_n$, which may be explained by the HSAB (Hard Soft Acid Base) Principles. According to HSAB Principles, hard bases (ligands) are prone to stable hard acids (metals), while soft bases favors soft acids. In addition, a higher oxidation state generally leads to the transition metal harder. For some nitrogen donor ligands, the order of increasing σ-donor interaction and declining of π-acceptor ability follows the order below:[46]

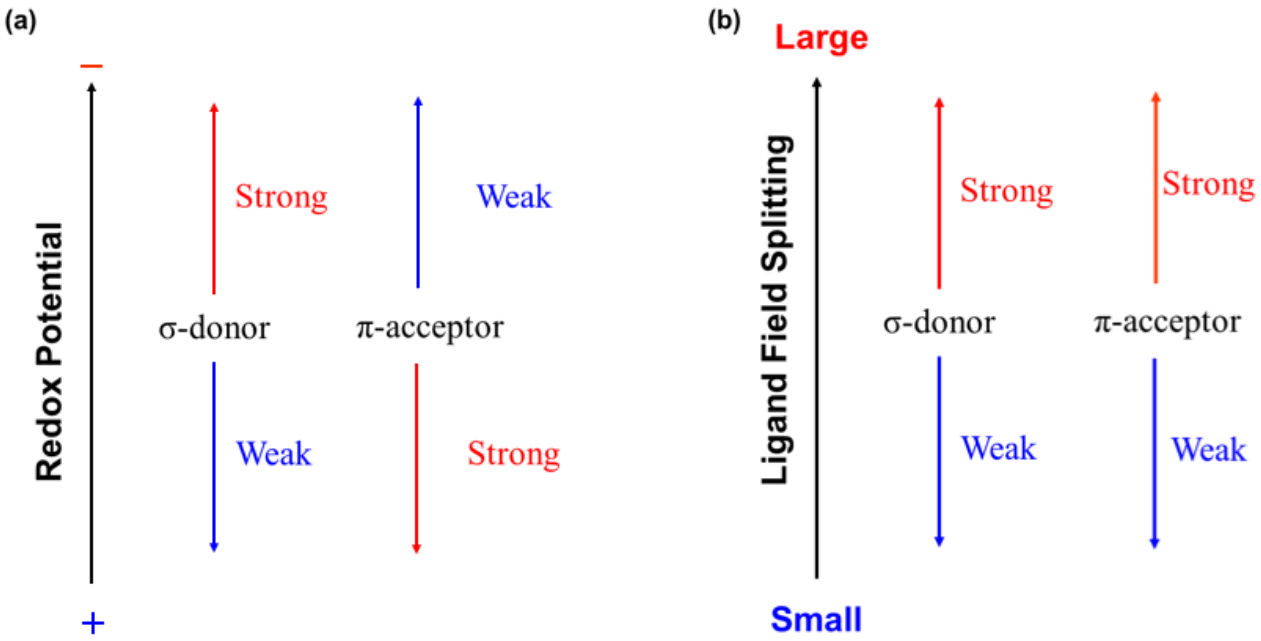

Scheme 3.4.Relationship between magnitude of ligand-field splitting/redox potential of metal center and σ-donor and π-acceptor.

Compound $\{[Fe(Tp)(CN)_3]_2Fe(bpe)\cdot 5H_2O\}_n$ exhibits MMCT behavior due to that the Fe(III) and Fe(II) sites feature close redox potential, and the relatively hard bpe (pyridine) ligand can stabilize the relatively harder Fe(III) center. The absence of MMCT behavior in complexes **3-1** and $\{[Fe^{III}(Tp^*)(CN)_3]_2Fe^{II}(bpmh)\}\cdot 2H_2O$ may be related to that the relatively large separation between Fe(II) and Fe(III) sites. Additionally, the btb (triazole) may be too soft to stabilize the Fe(III) ion. The

lock of ST behavior in complex $\{[Fe(Tp)(CN)_3]_2Fe(bpe)\cdot 5H_2O\}_n$ with CT process may be ascribe to that the ligand field of bpe on Fe(III) sites is not strong enough. The reason that complex $\{[Fe(Tp)(CN)_3]_2Fe(CH_3OH)\cdot H_2O\}_n$ does not show any electronic dynamic may be due to that CH_3OH only possesses weak σ-donor interaction without suitable ligand field and redox potential for Fe(II) sites to exihit ST or CT behavior. Scheme 2.4 presents the correlation of ligand-field splitting/redox potential magnitude and σ-donor and π-acceptor ability. To observe combined the MMCT and ST behavior, namely CTCST behavior in cyanide-bridged Fe^{II}/Fe^{III} system, the nitrogen donor ligands with σ-donor interaction and declining of π-acceptor ability between triazole and pyridine may be a possible candidates. The absence of ST behavior in complex **3-2** is related to that the ligand filed strength of 1,2,4-triazole is weak than that of cyanide group since cyanide group has stronger π-acceptor interaction.

3. 4 Conclusion

In this chapter, a new cyanide-bridged $\{Fe^{III}_2Fe^{II}\}_n$ double-zigzag chain and a new trinuclear cyanide-bridged $Fe^{III}_2Fe^{II}$ compound have been synthesized via carefully selecting starting building block and coordination ligand, and reaction conditions. The $\{Fe^{III}_2Fe^{II}\}_n$ double-zigzag chain exhibits magnetic bistablity via the spin transition behavior on the Fe(II) sites, whereas the trinuclear $Fe^{III}_2Fe^{II}$ cluster maintains its electronic state unchanged in the temperature range of 2-300 K, suggesting the lock of magnetic bistable state in this complex. It should be noted that these two complexes contain the same cyanoferrate and ligand but feature distinct molecular structures and magnetic properties, which indicates that flexible ligands are sensitive to the reaction conditions thus can be used to adjust molecular structures and magnetic properties.

As for Fe^{III}/Fe^{II} mixed valence systems, magnetic bistablity can be achieved through several different electronic dynamics, therefore, the correlation of magnetic properties and coordination ligands has been carefully discussed in this chapter. The ability of σ-donor and π-acceptor of the

ligands deeply influences the redox potential and ligand field splitting of the metal ions. In the family of cyanide-bridged $\{Fe^{III}_2Fe^{II}\}_n$ mixed-valence double-zigzag chains, ancillary ligands with stronger σ-donor generally lead to more negative redox potential for the metal center, whereas ancillary ligands with stronger π-acceptor interaction can enhance the ligand filed splitting for the metal ions. However, the σ-donor ability and π-acceptor ability for organic ligands usually varies in opposite direction. Therefore, to realize magnetic bistability through new electronic dynamic manner, namely charge-transfer coupled spin-transition (CTCST), in Fe^{III}/Fe^{II} mixed valence compound should balance the σ-donor ability and π-acceptor ability of the coordination ligands.

References

(1) O. Sato, T. Tyoda, T. Fujishima, K. Hashimoto, *Science*, **1996**, *272*, 704–705.

(2) M. A. Halcrow, *Spin-Crossover Materials*. John Wiley & Sons, United Kingdom, **2013**.

(3) X.-Y. Wang, C. Avendaño, K. R. Dunbar, *Chem. Soc. Rev.* **2011**, *40*, 3213–3238.

(4) M. Ohba, H. Ōkawa, *Coord. Chem. Rev.* **2000**, *198*, 313–323.

(5) D. Pinkowicz, R. Podgajny, B. Nowicka, S. Chorazy, M. Reczyński, B. Sieklucka, *Inorg. Chem. Front.* **2015**, *2*, 10–27.

(6) C. P. Berlinguette, A. Dragulescu-Andrasi, A. Sieber, J. R. Galán-Mascarós, H.-U. Güdel, C. Achim, K. R. Dunbar, *J. Am. Chem. Soc.* **2004**, *126*, 6222–6223.

(7) C. P. Berlinguette, A. Dragulescu-Andrasi, A. Sieber, H.-U. Güdel, C. Achim, K. R. Dunbar, *J. Am. Chem. Soc.* **2005**, *127,* 6766–6779.

(8) D. Li, R. Clérac, O. Roubeau, E. Harté, C. Mathonière, R. L. Bris, S. M. Holmes, *J. Am. Chem. Soc.* **2008**, *130,* 252–258.

(9) N. Hoshino, F. Iijima, G. N. Newton, N. Yoshida, T. Shiga, H. Nojiri, A.Nakao, R. Kumai, Y. Murakami H. Oshio. *Nat. Chem.* **2012**, *4*, 921–926.

(10) C. Zheng, J. Xu, Z. Yang, J. Tao, D. Li. *Inorg. Chem.,* **2015**, *54*, 9687-9689.

(11) D. Garnier, R.Jiménez, Y.Li, J. von Bardeleben, Y.Journaux, T. Augenstein, E. Moos, M. T. Gamer, F. Breher, R. Lescouëzec. *Chem. Sci.* **2016**, 4825–4831.

(12) Y. Zhang, D. Li, R. Clérac, M. Kalisz, C. Mathonière, S. M. Holmes. *Angew. Chem. Int. Ed.* **2010**, *49*, 3752–3756.

(13) Y.- Z. Zhang, P. Ferko, D. Siretanu, R. Ababei, N. P. Rath, M. J. Shaw, R. Clérac, C. Mathonière, S. M. Holmes. *J. Am. Chem. Soc.* **2014**, *136*, 16854–64.

(14) M. Nihei, Y. Sekine, N. Suganami, K. Nakazawa, A. Nakao, H. Nakao, Y. Murakami, H. Oshio. *J. Am. Chem. Soc.* **2011***, 133*, 3592–3600.

(15) E. S. Koumousi, I. R. Jeon, Q. Gao, P. Dechambenoit, D. N. Woodruff, P. Merzeau. *J. Am. Chem.*

Soc. **2014**, *136*, 15461–15464.

(16) N. Masayuki, O. Yuki, S. Yoshihiro, H. Norihisa, S. Takuya, I. P. -C. Liu, H. Oshio. *Angew. Chem. Int. Ed.* **2012**, *51*, 6361–6364.

(17) T. Liu, D.- P. Dong, S. Kanegawa, S. Kang, O. Sato, Y. Shiota, K. Yoshizawa, S. Hayami, S. Wu, C. He, and C. Y. Duan. *Angew. Chem. Int. Ed.* **2012**, *51*, 4367–4370.

(18) A. Mondal, Y. Li, M. Seuleiman, M. Julve, L. Toupet, C. M. Buron-Le, R. Lescouëzec. *J. Am. Chem. Soc.* **2013**, *135*, 1653–1656.

(19) D. Siretanu, D. Li, L. Buisson, D.M. Bassani, S.M. Holmes, C. Mathonière, R. Clérac. *Chem. Eur. J.* **2011**, *17*, 11704–11708.

(20) J. Mercurol, Y. Li, E. Pardo, O. Risset, M. Seuleiman, H. Rousselière, R. Lescouëzec, M. Julveb. *Chem. Comm.* **2010**, *46*, 8995–8997.

(21) C. Avendano, M. G. Hilfiger, A. Prosvirin, C. Sanders, D. Stepien, K. R. Dunbar, *J. Am. Chem. Soc.* **2010**, *132*, 13123–13125.

(22) M. Nihei, M. Ui, H. Oshio, *Polyhedron*, **2009**, *28*, 1718–1721.

(23) G. N. Newton, M. Nihei, H. Oshio, E. J. *Inorg. Chem.* **2011**, 3031–3042.

(24) C. Zheng, J. Xu, F. Wang, J. Tao, D. Li, *Dalton Trans.* **2016**,*45*, 17254–17263.

(25) T. Liu, H. Zheng, S. Kang, Y. Shiota, S. Hayami, M. Mito, O. Sato, K. Yoshizawa, S. Kanegawa C. Duan, *Nat. Commun.* 2013, *4*, 2826.

(26) A. Mondal, Y. Li, P. Herson, M. Seuleiman, M.-L. Boillot, E. Rivière, M. Julve, L. Rechignat, A. Bousseksoud, R. Lescouëzec, *Chem. Commun.* **2012**,*48*, 5653–5655.

(27) K. Zhang, S. Kang, Z.-S. Yao, K. Nakamura, T. Yamamoto, Y. Einaga, N. Azuma, Y. Miyazaki, M. Nakano, S. Kanegawa, O. Sato, *Angew. Chem.* **2016***, 128,* 6151 –6154.

(28) S. Chorazy et al., *Chem. Commun.* **2014**, *50*, 3484–3487.

(29) M. G. Hilfiger, M. Chen, T. V. Brinzari, T. M. Nocera, M. Shatruk, D. T. Petasis, J. L. Musfeldt, C. Achim, K. R. Dunbar, *Angew. Chem. Int. Ed.* **2010**, 49, 1410–1423.

(30) R. Le Bris, Y. Tsunobuchi, C. MathoniÀre, H. Tokoro, S. Ohkoshi, N. Ould-Moussa, G. Molnar, A. Bousseksou, J. F. L¦tard, *Inorg. Chem.* **2012**, *51*, 2852–2859.

(31) S. Ohkoshi, S. Ikeda, T. Hozumi, T. Kashiwagi, K. Hashimoto, *J. Am. Chem. Soc.* **2006**, *128*, 5320–5321.

(32) H. Tokoro, S. Ohkoshi, T. Matsuda, K. Hashimoto, *Inorg. Chem.* **2004**, *43*, 5231–5236.

(33) S. I. Ohkoshi, T. Matsuda, H. Tokoro, K. Hashimoto, *Chem. Mater.* **2005**, *17*, 81–84.

(34) H. Tokoro, S. Ohkoshi, *Bull. Chem. Soc. Jpn.* 2015, 88, 227–239.

(35) C. Avendano, M. G. Hilfiger, A. Prosvirin, C. Sanders, D. Stepien, K. R. Dunbar, *J. Am. Chem. Soc.* **2010**, *132*, 13123–13125.

(36) S. Ohkoshi, N. Machida, Y. Abe, Z. J. Zhong and K. Hashimoto, *Chem. Lett.*, **2001**, 312–313.

(37) J. Long, L. M. Chamoreau, C. Mathonière and V. Marvaud, *Inorg. Chem.* **2009**, *48*, 22–24.

(38) C. Maxim, C. Mathonière and M. Andruh, *Dalton Trans.* **2009**, 7805–7810.

(39) T. Hozumi, K. Hashimoto and S. Ohkoshi, *J. Am. Chem. Soc.* **2005**, *127*, 3864–3869.

(40) J. M. Herrera, V. Marvaud, M. Verdaguer, J. Marrot, M. Kalisz and C. Mathonière, *Angew. Chem., Int. Ed.* **2004**, *43*, 5468–5471.

(41) R. Podgajny, S. Chorazy, W. Nitek, M. Rams, A. M. Majcher, B. Marszalek, J. Zukrowski, C. Kapusta, B. Sieklucka, *Angew. Chem. Int. Ed.* **2013**, *52*, 896–900.

(42) R. Lescouëzec, J. Vaissermann, F. Loret, M. Julve, M. Verdaguer, *Inorg. Chem.* **2002**, *41*, 5943–5945.

(43) V. N. Kizhnyaev, E. A. Krakhotkina, T. L. Petrova, M. V. Kazantseva, F. A. Pokatilov, O. N. Verkhozina, *Polym. Sci. Ser.* B **2011** *53*, 144–150.

(44) G. M. Sheldrick, *Acta Cryst. C* **2015**, 71, 3–8.

(45) D. Zhang, Z. Li, N. Yu, Z. Yang, Q. Yang, Y. Wu, D. Li, *J. Mol. Struct.* **2015**, *1083*, 194–197.

(46) M. A. Trojer, A. Movahedi, H. Blank, M. Nydén, *J. Chem.* **2013**, 946739.

Chapter 4. Polymorphic Structures and Water-Tunable Thermal Hysteresis in a Dinuclear Co Valence Tautomeric Complex

4. 1 Introduction

The rapid development of electronic memory devices has motivated the investigation of molecules possessing switchable magnetic bistability.[1-3] Valence tautomeric (VT) complexes, whose magnetic properties change upon a change in the redox state, have received considerable attention in recent decades.[4-31] The most useful aspect of these magnetic properties is their abrupt change with a considerable thermal hysteresis loop at around room temperature (RT) and the retention of their photo-magnetism at temperatures close to RT. Recently, studies on spin transition compounds have found that some of these desirable magnetic properties are strongly related to their intermolecular interactions.[32-40] However, the "pure" correlation between the VT transition and intermolecular factors is still uncertain due to the very limitation examples and absence of clear packing structures for VT polymorphic compounds.[21, 26] Clarifying this correlation would facilitate the further exploration of VT compounds, but remains very challenging. Additionally, the control of hysteretic transitions is a significant but challenging task in magnetic bistable systems,[41-46] including the VT family. More significantly, the direction of charge transfer between metal center and redox-active ligand may be controlled via reasonable chemical design and adjustion of molecular parking.

A tetraoxolene-bridged binuclear cobalt compound with tpa (tpa = tris(2-pyridylmethyl)amine) terminal ligands is a typical VT complex manifesting a VT transition between the [*ls*-Co^{3+}–$dhbq^{3-}$–*ls*-Co3+]3+ and [*ls*-Co^{3+}–$dhbq^{2-}$–*ls*-Co^{2+}]$^{3+}$ states (ls, low-spin; hs, high-spin; dhbq = deprotonated 2,5-dihydroxy-1,4-benzoquinone).[8] The VT transition resulted in an abrupt change in the magnetic properties with a thermal hysteresis loop at approximately RT, making it a promising memory material.[1] However, the magnetic susceptibility of the high-temperature phase did not reach the

theoretically expected value after the abrupt transition.[8] Our recent careful investigation reveals that the incomplete transition initially considered as an intrinsic property in the complex is due to the presence of two polymorphic forms of the complex. Furthermore, through exploring the synthetic conditions, it is found that the two forms can be separately synthesized by controlling the crystallization temperature. This finding provides a good opportunity for the investigation on the "pure" contribution of intermolecular factors to the VT behaviors as this system consists a Co complex adopting two different crystal-packing structures. Here, we describe the synthesis, structure and properties of the two polymorphic complexes, including water-adjustable thermal hysteretic transition behavior observed for one of these polymorphs at approximately RT.

Scheme 4.1 Polymorphic structures determined by recrystallization temperature for a dinuclear Co valence tautomeric complex.

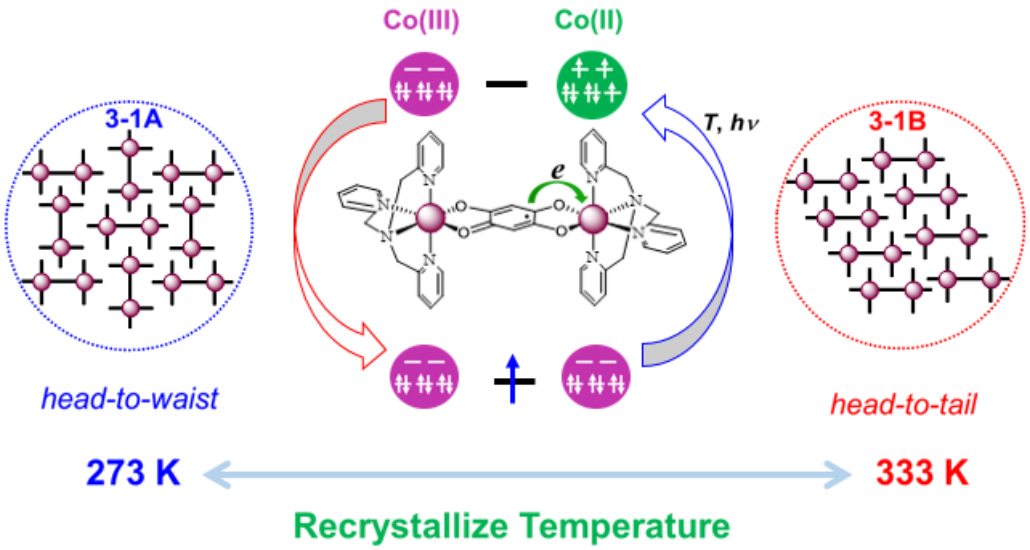

4. 2 Experimental Section

4.2.1 Starting Materials and Synthesis Methods

All of chemical reagents were commercially obtained and directly used. An initial sample of the title complex [{Co(tpa)$_2$}(dhbq)](PF$_6$)$_3$ (**4-1**) was prepared following the previously reported

procedure.[8]

Synthesis of [{Co(tpa)$_2$}(dhbq)](PF$_6$)$_2$. A methanol solution (10 ml) of 2,5-di-hydroxyl-1,4-benzoquinone (H_2dhbq, 0.14 g, 1.0 mmol) was slowly added to a methanol solution (20 ml) of tris(2-pyridylmethy)amine (0.58 g, 2.0 mmol) and $CoCl_2 \cdot 6H_2O$ (0.48 g, 2.0 mmol) under stirring. The resulting mixture was heated to reflux, after then an aqueous solution of KPF_6 (0.73 g, 4.0 mmol) was added. [{Co(tpa)$_2$}(dhbq)](PF$_6$)$_2$ was obtained as red microcrystals, which was collected via filtration and washed alternately with water and methanol for several times, and them dried under vacuum. Yield: ca. 35%.

Synthesis of [{Co(tpa)$_2$}(dhbq)](PF$_6$)$_3$ (4-1).An acetone/water mixed solution (v/v = 1/1, 5 ml) of $AgPF_6$ (25.3 mg, 0.1 mmol) was added dropwise into a acetone solvent (10 ml) of [{Co(tpa)}$_2$(dhbq)](PF6)$_2$ (112.6 mg, 0.1 mmol), the resulting mixture was stirred at room temperature for 30 min. After that, the precipitation was removed by filtration and the solvent was removed by reduced pressure evaporation, the red residue was washed with cooled water for several times, and dried under in air. Yield: ca. 85 %.

Synthesis of (4-1A·3H$_2$O). An acetone/water mixed solution (v/v = 2:1, 10 ml) of [{Co(tpa)}$_2$(dhbq)](PF6)$_3$ (**4-1**) was slowly evaporated in a ice/water bath (0–4 °C) under nitrogen atmosphere. Long parallelepiped dark red crystals of **4-1A·3H$_2$O** can be obtained after several days. The target product was collected through filtration and then dried in air. Yield: ca. 60 %. Anal. Calcd for $C_{42}H_{44}Co_2F_{18}N_8O_7P_3$: C 38.05, H 3.34, N 8.45 %; found: C 38.49, H 3.32, N 8.42 %.

Synthesis of (4-1B·2H$_2$O). An acetone/water mixed solution (v/v 1:2, 10 ml) of **4-1** was evaporated in an oil bath (60–65 °C) under nitrogen atmosphere. Long needle dark red crystals of **4-1B·2H$_2$O** can be obtained after several hours, which was collected by filtration and air-dried. Yield: ca. 45 %. Anal. Calcd for $C_{42}H_{42}Co_2F_{18}N_8O_6P_3$: C 38.58, H 3.24, N 8.57 %; found: C 38.87, H 3.11, N 8.67 %.

4.2.2 Physical Measurement

Crystal structural analysis. The crystal data of **4-1A·3H$_2$O** (200 K), **4-1A** (300 K), **4-1B·2H$_2$O** (123 K) and **4-1B** (123 and 333 K) were collected on a Rigaku FR-E+ CCD diffractometer with Mo-Kα radiation. All the structures were solved via direct method and refined by the full-matrix least-squares technique on F^2 by on the SHELXTL program.[47] All H atoms on C atoms were geometrically produced and refined using a riding model. While H atoms on lattice water can be found from difference Fourier maps, for which O-H distance were normalized to 0.82 Å. Structural information of **4-1A·3H$_2$O** (1498385), **4-1A** (1498386), **4-1B·2H$_2$O** (1498387) and **4-1B** (1498388/1498389) can be obtained freely from the Cambridge Crystallographic Data Centre (CCDC).

Other physical measurement. The powder X-ray diffraction (PXRD) patterns were obtained on a Rigaku 2100 diffractometer with Cu-*Kα* radiation using flat plate geometry. Magnetic measurements were performed on a Quantum Design MPMS-XL SQUID magnetometer. Light-irradiation of the samples was carried out with a laser diode pumped Nd:YAG laser (532 nm). The UV-vis absorption spectra for solid sample were recorded in the range 400–800 nm on a UV-3100 PC spectrometer, and UV-vis absorption spectra for solution sample were measured in the range 400–800 nm on a DH-2000-BAL spectrometer. Infrared (IR) spectra (CaF_2 pellet) were recorded in the range 1000–4000 cm^{-1} on a JASCO FT/IR-600 Plus spectrometer. Thermogravimetric analysis (TGA) were performed on a TG/DTA6300 system at a temperature-increasing rate of 2 K/min. Differential scanning calorimetry (DSC) measurement were carried out on a DSC 6200. Elemental analyses were conducted on a Yanaco CHN CORDER MT-6 elemental analyzer.

Computational methods. The Mulliken charges and spin densities for the cation $[\{Co(tpa)_2\}(dhbq)]^{3+}$ in **4-1B** at 123 K and 333 K were calculated using density functional theory (DFT) on the program Package Gaussian 09.[48] The X-ray determined molecular structures were used for the calculation. B3LYP*/6-311+G** basis sets were used through all calculation.[49]

4. 3 Results and Discussion

4.3.1 Structural Analysis

Crystal structure data for polymorph **4-1A·3H₂O** were obtained at 200 K. Structural analysis revealed that the crystal structure of **4-1A·3H₂O** is almost the same as that previously reported,[8] comprising the orthorhombic space group *P*ccn (Table 4.1) with molecular cations $[\{Co(tpa)_2\}(dhbq)]^{3+}$ ($\mathbf{1^{3+}}$) located at the crystallographic center of symmetry (Figure 4.1). The average Co–N and Co–O bond lengths are 1.919 Å and 1.887 Å, and the C–O bond lengths are 1.335 Å and 1.316 Å (Table 4.2). These bond lengths reveal that the spin and oxidation state for the molecular cation ($\mathbf{1^{3+}}$) of this polymorphic phase can be expressed as radical form [*ls*-Co^{3+}–$dhbq^{3-}$–*ls*-Co^{3+}]$^{3+}$ at 200 K. The lattice water molecules formed hydrogen bonds between themselves and have almost no efficient intermolecular interaction with the host molecules. The dehydrated crystal measured at 300 K shows almost the same structure as those of the fresh crystal (Table 4.1 and 4.2).

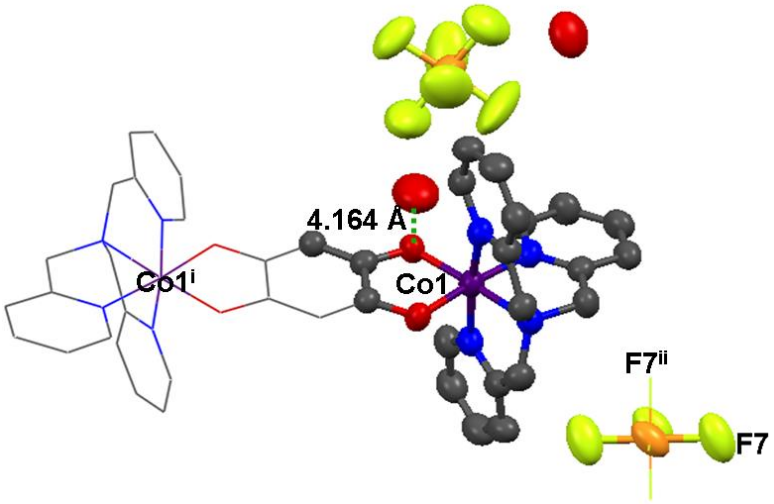

Figure 4.1. Ellipsoid mode showing asymmetric structural unit of polymorph **4-1A·3H₂O** (*ls*-Co^{3+}, C, O, N, P and F atoms are represented by violet, grey, red, orange, and yellow ellipsoids, respectively. H atoms were omitted for clarity; the wireframe mode part was generated by symmetric operations with code i: *-x, 1-y, 1-z*; ii: *3/2-x, 1/2-y, z*).

Table 4.1. Crystallographic parameters of complexes **4-1A·3H₂O** and **4-1A**.

Compound	**4-1A· 3H₂O**	**4-1A**
Formula	$C_{42}H_{44}Co_2F_{18}N_8O_7P_3$	$C_{42}H_{38}Co_2F_{18}N_8O_4P_3$
Formula weight	1325.57	1271.58
Temp. (K)	200	300
Crystal System	Orthorhombic	Orthorhombic
Space group	*Pccn* (No. 56)	*Pccn* (No. 56)
a (Å)	16.368(3)	16.078(3)
b (Å)	20.091(4)	20.331(4)
c (Å)	16.047(3)	16.593(3)
α (°)	90	90
β (°)	90	90
γ (°)	90	90
Volume (Å^3)	5277(17)	5406.3(19)
Z	4	4
$\rho_{calcd.}$(g cm^{-3})	1.633	1.562
μ (Mo-$K\alpha$)	0.840	0.812
F(000)	2532.0	2556.0
θ range (°)	3.004–27.476	2.990–24.996
Independent reflections	2885	2996
R_1 ($I > 2.0\sigma$)	0.0765	0.1057
wR_2 (*all data*)	0.2363	0.3373
Goodness-of-fit on F^2	1.008	1.186

[a] $R = \sum||F_0|-|F_c||)/\sum|F_0|$ [b] $w\mathrm{R} = |\sum w(F_0-F_c)^2/\sum w(F_0^2)^2|^{1/2}$

Table 3.2. Selected bond distances (Å) and angels (°) for complexes **4-1A·3H₂O** and **4-1A**.

	4-1A·3H₂O (200 K)		**4-1A** (300 K)	
Co–O	1.876(3)	1.879(3)	1.879(4)	1.892(4)
Co–N	1.902(4)	1.911(4)	1.921(6)	1.937(6)
	1.904(4)	1.923(4)	1.934(6)	1.953(6)
C–O	1.317(5)	1.325(6)	1.310(7)	1.319(7)
O–Co–O	87.16(14)		87.08(18)	

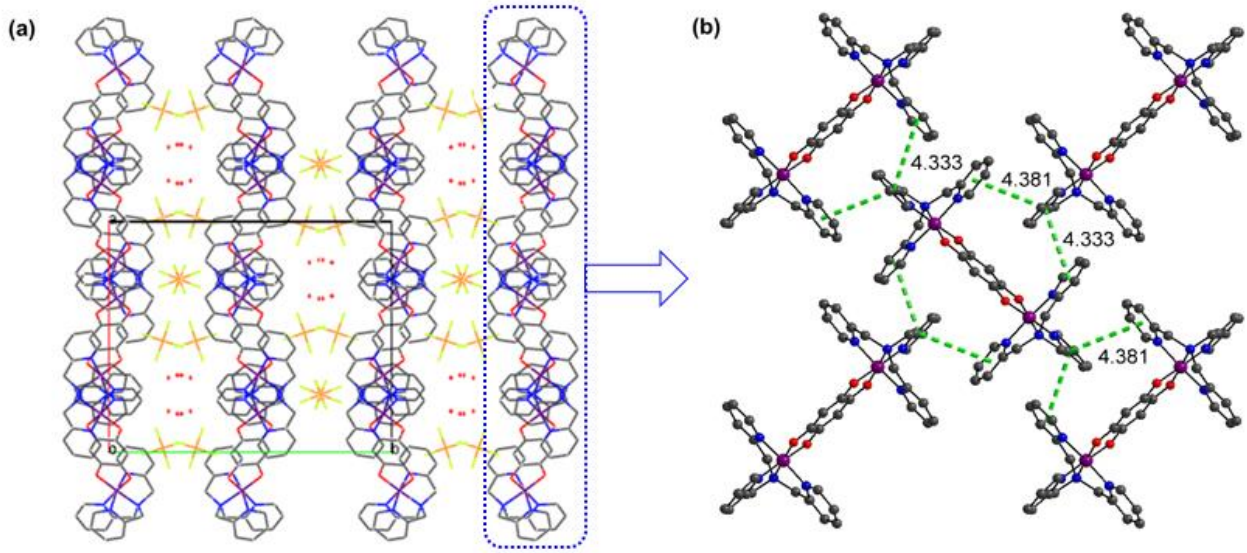

Figure 4.2. (a) Crystal packing mode for polymorph **4-1A·3H₂O** showing alternating cation and anion layers; (b) Arrangement mode of $\mathbf{1}^{3+}$ cations in the same layer for polymorph **4-1A·3H₂O** (**4-1A**) with π···π interactions (green dotted lines) shown. (*ls*-Co^{3+}, C, O, N, P and F atoms are represented by violet, grey, red, orange and yellow, H atoms were omitted for clarity).

In the crystal state, **4-1A·3H₂O** (**3-1A**) features $\mathbf{1}^{3+}$ cations and PF_6^- anions crystallized in alternating layers forming three-dimensional structure (Figure 4.2a). In the cation layers, the $\mathbf{1}^{3+}$ cations are arranged *head-to-waist* with their neighbors (Figure 4.2b), and the head pyridines are located almost equidistant between the adjacent cations, forming relatively uniform and very weak

intermolecular π···π interactions with the pyridine pairs centroid···centroid distances of 4.510 Å and 4.199 Å for **4-1A·3H₂O**, and 4.381 Å and 4.333 Å for **4-1A**. The lattice water molecules are located in the holes formed by the $\mathbf{1}^{3+}$ cations and PF_6^- anions. Thermogravimetric analysis (TGA) showed that the lattice water can be easily removed since the TGA curve shows that lattice water are almost completely lost at approximately 355 K (Figure 4.3a). Additionally, the purity of this polymeric phase has been confirmed by powder X-ray diffraction (Figure 4.3b)

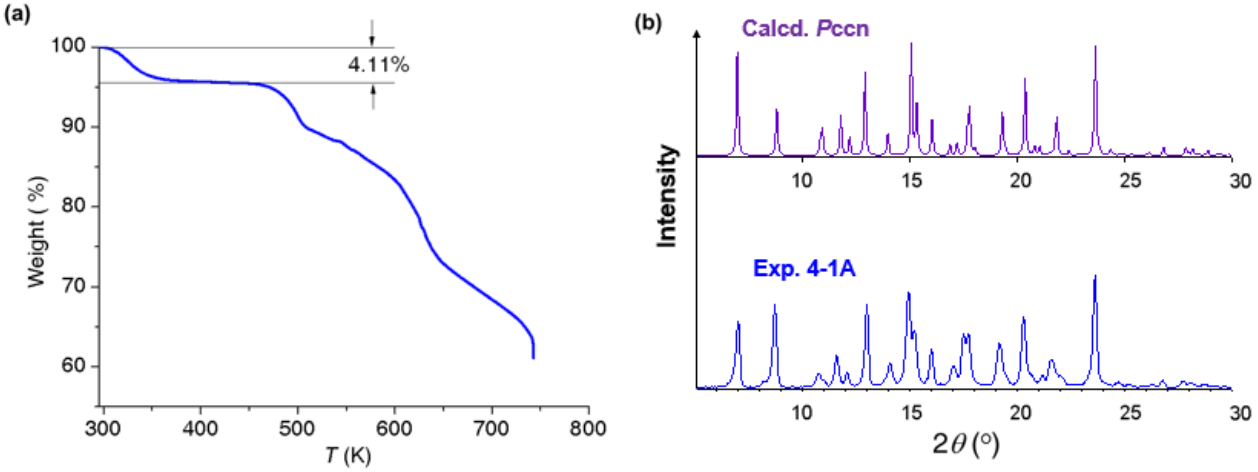

Figure 4.3. (a) TGA curve and (b) PXRD pattern (room temperature) for polymorph **4-1A·3H₂O**.

Structural analysis of **4-1B·2H₂O** at 123 K and 333 K indicated that this polymorph exhibits a thermal phase transition. At 123 K, **4-1B·2H₂O** crystallizes into a triclinic space group $P\bar{1}$ (Table 4.3) with two independent $\mathbf{1}^{3+}$ cations located at the crystallographic center of symmetry (Figure 4.4a). At 333 K, **4-1B** (lattice water molecules lost during the measurement) adopts a monoclinic space group $P_{21/c}$ (Table 4.3), with the $\mathbf{1}^{3+}$ cations absent from the crystallographic inversion center (Figure 3.4b). At 123 K, the average coordination bond distances for **4-1B·2H₂O** are 1.922 Å (Co–N) and 1.883 Å (Co–O) for Co1 and 1.925 Å (Co–N) and 1.881 Å (Co–O) for Co2 (Table 3.4), indicating that the spin and oxidation state for the molecular cation of this polymorphic phase are radical form, which can be presented as $[ls\text{-}Co^{3+}\text{–}dhbq^{3-}\text{–}ls\text{-}Co^{3+}]^{3+}$ at 123 K. After the phase transition, the molecular conformation is very different (Table 3.4), with the average metal-to-ligand bond lengths becoming

1.916 Å (Co–N) and 1.878 Å (Co–O) for Co1, and 2.104 Å (Co–N) and 2.072 Å (Co–O) for Co2. The C–O bond distances also decrease from 1.317–1.322 Å at 123 K to 1.248–1.295 Å at 333 K. These bonds revealed that one electron transfers from the radical $dhbq^{3-}$ to one of Co ion, which simultaneously changed from *ls*-Co^{3+} to *hs*-Co^{2+}. Thus, the oxidation and spin state of $\mathbf{1}^{3+}$ at 333 K can be expressed as [*ls*-Co^{3+}–$dhbq^{2-}$–*hs*-Co^{2+}]$^{3+}$. In the fresh crystals, these lattice water molecules formed very weak hydrogen bonds with the oxygen atoms of the cations (Figure 4.4a). The crystal structure of **4-1B** at 333 K does not include any lattice water (Figure 4.4 b), indicating that dehydration occurred during the measurement. The dehydrated crystal measured at 123 K possesses almost the same structural features as those of the fresh crystal (Table 4.3 and 4.4). The valence tautomeric transition induced a non-polar-to-polar structure change. The Mulliken charges and spin densities for the cation for $\mathbf{1}^{3+}$ before and after valence tautomeric transition have been determined by DFT calculation (Figure 4.5), which indicates that the $\mathbf{1}^{3+}$ possesses an electric dipole moment of 0 Debye in [*ls*-Co^{3+}–$dhbq^{3-}$–*ls*-Co^{3+}]$^{3+}$ form and 9.724 Debye in [*ls*-Co^{3+}–$dhbq^{2-}$–*hs*-Co^{2+}]$^{3+}$ form.

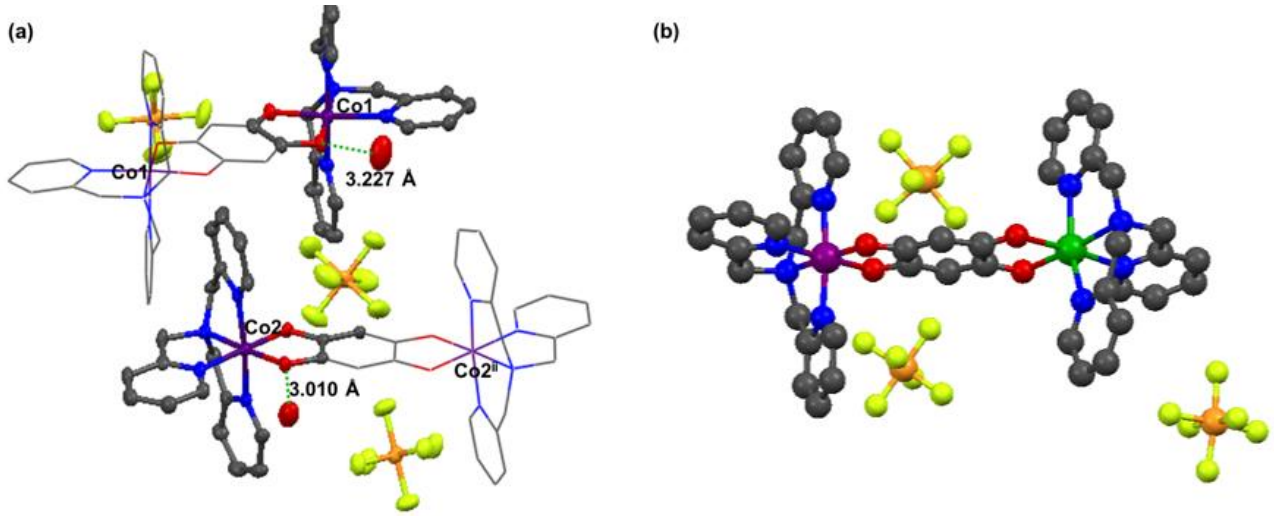

Figure 4.4. Ellipsoid mode showing asymmetric structural unit of **4-1B·2H₂O** at 123 K (a) and **4-1B** at 333 K (b). (*ls*-Co^{3+}, *hs*-Co^{2+}, C, O, N, P and F atoms are represented by violet, green, grey, red, orange and yellow, H atoms were omitted for clarity, wireframe mode part was generated by symmetric operations with code i: *1-x, 1-y, -z*; ii: *1-x, 1-y, 1- z*).

Table 4.3. Crystallographic parameters of complexes **4-1B·2H₂O** and **4-1B**.

Compound	**4-1B·2H₂O** (LT)	**4-1B**(HT)	**4-1B**(HT)
Formula	$C_{42}H_{42}Co_2F_{18}N_8O_6P_3$	$C_{42}H_{38}Co_2F_{18}N_8O_4P_3$	$C_{42}H_{38}Co_2F_{18}N_8O_4P_3$
Formula weight	1307.59	1271.58	1271.58
Temp. (K)	123 K	333 K	123 K
Crystal System	triclinic	monoclinic	triclinic
Space group	$P\bar{1}$ (No. 2)	$P2_1/c$ (No. 14)	$P\bar{1}$ (No. 2)
a (Å)	11.928(2)	17.465(4)	11.702(2)
b (Å)	12.532(3)	17.980(4)	12.608(3)
c (Å)	17.872(4)	17.881(4)	17.910(4)
α (°)	103.90(3)	90	103.83(3)
β (°)	103.76(3)	112.85(3)	105.17(3)
γ (°)	96.59(3)	90	96.22(3)
Volume (Å^3)	2476.7(10)	5174(2)	2434.7(10)
Z	2	4	2
$\rho_{calcd.}$(g cm^{-3})	1.753	1.632	1.734
μ (Mo-$K\alpha$)	0.891	0.848	0.901
F(000)	1318.0	2556.0	1278.0
θ range (°)	3.295–25.499	3.185–25.250	3.279–25.499
Reflections	7881	7712	7130
R_1 ($I > 2.0\sigma$)	0.0561	0.1116	0.0819
wR_2 (*all data*)	0.1306	0.2244	0.1967
Goodness-of-fit on F^2	1.054	1.166	1.050

[a] $R = \sum||F_0|-|F_c||)/\sum|F_0|$ [b] $wR = |\sum w(F_0-F_c)^2/\sum w(F_0^2)^2|^{1/2}$

Table 4.4. Selected bond distances (Å) and angels (°) for complexes **4-1B·2H₂O** and **4-1B**.

	3-1B·2H₂O (123 K)		**3-1B** (333 K)		**3-1B**(123 K)	
Co–O	1.879(3)	1.877(3)	1.877(4)	2.020(4)	1.867(4)	1.867(4)
	1.887(3)	1.884(2)	1.879(4)	2.125(5)	1.883(5)	1.877(4)
Co–N	1.912(3)	1.914(3)	1.899(5)	2.069(7)	1.902(5)	1.901(5)
	1.919(3)	1.925(3)	1.912(6)	2.095(7)	1.916(5)	1.918(5)
	1.921(3)	1.926(3)	1.928(5)	2.118(7)	1.924(5)	1.920(5)
	1.935(3)	1.933(3)	1.928(6)	2.135(6)	1.938(5)	1.937(5)
C–O	1.318(4)	1.322(4)	1.248(7)	1.288(7)	1.320(7)	1.331(7)
	1.322(4)	1.317(4)	1.277(7)	1.295(7)	1.328(7)	1.321(7)
O–Co–O	87.39(11)	87.64(11)	86.01(18)	78.93(18)	87.93(19)	88.12(19)

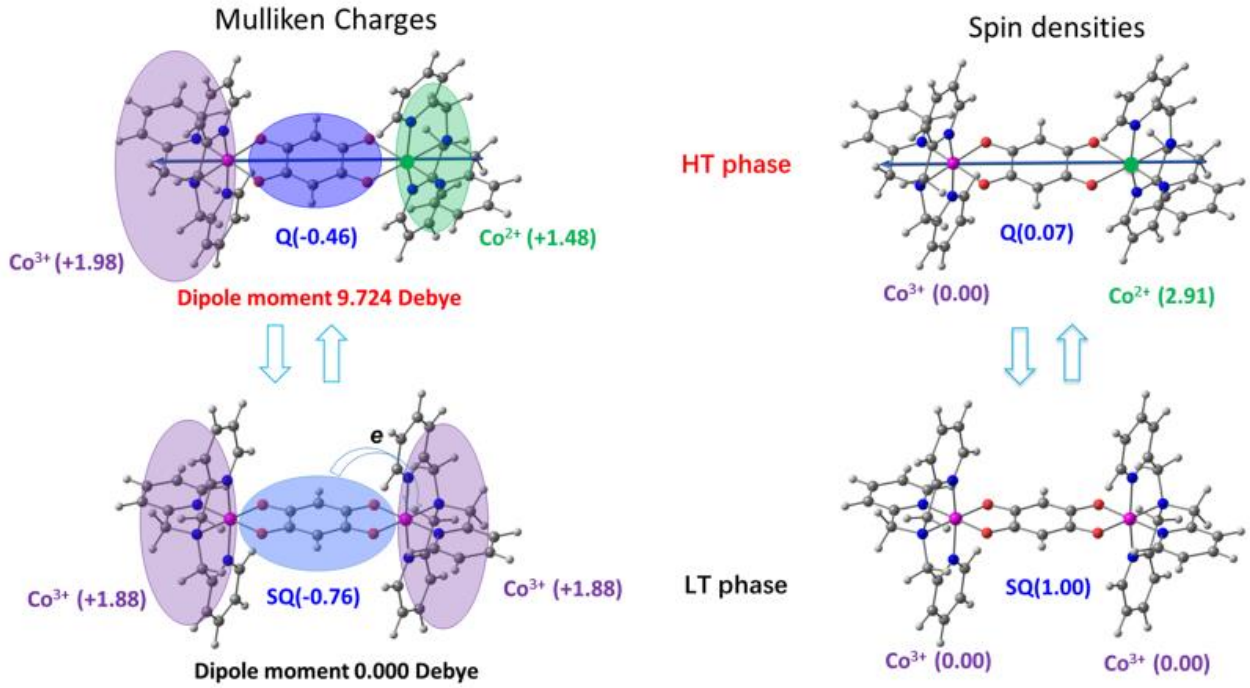

Figure 4.5. The Mulliken charges and spin densities distribution for $\mathbf{1}^{3+}$ cation of **4-1B** in high temperature phase and low temperature phase.

Polymorph **4-1B**·2H_2O (**4-1B**) also features alternating layers of $\mathbf{1}^{3+}$ cations and PF_6^- anions in the three-dimensional extended structure (Figure 4.6a). The arrangement of $\mathbf{1}^{3+}$ cations is very different from that in polymorph **4-1A**. In the cation layers of **4-1B**·2H_2O (**3-1B**), the $\mathbf{1}^{3+}$ cations adopt a *head-to-tail* arrangement with their neighbors (Figure 4.6b). This arrangement, which is different from that of polymorph **4-1A**, certainly results in different π···π intermolecular interactions. In this polymorph phases, the head and tail pyridine pairs also show weak π···π interactions, with centroid···centroid distances of 4.161 Å and 4.162 Å for **4-1B**·2H_2O, 4.117 Å and 4.111 Å for **4-1B**. While the shoulder pyridines of tpa are offset from the waists of adjacent molecules, forming relatively strong π···π interactions (3.866 Å for **4-1B** and 3.730 Å for **4-1B**·2H_2O of the pyridine pairs). The π···π interactions become weak after the phase transition (Figure 4.7a). The lattice water molecules are located in the PF_6^- anion layers (Figure S8) in **4-1B**·2H_2O. TGA data reveal that the lattice water is abruptly lost at approximately 325 K (Figure 4.8a), which is in accordance with the structure data collected at 333 K. The purity of this polymorphic phase was checked by PXRD (Figure 4.8b).

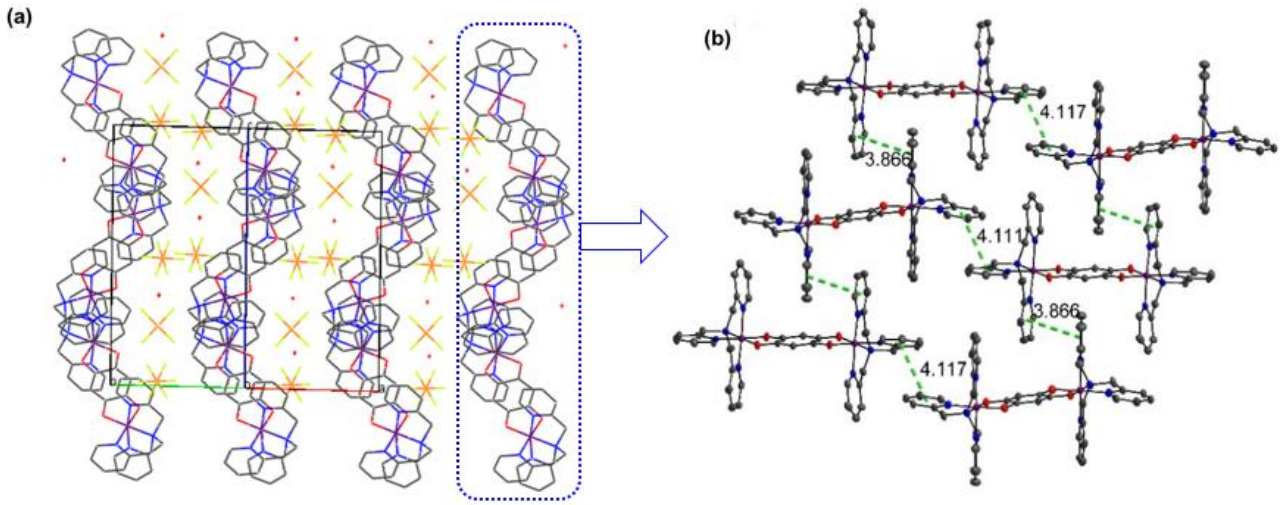

Figure 4.6. (a) Crystal packing mode for polymorph **4-1B·2H_2O** showing alternating cation and anion layers; (b) Arrangement mode of $\mathbf{1}^{3+}$ cations in the same layer for polymorph **4-1B·2H_2O** (**4-1B**) with π···π interactions (green dotted lines) shown (*ls*-Co^{3+}, C, O, N, P and F atoms are represented by violet, grey, red, orange and yellow, H atoms were omitted for clarity).

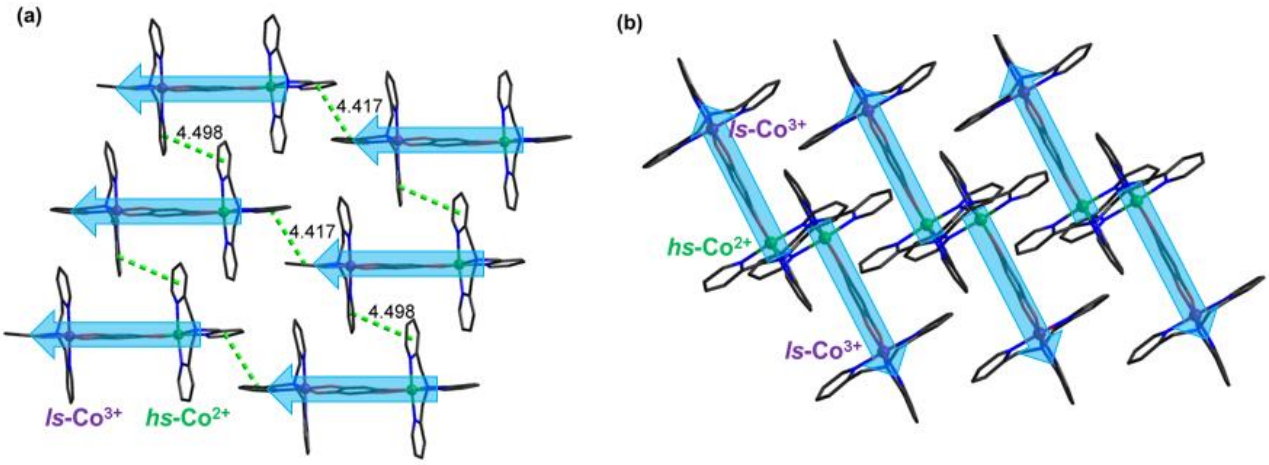

Figure 4.7. Arrangement mode of $\mathbf{1}^{3+}$ cations showing the same polar directions in one layer (a), while adverse polar directions in two adjacent layers (b) for polymorph **4-1B**.

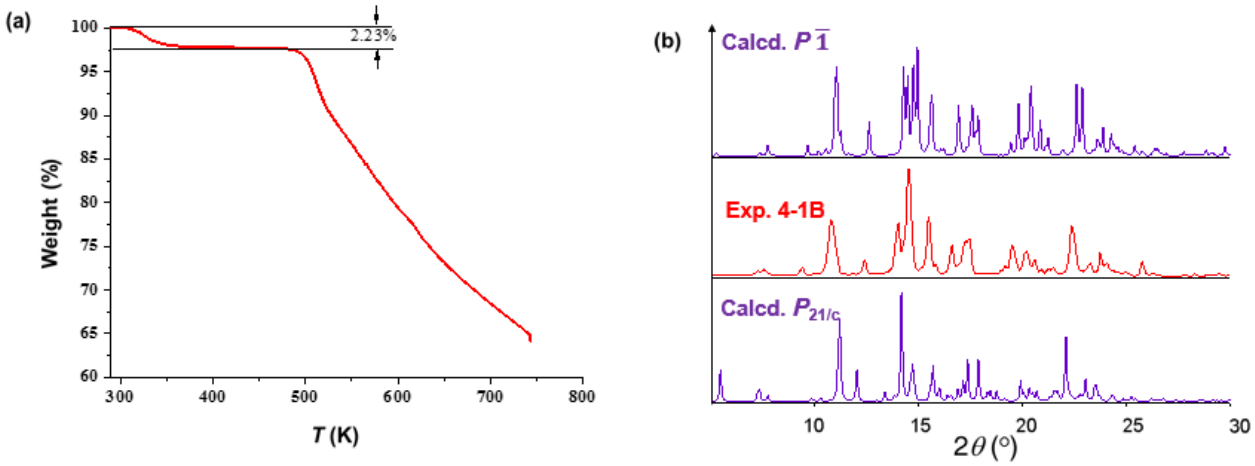

Figure 3.8. (a) TGA curve and (b) PXRD pattern (room temperature) for polymorph **4-1B·2H₂O**.

As mentioned forward, the $\mathbf{1}^{3+}$ cations exhibit nonpolar-to-polar structural transition accompanying with the valence tautomeric behavior. The crystal-packing mode of **4-1B** at 333 K reveals that $\mathbf{1}^{3+}$ cations shown unidirectional charge transfer between the cobalt ions and dhbq ligands in the same layer (Figures 4.7a), namely that the polar orientation of $\mathbf{1}^{3+}$ cations in one layer are almost the same. This is a promising characteristic for generating interesting electronic properties for this polymorph. Unfortunately, the charge transfer behavior in adjacent layers is adverse (Figures 4.7b). Further effort to synthesize similar valence tautomeric complexes showing unidirectional charge transfer extended to three-dimensional structures is in progress.

4.3.2 Magnetic Properties

Magnetic analysis revealed that these two polymorphic complexes exhibit distinct thermally dependent VT behaviors (Figure 4.9a). For polymorph **4-1A·3H₂O**, $\chi_m T$ (where $\chi_m T$ stands for the molar magnetic susceptibility) remains almost constant at 0.36 cm^3 K mol^{-1} from 2 to 270 K, which is in accordance with the oxidation and spin state of [*ls*-Co^{3+}–$dhbq^{3-}$–*ls*-Co^{3+}]$^{3+}$ (S = 1/2). Then, $\chi_m T$ slowly increases to 1.10 cm^3 K mol^{-1} at 360 K, indicating an incomplete VT transition in this polymorphic phase. According to the TGA data, the sample would dehydrate during the magnetic measurement. However, the dehydrated sample (**4-1A**) has the same magnetic properties with **4-1A·3H₂O**, which agrees well with the near absence of an efficient interaction between the water molecules and $\mathbf{1}^{3+}$ cations (Figure 4.1) found in the structural analysis of this polymorph.

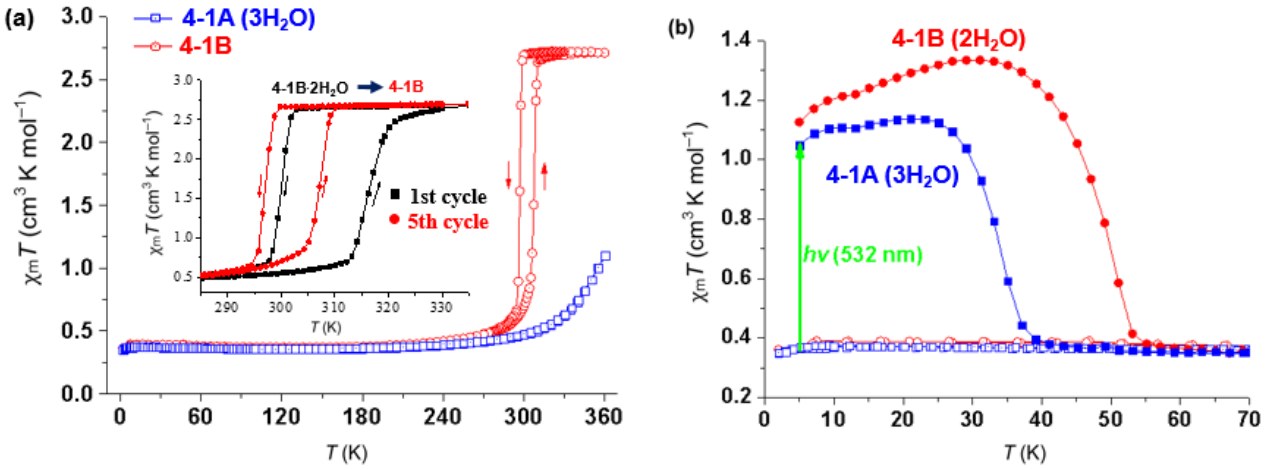

Figure 4.9. (a) Temperature dependence of $\chi_m T$ for **4-1A·3H₂O** (blue) and **4-1B·2H₂O** (red), samples were measured in the range of 2–360 K at a rate of 2 K/min, insert shows the thermal hysteresis loops in different scan cycles for **4-1B·2H₂O**. (b) Thermal relaxation of $\chi_m T$ for **4-1A·3H₂O** (blue) and **4-1B·2H₂O** (red) after irradiation with green light for 30 min, temperature increasing at 1 K/min.

For polymorph **4-1B·2H₂O**, the $\chi_m T$ vs. T exhibits an abrupt and complete transition with a thermal hysteresis loop at around room temperature, and the hysteretic transition is affected by the lattice water molecules (Figure 4.9a). When magnetic data were collected using the fresh crystal sample,

$\chi_m T$ increased abruptly with $T_{1/2}\uparrow$ = 316 K in the first heating mode and decreased sharply from the saturated value with $T_{1/2}\downarrow$ = 300 K in the first cooling mode (Figure 4.10 a). Upon repeated scans, dehydration was observed and magnetic transition occurred at lower temperatures, after several scan cycles, the temperature of this transition became almost invariant with $T_{1/2}\uparrow$ = 307 K and $T_{1/2}\downarrow$ = 297 K (Figure 4.10 a). Therefore, the final width of the thermal hysteresis loop is 10 K. In the low-temperature range, the $\chi_m T$ (0.36 cm^3 K mol^{-1}) value of **4-1B** is the same as that of **4-1A**, reflecting the oxidation and spin state of [*ls*-Co^{3+}–$dhbq^{3-}$–ls-Co^{3+}]$^{3+}$. The saturated $\chi_m T$ value at high temperature is 2.71 cm^3 K mol^{-1}, which reveals that the oxidation and spin state of this high-temperature phase is [*ls*-Co^{3+}–$dhbq^{2-}$–*hs*-Co^{2+}]$^{3+}$ (S = 3/2). This saturated $\chi_m T$ value is reasonable for high-spin Co(II) with large orbital contribution. Note that the dehydrated sample (**4-1B**) could be rehydrated upon exposure to air at RT, and the rehydrated sample shows the same magnetic behavior as that of the fresh sample. These results indicate that the thermal hysteresis can be adjusted by the guest water molecules.

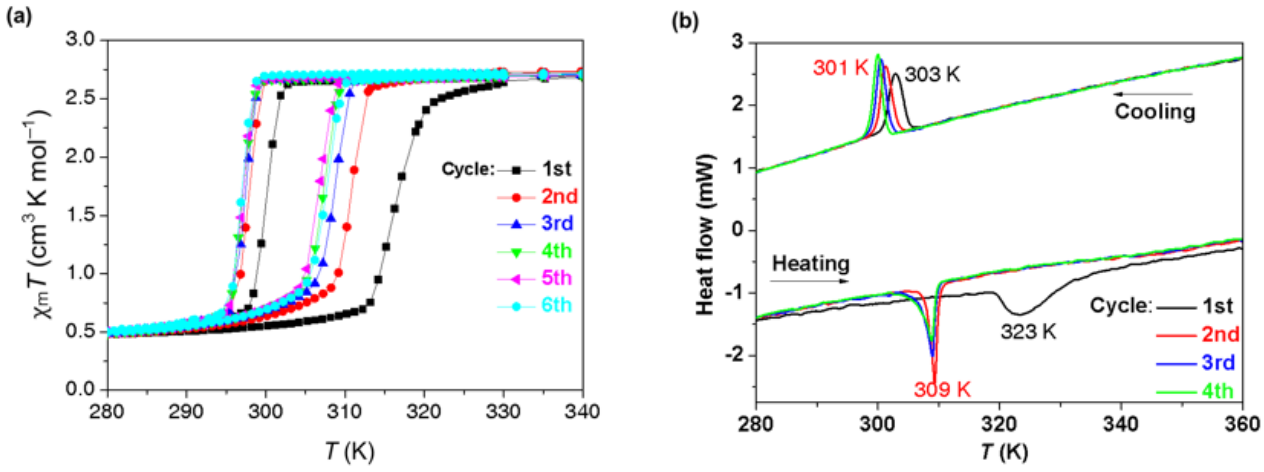

Figure 4.10. (a) Temperature dependence of $\chi_m T$ for **4-1B·2H₂O** showing hysteretic transition variation with repeated scan, (b) DSC for **4-1B·2H₂O** with repeated scan in the temperature range of 200−360 K.

The dependence of the hysteretic transition of **4-1B** on the lattice water was supported by

differential scanning calorimetry (DSC) (Figure 4.10b). The DSC curve features a broad endo peak at approximately 323 K in the first heating scan, which indicates that the endothermic contribution is from both VT phase transition and dehydration in the first heating scan. The sharp exo peak at 303 K in the first cooling scan is in reasonable agreement with the magnetic data. In the second scan cycle, the DSC data are almost in good agreement with the corresponding magnetic data, showing sharp endo and exo peaks at 309 K and 301 K, respectively. The DSC curve changes very slightly upon repeated scanning.

The two polymorphic complexes also display distinct LIESST (Light-Induced Excited Spin-State Trapping) behaviors (The fresh samples were used to measure photo-magnetic properties since the dehydrated samples can easy absorb water in the air). As shown in Figure 4.9b, after irradiation with 532 nm light at 5 K for 30 min, $\chi_m T$ increases from 0.36 cm^3 K mol^{-1} to its saturated values of 1.05 cm^3 K mol^{-1} for **4-1A·3H₂O** and 1.12 cm^3 K mol^{-1} for **4-1B·2H₂O**. After quenching the light, the thermal relaxation of $\chi_m T$ with increasing temperature differs between the two polymorphs. For **4-1A·3H₂O**, as the temperature increases to 9 K, $\chi_m T$ increases slowly to a maximum value of 1.10 cm^3 K mol^{-1}. The value then decreases abruptly above 33 K. Finally, at approximately 40 K, $\chi_m T$ returns to its original value. Meanwhile, the LIESST state of **4-1B·2H₂O** has a higher relaxation temperature than that of **4-1A·3H₂O**. In the case of **4-1B·2H₂O**, $\chi_m T$ continues to increase slightly up to 33 K, and then decreases sharply above 49 K before returning to its initial value at 55 K. These results also demonstrate that the $[ls\text{-}Co^{3+}\text{–dhbq}^{3-}\text{–}ls\text{-}Co^{3+}]^{3+} \leftrightarrows [ls\text{-}Co^{3+}\text{–dhbq}^{2-}\text{–}hs\text{-}Co^{2+}]^{3+}$ photo process is reversible for both polymorphs.

3.3.3 Optical Spectrum Analysis

The thermally induced valence tautomeric behavior for **4-1** in solution was checked by UV-vis absorption spectra. At 277 K, the solution sample displays obvious UV-vis absorption peaks at around 485 nm and 526 nm. These peaks are characteristic of ligand-to-metal charge transfer (LTCT) from the $dhbq^{3-}$ radical to one of cobalt ion.[8, 9] The intensity of these absorption peaks for this compound

in solution gradually decreases upon heating and virtually disappear by 330 K (Figure 3.11), revealing gradual valence tautomeric transition and a significant quantity of $\mathbf{1}^{3+}$ cations changed from the [*ls*-Co^{3+}–$dhbq^{3-}$–*ls*-Co^{3+}]$^{3+}$ sate to the [*ls*-Co^{3+}–$dhbq^{2-}$–*hs*-Co^{2+}]$^{3+}$ state, up to a temperature of 330 K. Note that the distinct forms of $\mathbf{1}^{3+}$ cations in solution at about 270 K and 330 K may be the main factor determined the polymorphic structures in crystal states.

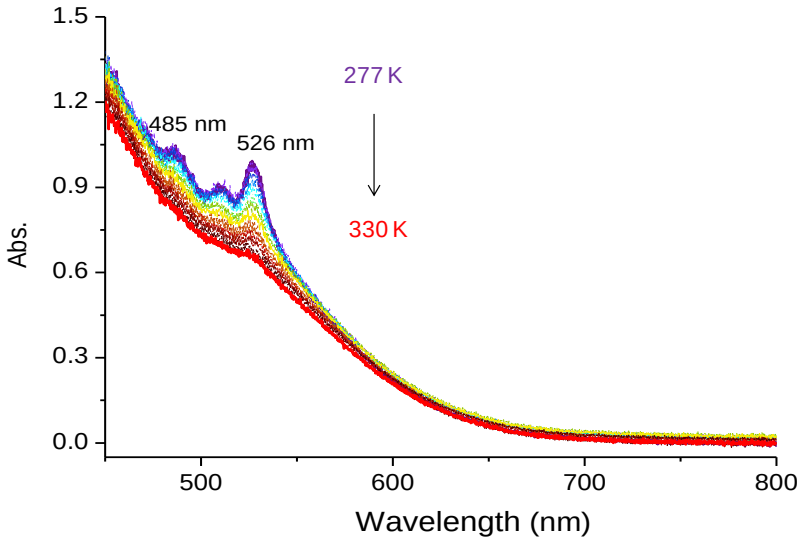

Figure 4.11. Temperature-dependent UV-vis absorption spectra of complex **4-1** in the butyronitrile solution (0.5 mmol/L).

The distinct thermally controlled valence tautomeric transitions of these two polymorphs were also supported by UV-vis absorption spectrum analysis (Figure 4.12). The UV-vis absorption spectra of **4-1A·3H₂O** and **4-1B·2H₂O** at 270 K are very similar and feature clear peaks of LTCT ($dhbq^{3-}$ radical to cobalt ion) at approximately 490 nm and 535 nm. The intensity of these peaks decreases slightly up to 333 K for **4-1A·3H₂O**, indicating an incomplete valence tautomeric transition. Meanwhile, for **4-1B·2H₂O**, these absorption bands decrease dramatically in intensity and almost disappear by 333 K, indicating an abrupt valence tautomeric transition from [*ls*-Co^{3+}–$dhbq^{3-}$–*ls*-Co^{3+}]$^{3+}$ to [*ls*-Co^{3+}–$dhbq^{2-}$–hs-Co^{2+}]$^{3+}$.

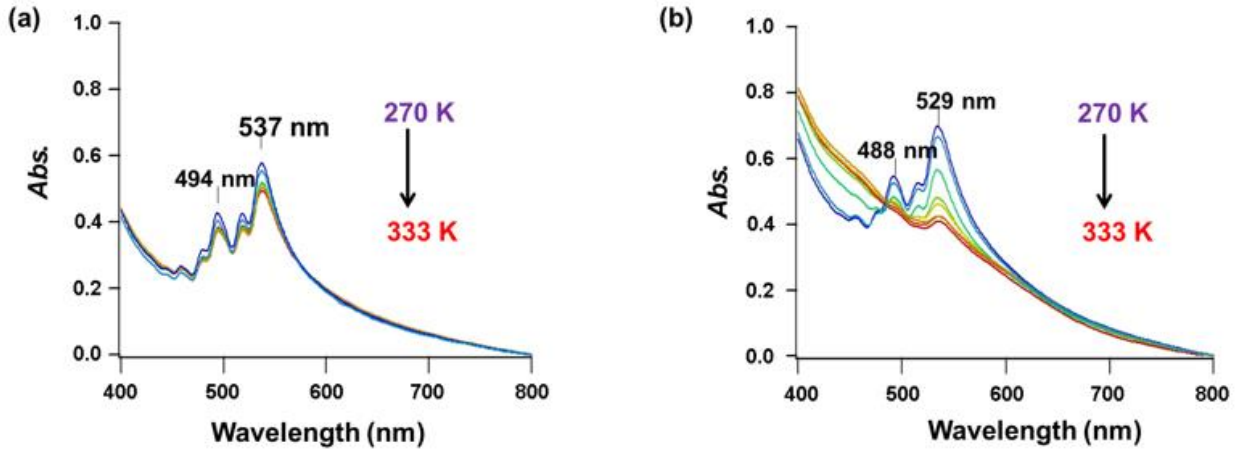

Figure 4.12. Temperature-dependent UV-vis spectra for **4-1A·3H₂O** (a) and **4-1B·2H₂O** (b).

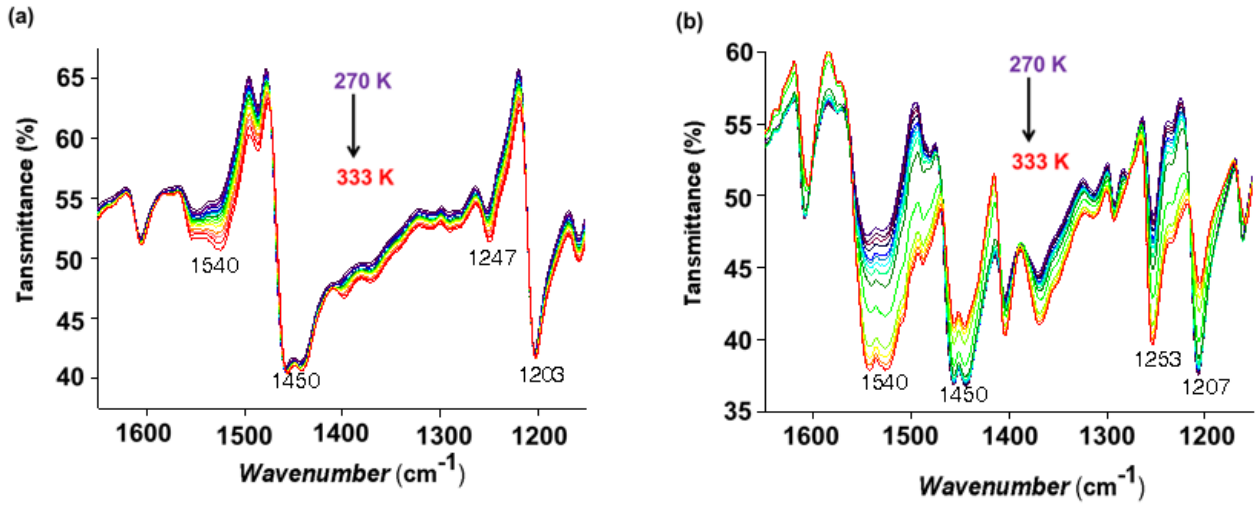

Figure 4.13. Temperature-dependence of IR spectra for **4-1A·3H₂O** (a) and **4-1B·2H₂O** (b).

The IR spectra of these polymorphs underwent the same changes upon the valence tautomeric transition from [*ls*-Co^{3+}–$dhbq^{3-}$–*ls*-Co^{3+}]$^{3+}$ to [*ls*-Co^{3+}–$dhbq^{2-}$–*hs*-Co^{2+}]$^{3+}$. The absorption peaks for $dhbq^{3-}$ (ca. 1550 cm^{-1}) and the associated C–O bond-stretching vibration (ca. 1250 cm^{-1}) increased, while the absorption peaks for $dhbq^{2-}$ (ca. 1205 cm^{-1}) and the corresponding C–O bond-stretching mode (ca. 1450 cm^{-1}) decreased. These variations are subtle for **4-1A·3H₂O** but obvious for **4-1B·2H₂O** (Figure 3.13). Additionally, IR spectra of light-excited state for this valence tautomeric compound were also representatively measured on **4-1B·2H₂O**. After photo irradiation at 17 K, the

absorption peaks for $dhbq^{3-}$ (ca. 1550 cm^{-1}) and the associated C–O bond-stretching vibration (ca. 1267 cm^{-1}) obviously increased, while the absorption peaks for $dhbq^{2-}$ (ca. 1210 cm^{-1}) with corresponding C–O bond-stretching mode (ca. 1462 cm^{-1}) clearly decreased. Upon heating, the IR spectra slowly relaxed back to the initial one (Figure 4.14).

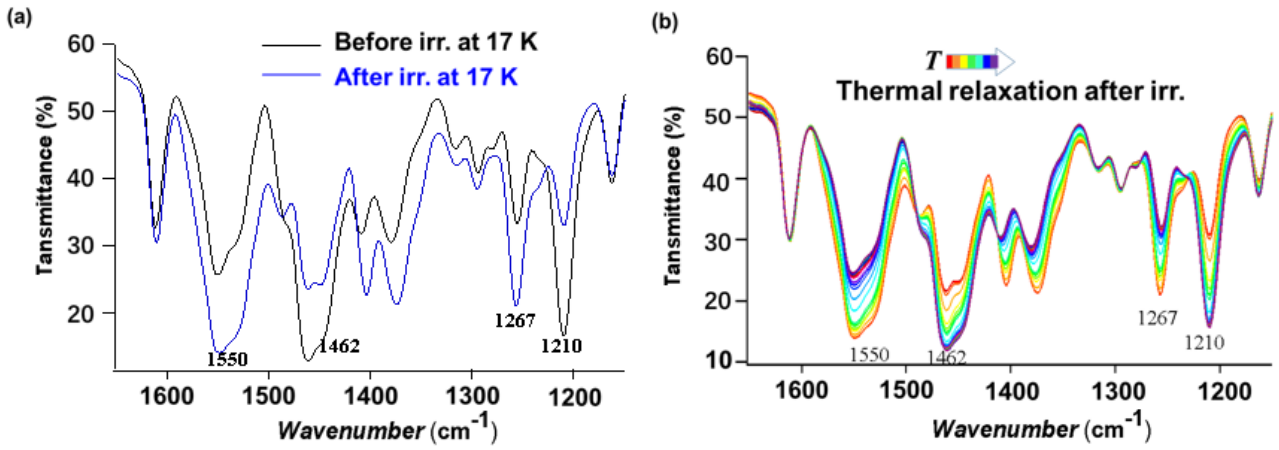

Figure 4.14. (a) IR spectra measured before and after photo irradiation for **4-1B·2H₂O**, and (b) IR spectra measured during thermal relaxation of light-excited state for **4-1B·2H₂O**.

4.3.3 Influence of Intermolecular Interactions on Valence Tautomeric Transition

Note that a valence tautomeric transition is mainly affected by the redox potential difference between metal centers and redox-active ligands.[2] Thus, studies on ligand dependence of valence tautomeric transition have been investigated to tune redox potential of metal centers, which are mainly considered as studies about molecular factors.[3e, 4c] In these studies, intermolecular factors have also been discussed since the modification of coordination ligands would certainly cause distinct intermolecular structures. Herein, the distinct thermal valence tautomeric behaviors for **4-1A·3H₂O** and **4-1B·2H₂O** are only ascribed to the differences in their intermolecular factors. In polymorph **4-1A·3H₂O**, the $\mathbf{1}^{3+}$ cations form very weak π···π interactions among themselves, and thus, there is essentially no efficient intermolecular cooperation in this polymorphic form (Figure 4.15 a). Thus, there is a relatively slight valence tautomeric transition with increasing temperature. In contrast, the

1^{3+} cations in **4-1B·2H₂O** exhibit relatively strong π···π intermolecular interactions (Figure 4.15b), favoring the cooperative effect and leading to an abrupt valence tautomeric transition with a thermal hysteresis loop. It worthy to note that UV-vis absorption spectrum analysis revealed the solution sample of **4-1** exhibiting more complete valence tautomeric transition than that for solid state of **4-1A·3H₂O**. This may be ascribed to that the **1^{3+}** cations distributed in a relatively relaxing surrounding, which favors the low spin Co(III) ions with smaller volumes changing to high spin Co(II) ions with larger volumes. The distinctive thermal relaxation temperature for the LIESST state of **4-1A·3H₂O** and **4-1B·2H₂O** may also relate to the different intermolecular interactions in the solid state.[34]

The lattice-water-controlled hysteretic transition of **4-1B·2H₂O** is also attributed to intermolecular factors. The hydrogen bonds formed between the water molecules and **1^{3+}** cations play a significant role in the shift of the valence tautomeric transition temperature, even though these hydrogen bonds are very weak. The hydrogen bond O–H(water)···O(dhbq) is expected to have an electron-withdrawing effect on both the Co center and $dhbq^{3-}$ radical. However, this electron-withdrawing effect may have greater influence on the $dhbq^{3-}$ radical than on Co ion, which stabilizes the radical form [*ls*-Co^{3+}–$dhbq^{3-}$–*ls*-Co^{3+}]$^{3+}$ and thereby increasing the valence tautomeric transition temperature. Similar hydrogen bond effects have been observed in metal-to-metal electron-transfer-coupled spin-transition systems.[50, 51] In addition, these hydrogen bonds may also affect the intermolecular cooperativity. It is possible that the formation of stronger hydrogen bonds between the guest molecules and **1^{3+}** cations would increase the transition temperature shift observed in this system.

4. 4 Conclusion

Two polymorphic structures have been well determined in a valence tautomeric dinuclear cobalt complex. These polymorphs show distinct thermal and photo magnetic behaviors, and are thus, ideal for studying the "pure" intermolecular factors to valence tautomeric transitions. In polymorph **4-1A·3H₂O**, the valence tautomeric cations are arranged *head-to-waist* with their neighbors and exhibit

weak π···π interactions, resulting in a gradual and incomplete thermal valence tautomeric transition. In contrast, the cations in polymorph **4-1B** are arranged *head-to-tail* and exhibit relatively strong π···π interactions, leading to an abrupt and complete thermal valence tautomeric transition with adjustable hysteresis loop at around room temperature. The valence tautomeric transition process for both polymorphs can be induced by light, but the light-excited state of **4-1B·2H$_2$O** has a higher thermal relaxation temperature than that of **4-1A·3H$_2$O**. Another important finding is that the cations in **4-1B** display no-polar-to-polar structural transition accompanied with valence tautomeric behavior, an significant feature to produce interesting electronic properties. Unfortunately, the polar effect is cancelled by three-dimensional packing structure.

In conclusion, this study provide a new insight into the "pure" contribution of intermolecular factors to the valence tautomeric transition. Similar to spin crossover complexes, strong π···π intermolecular interactions among valence tautomeric molecules generate desirable magnetic properties, including a thermal hysteretic transition and higher relaxation temperature for the LIESST state. Additionally, controlling the intermolecular interaction between valence tautomeric molecules and guest molecules is an efficient means of adjusting the hysteretic transition in valence tautomeric compounds. These results indicate that intermolecular interactions play an important role in the magnetic behaviors of valence tautomeric complexes, which suggests that both molecular and intermolecular factors should be carefully considered in the further development of practical valence tautomeric materials. One significant but challenging task in valence tautomeric system is preparation of switchable polar materials through adjusting molecular packing structures together with artful chemical design.

References

(1) O. Kahn, C. J. Martinez, *Science* **1998**, *279*, 44–48.

(2) A. Bousseksou, G. Molnár, P. Demont, J. Menegotto, *J. Mater. Chem.* **2003**, *13*, 2069–2071.

(3) A. Calzolari, Y. Chen, G. F. Lewis, D.B. Dougherty, D. Shultz, M. B. Nardelli, *J. Phys. Chem. B* **2012**, *116*, 13141–13148.

(4) O. Sato, J. Tao, Y.-Z. Zhang, *Angew. Chem. Int. Ed.* **2007**, *46*, 2152–2187.

(5) E. Evangelio, D. Ruiz-Molina, *Eur. J. Inorg. Chem.* **2005**, *118*, 2957–2971.

(6) T. Tezgerevska, K. G. Alley, C. Boskvic, *Coord. Chem. Rev.* **2014**, *268*, 23–40.

(7) C. Carbonera, A. Dei, J.-F. Létard, C. Sangregoria, L. Sorace, *Angew. Chem. Int. Ed.* **2004**, *43*, 3136–3138.

(8) J. Tao, H. Maruyama, O. Sato, *J. Am. Chem. Soc.* **2006**, *128*, 1790–1791.

(9) B. Li, J. Tao, H.-L. Sun, O. Sato, R.-B. Huang, L.-S. Zheng, *Chem. Commun.* **2008**, 2269–2271.

(10) B. Li, L.-Q. Chen, J. Tao, R.-B. Huang, L.-S. Zheng, *Inorg. Chem.* **2013**, *52*, 4136−4138.

(11) K. G. Allery, G. Poneti, J. B. Aitken, R. K. Hocking, B. Moubaraki, K. S. Murray, B. F. Abrahams, H. H. Harris, L. Scorace, C. Boskovic, *Inorg. Chem.* **2012**, *51*, 3942−3946.

(12) V. I. Minkin, A. A. Starikova, A. G. Starikov, *Dalton Trans.* **2015**, *44*, 1982–1991.

(13) K. G. Alley, G. Poneti, P. S. D. Robinson, A. Nafady, B. Moubaraki, J. B. Aitken, S. C. Drew, C. Ritchie, B. F. Abrahams, R. K. Hocking, K. S. Murray, A. M. Bond, H. H. Harris, L. Scorace, C. Boskovic, *J. Am. Chem. Soc.* **2013**, *135*, 8304–8323.

(14) D. Schweinfurth, Y. Rechkemmer, S. Hohloch, N. Deibel, I. Peremykin, J. Fiedler, R. Marx, P. Neugebauer, J. van Slageren, B. Sarkar, *Chem. Eur. J.* **2014**, *20*, 3475–3486.

(15) M. van der Meer, Y. Rechkemmer, U. Frank, F.D. Breitgoff, S. Hohloch, C.-Y. Su, P. Neugebauer, R. Marx, R. Marx, M. Dörfel, J. van Slageren, B. Sarkar, *Chem. Eur. J.* **2016**, *22*, 13884–13893.

(16) A. Witt, F. W. Heinemann, S. Sproules, M. M. Khusniyarov, *Chem. Eur. J.* **2014**, *20*, 11149–11162.

(17) P. Gütlich, A. Dei, *Angew. Chem. Int. Ed.* **1997**, *36*, 2734–2736.

(18) R. D. Schmidt, D. A. Shultz, J. D. Martin, P. D. Boyle, *J. Am. Chem. Soc.* **2010**, *132*, 6261–6273.

(19) A. Witt, F. W. Heinemann, M. M. Khusniyarov, *Chem. Sci.* **2015**, *6*, 4599–4609.

(20) D. Kiriya, H.-C. Chang, S. Kitagawa, *J. Am. Chem. Soc.* **2008**, *130*, 5515–5522.

(21) D. Kiriya, H.-C. Chang, K. Nakamura, D. Tanaka, K. Yoneda, S. Kitagawa, *Chem. Mater.* **2009**, *21*, 1980–1988.

(22) P. Dapporto, A. Dei, G. poneti, L. Sorace, *Chem. Eur. J.* **2008**, *14*, 10915–10918.

(23) A. Droghetti, S. Sanvito, *Phys. Rev. Lett.* **2011**, *107*, 047201.

(24) Y. Mulyana, G. Poneti, B. Moubaraki, K. S. Murray, B. F. Abrahams, L. Sorace, C. Boskovic, *Dalton Trans.* **2010**, *39*, 4757–4767.

(25) O.-S. Jung, C. G. Pierpont, *J. Am. Chem. Soc.* **1994**, *116*, 2229–2230.

(26) F. Novio, J. Campo, D. Ruiz-Molina, *Inorg. Chem.* **2014**, *53*, 8742–8748.

(27) X.-Y. Chen, R.-J. Wei, L.-S. Zheng, J. Tao, *Inorg. Chem.* **2014**, *53*, 13212–13219.

(28) C. W. Lange, M. Foldeaki, V. I. Nevodchilov, V. K. Cherkasov, G. A. Abakumov, C. G. Pierpont, *J. Am. Chem. Soc.* **1992**, *114*, 4220–4222.

(29) W.-Q. Cheng, G.-L. Li, R. Zhang, Z.-H. Ni, W.-F. Wang, O. Sato, *J. Mol. Struct.* **2015**, *1087*, 68–72.

(30) I. Imaz, D. Maspoch, C. Rodríguez-Blanco, J. M. Préz-Falcón, J. Campo, D. Ruiz-Molina, *Angew. Chem. Int. Ed.* **2008**, *47*, 1857–1860.

(31) B. Li, L.-Q. Chen, R.-J. Wei, J. Tao, R.-B. Huang, L.-S. Zheng, Z. Zheng, *Inorg. Chem.* **2011**, *50*, 424–426.

(32) B. Weber, W. Bauer, J. Obel, *Angew. Chem. Int. Ed.* **2008**, *47*, 10098–10101.

(33) S. Hayami, Z.-Z. Gu, H. Yoshiki, A. Fujishima, O. Sato, *J. Am. Chem. Soc.* **2001**, *123*, 11644–11650.

(34) M. B.-L. Cointe, J. Hébert, C. Baldé, N. Moisan, L. Toupet, P. Guionneau, J. F. Létard, E. Freysz, H. Cailleau, E. Collet, *Phys. Rev. B* **2012**, *85*, 064114.

(35) O. Iasco, E. Rivière, R. Guillot, M. B.-L. Cointe, J.-F. Meunier, A. Bousseksou, M.-L. Boillot, *Inorg. Chem.* **2015**, *54*, 1791−1799.

(36) J. Tao, R.-J. Wei, R.-B. Huang, L.-S. Zheng, *Chem. Soc. Rev.* **2012**, *41*, 703–737.

(37) W. Phonsri, C. G. Davice, G. N. L. Jameson, B. Moubaraki, K. S. Murray, *Chem. Eur. J.* **2016**, *22*, 1322–1333.

(38) J. Luan, J. Zhou, Z. Liu, B. Zhu, H. Wang, X. Bao, W. Liu, M.-L. Tong, G. Peng, H. Peng, L. Salmon, A. Bousseksou, *Inorg. Chem.* **2015**, *54*, 5145−5147.

(39) M. B. Bushuev, V. A. Daletsky, D. P. Pishchur, Y. V. Gatilov, I. V. Korolkov, E. B. Nikolaenkova, V. P. Krivopalov, *Dalton Trans.* **2014**, *43*, 3906–3910.

(40) C. Bartual-Murgui, C. Codina, O. Roubeau, G.Aromí, *Chem. Eur. J.* **2016**, *22*, 12767-12776.

(41) T. Romero-Morcillo, M. Seredyuk, M. C. Munoz, J. A. Real, *Angew. Chem. Int. Ed.* **2015**, *54*, 14777–14781.

(42) H. Peng, S. Tricard, G. Félix, G. Molnár, W. Nicolazzi, L. Salmon, A. Boussekson, *Angew. Chem. Int. Ed.* **2014**, *53*, 10894–10898.

(43) R. Ohtani, K. Yoneda, S. Furukawa, N. Horike, S. Kitagawa, *J. Am. Chem. Soc.* **2011**, *133*, 8600–8605.

(44) Kulmaczewski, R.; Olguín, J.; Kitchen, J. A.; Feltham, H. L. C.; Jameson, G. N. L.; Tallon, J. L.; Brook, S. *J. Am. Chem. Soc.* **2014**, *136*, 878–881.

(45) H. Hagiwara, S. Okada, *Chem. Commun.* **2016**, *52*, 815–818.

(46) I. Boldog, A. B. Gaspar, V. Martínez, P. Pardo-Ibáñez, V. Ksenofontov, A. Bhattacharjee, P. Gütlich, J. A. Real, *Angew. Chem. Int. Ed.* **2008**, *47*, 6443–6447.

(47) G. M. Sheldrick, *Acta Cryst. C.* **2015**, 71, 3–8.

(48) M. J. Frisch, G. W. Trucks, H. B. Schlegel el al. *Gaussian, Inc., Wallingford CT*, **2009**.

(49) R. Krishnan, J. S. Binkley, R. Seeger, Pople, J. A. J. Chem. Phys. **1980**, *72*, 650–654.

(50) N. Hoshino, F. Iijima, G. N. Newton, N. Yoshida, T. Shiga, H. Nojiri, A. Nakao, R. Kumai, Y. Murakami, H. Oshio, *Nat. Chem.* **2012**, *4*, 921–926.

(51) K. Mitsumoto, E. Oshiro, H. Nishikawa, K. Shiga, Y. Yamamura, K. Saito, H. Oshio, *Chem. Eur. J.* **2011**, *17*, 9612–9618.

Chapter 5. Conclusions

Coordination compounds exhibiting spin state transition behaviors serve as important candidates for the exploitation of practicable electronic devices, such as high-density information storage devices, quantum computation, or molecular spintronics. The spin state transition in coordination complexes can be accessed through flipping the spin orientation and spin number change. Importantly, these spin sate transition behaviors are deeply affected by coordination ligands because of that the auxiliary ligands can adjust the magnetic anisotropy (for slow magnetization relaxation), ligand field strength (for spin transition), redox potential (for charge transfer) for the metal centers. Additionally, these spin state transition behaviors also rely on the molecular geometries and intermolecular interactions. For example, high-symmetric geometry of metal center can limit the transverse zero-splitting in a small level, which favor the complex to show slow magnetization relaxation behavior. Additionally, strong intermolecular interactions can generate cooperative effect thus generally lead to abrupt magnetic transition with hysteresis, but go against to slow magnetization dynamics since strong intermolecular interactions usually result in dipolar-dipolar interaction.

In **chapter 2**, an octa-coordinated Fe(II) complex, $[Fe^{II}(dpphen)_2](BF_4)_2 \cdot 1.3H_2O$ (dpphen = 2,9-di(pyrazo-1-yl)-1,10-phenanthroline) with a pseudo-D_{2d} symmetric metal center showing slow magnetic relaxation is reported. This Fe(II) complex slow magnetic relaxation (single-ion magnet, SIM) behavior since this it possesses strong uniaxial magnetic anisotropy. The uniaxial magnetic anisotropy for this high-coordinated Fe(II) is confirmed by magnetic measurement, high-frequency/field electron paramagnetic resonance (HF-EPR) studies, and *ab initio* calculations, which reveal that it has a negative axial zero-field splitting ($D \approx -6.0$ cm^{-1}) and a small rhombic zero-field splitting ($E \approx 0.04$ cm^{-1}). More interestingly, the magnetic units $[Fe^{II}(dpphen)_2]^{2+}$ arranged parallel to each other with their magnetic easy axis near to the crystalline *c*-axis, and thus serves as a perfect object for examining the fitness of experiment results and theoretical results. Under applied dc

magnetic fields, the octa-coordinated Fe(II) complex exhibits slow spin direction transition behavior at low temperature. Fitting the relaxation time with the Arrhenius mode combining Orbach and tunneling terms affords a good fit to all the data and yields an effective energy barrier (17.0 cm^{-1}) close to the energy gap between the ground state and the first-excited state. The origin of the strong uniaxial magnetic anisotropy for this complex has been clearly understood from theoretical calculations. Generally, slow magnetization dynamics in transition-metal compounds are prevalently via reducing coordination numbers to reduce the orbital quenching effect, especially for the non-Kramers ions. Thus, our results provide a new strategy for realizing slow magnetization dynamics in high-coordinated transition complexes.

In **chapter 3**, in order to observe charge transfer coupled spin transition (CTCST) behavior in cyanide-bridged Fe^{II}/Fe^{III}, ligand (1,4-(1H-1,2,4-triazole)butane, btb) with stronger π-acceptor ability has been used. Two new cyanide-bridged Fe^{II}/Fe^{III} mixed-valence compounds are presented, which were obtained via cyanoferrate ($[Fe^{III}(Tp)(CN)_3]^-$, Tp = hydrotris(pyrazolyl)borate) and flexible ligand btb under different synthesis conditions. One of these two new compound $\{[Fe(Tp)(CN)_3]_2Fe(btb)\cdot H_2O\}_n$ is a cyanide-bridged one-dimensional $\{Fe^{III}_2Fe^{II}\}_n$ double-zigzag chain, and exhibits thermal and photo-induced spin transition behavior in the Fe(II) sites. Whereas the other compound $[Fe(Tp)(CN)_3]_2Fe(btb)_2\cdot 2H_2O$ features cyanide-bridged trinuclear linear $Fe^{III}_2Fe^{II}$ motifs further linked by btb forming an extended linear chain, and shows weak antiferromagnetic interactions between metal centers. These results suggest that flexible ligands are sensitive to synthesis conditions and can be used to produce variable structures and magnetic properties. Although CTCS behavior has not been observed, the proposal for doing further work was provided, namely the ligand field strength and redox potential for the metal center should be carefully balanced via using ligand with moderate π-acceptor ability.

In **chapter 4**, polymorphic structures and water-tunable thermal hysteresis in a valence tautomeric dinuclear cobalt complex $[\{Co(tpa)_2\}(dhbq)](PF_6)_3$ (tpa = tris(2-pyridylmethyl)amine, dhbq =

deprotonated 2,5-dihydroxy-1,4-benzoquinone) is introduced. Two polymorphs of complex $[\{Co(tpa)_2\}(dhbq)](PF_6)_3$ were obtained via controlling the recrystallization temperature. Importantly, the two polymorphs display very distinct magnetic behaviors, thus provide a good opportunity for the investigation on the "pure" contribution of intermolecular factors to the valence tautomeric behaviors. The polymorph with the $[\{Co(tpa)_2\}(dhbq)]$ cations arranged *head-to-tail* characterizes relatively strong π···π interactions, and thus shows an abrupt and complete thermal valence tautomeric transition with adjustable hysteresis loop at around room temperature. Whereas, the polymorph featuring valence tautomeric cations arranged *head-to-waist* with their neighbors exhibits weak π···π interactions, thus lead to a gradual and incomplete thermal valence tautomeric transition. The valence tautomeric transition process for both polymorphs can be induced by light, but the light-excited states for them show distinct thermal relaxation behaviors.

The research in this thesis presents serval novel results in spin state transition behaviors, which provides some available knowledge, from both molecular and intermolecular level, for further development of practicable magnetic materials. However, since the spin state transition in coordination compounds are determined by various factors, it still remains great challenge to clearly clarify the net relationship between magnetic properties and one of their determining factor, although numerous of complexes exhibiting spin variation behaviors have been well studied. It cannot be denied that the reported results continuously provide inspiration for the development of novel and intriguing properties in coordination compounds. Hence, research on spin state transition in coordination complexes remains significant, and new insight into the intrinsic nature of magnetic compounds as well as novel magnetic properties still can be expected.

Acknowledgement

I wish to extend my greatest gratitude for the person who provide me invaluable help for pursuing my doctor degree in Kyushu University.

Certainly, my deepest appreciation goes foremost to my supervisor, Prof. Osamu Sato, who offered the opportunity for me to study and do research in his group, and guided me to finish this thesis.

Secondly, I would like to express my sincere thanks to all our group members, especially Dr. Zi-Shuo Yao, Dr. Sheng-Qun Su, Mr. Shu-Qi Wu, Dr. You-Gui Huang, Dr. Shinji Kanegawa, Dr. Soonchul Kang, Mr. Jun-Qiu Li and Dr. Wei Huang, Ms. Tomoko Ueda and my friend Dr. Xu-Hui Li, all of them rendered me much help in my research and/or afforded me a happy life during the four years.

Thirdly, I would like to express my gratitude to Prof. Zhong-Hai Ni in China University of Mining and Technology, Prof. Zhenxing Wang in Huazhong University of Science and Technology, Prof. Takashi Yamamoto in Keio University, for their help in property measurements and analysis.

My deepest appreciation also goes to my parents and my all family members.

Finally, my great gratitude goes to my dear country. I cannot focus on my research without the scholarship provided by China Scholarship Council.

List of publication

1. **Li G. L.**, Kanegawa, S., Yao Z. S., Su S. Q, Wu S. Q., Huang Y. G., Kang S., Sato O.

   Influence of intermolecular interactions on valence tautomeric behaviors in two polymorphic dinuclear cobalt complexes.

   Chemistry - A European Journal, **2016**, *22*, 17130–17135.

2. **Li G. L.**, Wu S. Q., Zhang L. F., Wang Z., Ouyang Z. W., Ni Z. H., Su S. Q., Yao Z. S., Sato O.

   Field-induced slow magnetic relaxation in an octa-coordinated Fe(II) complex with pseudo-D_{2d} symmetry: magnetic, HF-EPR and theoretical investigations

   Inorganic Chemistry, **2017**, *56*, 8018−8025.

3. **Li G. L.**, Sato O.

   A compressed octahedral cobalt(II) complex in the crystal structure of diaqua[6,6'-sulfanediylbis(2,2'-bipyridine)]cobalt(II) dinitrate

   Acta Crystallogr E , **2017**, *E73*, 993–995.

4. **Li G. L.** Kang S., Kanegawa S. Sato O.

   Control of structures and magnetic properties in the cyanide-bridged Fe^{II}/Fe^{III} mixed-valence system using flexible ligand under different synthesis conditions.

   Physical Chemistry Chemical Physics (Under preparation)